

Active Vibration Control of a Flexible Robotic Manipulator

A Thesis Submitted to the
College of Graduate and Postdoctoral Studies
In Partial Fulfillment of the Requirements
For the Degree of Master of Science
In the Department of Mechanical Engineering
University of Saskatchewan
Saskatoon

By

Amir Mohamad Kamalirad

© Copyright Amir Mohamad Kamalirad, December 2022. All rights reserved.

Unless otherwise noted, copyright of the material in this thesis belongs to the author.

Permission to use

In presenting this thesis/dissertation in partial fulfillment of the requirements for a Postgraduate degree from the University of Saskatchewan, I agree that the Libraries of this University may make it freely available for inspection. I further agree that permission for copying of this thesis/dissertation in any manner, in whole or in part, for scholarly purposes may be granted by the professor or professors who supervised my thesis/dissertation work or, in their absence, by the Head of the Department or the Dean of the College in which my thesis work was done. It is understood that any copying or publication or use of this thesis/dissertation or parts thereof for financial gain shall not be allowed without my written permission. It is also understood that due recognition shall be given to me and to the University of Saskatchewan in any scholarly use which may be made of any material in my thesis/dissertation.

Requests for permission to copy or to make other uses of materials in this thesis/dissertation in whole or part should be addressed to:

Head of the Department of Mechanical Engineering
University of Saskatchewan, College of Engineering
3B48 Engineering Building, 57 Campus Drive
Saskatoon, Saskatchewan, S7N 5A9, Canada

OR

Dean
College of Graduate and Postdoctoral Studies
University of Saskatchewan
116 Thorvaldson Building, 110 Science Place
Saskatoon, Saskatchewan S7N 5C9 Canada

Abstract

A five-degree-of-freedom (5-DOF) robot manipulator for agricultural applications was developed by previous members of the robotic lab at University of Saskatchewan. The manipulator was designed to be installed on a mobile base vehicle for monitoring targeted crops in a farm field using sensors installed on its tip. The crop monitoring is called phenotyping. When the manipulator mobile base moves along the field, vibration is induced from the farm terrain to the base of manipulator. Thus, the sensors mounted at the end-effector (EE) of the manipulator may not record data accurately. To address this issue, vibration suppression of the manipulator is necessary.

The objectives of this research were: 1. Evaluation of vibration experienced by the 5-DOF manipulator's tip; and 2. Study active vibration control to remedy vibration experienced by the manipulator; also, some efforts were done for possible implementation of active vibration control on the manipulator in a laboratory setting.

Free and forced vibration simulation studies were conducted to evaluate the amplitude of vibration transmitted to the EE from the base of the manipulator. To eliminate excitation coming from the manipulator's base, an active vibration suppression method using a model-based controller was used. To obtain a mathematical model for the manipulator, finite element analysis was utilized using commercial software and was verified manually. This method was applied to three different cases: 1- a cantilever beam, 2- a two-link, two-joint manipulator (2L2JM), and 3- the 5-DOF manipulator. For active vibration control, model reduction was applied to a state-space model of systems via a matched-DC algorithm. The LQR (linear-quadratic regulator) was used for the cantilever beam vibration control. For the 2L2JM and the 5-DOF manipulator, a H^∞ controller was used. This was an optimal and robust controller based on the H^∞ norm.

Based on vibration evaluation, it was found that an active vibration suppression was necessary for the 5-DOF manipulator. Mathematical models of several systems were developed and verified using finite element analysis. The controllers suppressed random vibration that were applied to the base of the 5-DOF manipulator. For the closed-loop control system of the manipulator, a look-up table was created for the actuators.

Through this study, the vibration of the 5-DOF manipulator was analyzed. Then, mathematical models of different geometries as well as the 5-DOF manipulator were obtained. Then these

models were compared with the software models. The model reduction approach made the large finite element models reduce to systems with a small order. Using models and control strategies, simulation studies were conducted for the vibration suppression of the manipulator.

Acknowledgements

I would like to express my sincere gratitude to my supervisor Prof. Reza Fotouhi and my advisory committee members, Prof. Bruce Sparling, and Prof. Ikechukwuka Oguocha, for the support and guidance throughout my graduate study.

I would also like to thank my supervisor for his financial support from his grant from Natural Sciences and Engineering Research Council of Canada (Prof. Fotouhi NSERC grant). Moreover, I appreciate the Mechanical engineering department of university of Saskatchewan for Devolved M.Sc. Scholarship for graduate studies.

I also appreciate the help from Mr. Douglas Bitner, Mechanical Engineering department of University of Saskatchewan for his valuable supports. The help from Robotics Lab members, including Mitra Taghizadeh, Majid Khakpour, Hedieh Badkoobehhezaveh, Qianwei Zhang, Amir Khozimeh, Joshua Cote, and Zachary Ochitawa are also appreciated.

Finally, I want to thank my parents for their support.

Contents

Permission to use	i
Abstract	ii
Acknowledgements	iv
Contents	v
List of Figures	viii
List of Tables	vii
List of abbreviations	viii
List of symbols.....	xiii
Chapter 1. Introduction.....	1
1.1 Motivation.....	1
1.2 Background	1
1.3 Problem statement.....	2
1.4 Literature review	3
1.5 Objectives	5
1.6 Methodology	6
1.7 Key contribution of thesis.....	7
1.8 Outline of the thesis	7
Chapter 2. Vibration Evaluation.....	9
2.1 Free vibration evaluation	9
2.2 Forced vibration evaluation	13
2.3 Summary	20
Chapter 3. Finite Element Model of Manipulators	21
3.1 Finite element model of a cantilever beam	21
3.2 Finite element model of two-link two-joint manipulator.....	25
3.3 State-space modeling using principal coordinates	28
3.4 Balanced realization and model reduction	31
3.5 Modal FEA-A for the manipulators studied.....	34
3.6 Verification of finite element models	37
3.7 State-space modeling for the manipulators	40
3.8 Transient analysis methodology.....	43
3.9 Results, cantilever beam model	45
3.10 Results, two-link two-joint manipulator (2L2JM)	50
3.11 Results, 5-DOF manipulator	55

3.12	Summary	60
Chapter 4.	Vibration Controller Design.....	62
4.1	Vibration controller using LQR for cantilever beam	63
4.2	Vibration controller- cantilever beam results.....	64
4.3	Vibration control using H_{∞} for 2L2JM and 5-DoF manipulator	72
4.4	Vibration controller- two-link two-joint manipulator (2L2JM) results	73
4.5	Vibration controller- 5-DOF manipulator results	80
4.6	Summary	88
Chapter 5.	Implementation of Active Vibration Controller.....	89
5.1	Tip displacement measurement and verification.....	89
5.2	Stepper motor field of operation experiment	93
5.3	Summary	99
Chapter 6.	Conclusion and Future Work	100
6.1	Conclusions.....	100
6.2	Future work.....	101
	References.....	103
	Appendixes	107

List of Tables

Table 2.1. Natural frequencies and mode characteristics of the 5-DOF manipulator (fixed base and joints).....	11
Table 2.2. Displacement transmissibility of harmonic excitation and random vibration on the base of the 5-DOF manipulator. Indicated points correspond to Figure 2.6.....	19
Table 3.1. Specifications of the cantilever beam.	21
Table 3.2. Cantilever beam, natural frequencies for manual FEM and FEA-A for different number of elements.....	39
Table 3.3. The 2L2JM, natural frequencies for manual FEM and FEA-A for different number of elements.	40
Table 3.4. Normalized RMS values of different models and their comparison with FEA-A transient for the cantilever beam.....	48
Table 3.5. Normalized RMS values of different models and their comparison with FEA-A transient for the 2L2JM.....	53
Table 3.6. RMS values of different models and their comparison with FEA-A transient for the 5-DOF manipulator.	58
Table 5.1. Torque (Nm) measured based on specific acceleration and speed of the motor (test1).	97
Table 5.2. Max torque of the motor and the current at a certain speed (test 2).	98

List of Figures

Figure 1.1. 5-DOF manipulator of U of S.....	2
Figure 2.1. The 5-DOF manipulator mesh results in FEA-A workbench.....	10
Figure 2.2. First mode of the 5-DOF manipulator with fixed base and joints (1st lateral).....	12
Figure 2.3. Second mode of the 5-DOF manipulator with fixed base and joints (1st vertical).	12
Figure 2.4. Mass-damper-spring model of the manipulator with moving base.	13
Figure 2.5. 5-DOF displacement transmissibility in frequency domain (EE displacement / base displacement). The base is under harmonic excitation (equation 2-4) over the range of [0.1,100] Hz. The 4 indicated points are the first 4 vertical modes.....	15
Figure 2.6. PSD of the random vibration for the base excitation.	16
Figure 2.7. The displacement of the base and EE of the 5-DOF manipulator in time domain. the base of the 5-DOF manipulator (see appendix A) is under random vibration (red solid line). This vibration is transmitted to the EE (blue dashed line).....	18
Figure 2.8. The 5-DOF manipulator displacement transmissibility under harmonic and random vibration. Indicated points are explained in Table 2.2.....	19
Figure 3.1. Schematic of the cantilever beam with the actuator force applied at one-third its length from the base.....	22
Figure 3.2. Schematic of a two-link two-joint manipulator (2L2JM).....	26
Figure 3.3. The 5-DOF manipulator mesh results in FEA-A workbench.....	35
Figure 3.4. The Cantilever beam mesh results in FEA-A workbench.	36
Figure 3.5. The 2L2JM mesh results in FEA-A workbench.....	37

Figure 3.6. Master DOF extraction for the 4th mode of the 5-DOF manipulator.....	41
Figure 3.7. Master DOFs of the manipulators. The vertical displacements are represented with green arrow, while the rotational displacements are shown by orange curved arrows. (a) Master DOFs of the cantilever beam. (b) Master DOFs of the 2L2JM. (c) Master DOFs of the 5-DOF manipulator.	42
Figure 3.8. Cantilever beam’s tip displacement and moment for 3 different state-space models as well as FEA-A transient. a- the response for small time duration, for comparison, b- the response for 0.5 second interval, c- an arbitrary excitation moment between [-10,10] N-m applied on L/6 of the beam.....	47
Figure 3.9. cantilever beam, full order model, a. Observability Gramian and b. Controllability Gramian.....	49
Figure 3.10. Cantilever beam, balanced full order model, a. Observability Gramian and b. Controllability Gramian.	50
Figure 3.11. 2L2JM’s tip displacement and moment for 3 different state-space models as well as FEA-A transient. a- the response for small time duration, for comparison, b- the response for 0.5 second interval, c- an arbitrary excitation moment between [-10,10] N applied on L/3 of the first link.	52
Figure 3.12. 2L2JM, full oscillatory model, a. Observability Gramian and b. Controllability Gramian.....	54
Figure 3.13. 2L2JM, balanced-full oscillatory model, a. Observability Gramian and b. Controllability Gramian.	55
Figure 3.14. 5-DOF manipulator tip displacement and moment for 3 different state-space models as well as FEA-A transient. a- the response for small time duration, for comparison, b- the response for 0.2 second interval, c- an arbitrary excitation force between [-2,2] kN applied on the base.	57

Figure 3.15. 5-DOF manipulator, full oscillatory model, a. Observability Gramian and b. Controllability Gramian.	59
Figure 3.16. 5-DOF manipulator, balanced-full oscillatory model, a. Observability Gramian and b. Controllability Gramian.	60
Figure 4.1. Structure of a LQR state feedback controller.	63
Figure 4.2. Vibration response of a cantilever beam due to an impulse moment exerted at $L/6$ from its base at zero-time, (a) tip displacement of the open loop systems, (b) tip displacement of the closed loop systems, (c) the controller effort.	66
Figure 4.3. Vibration response of a cantilever beam due to an arbitrary vibration $[-10,10]$ Nm moment exerted at $L/6$ from its base. (a) tip displacement of the full order systems. (b) tip displacement of the reduced order systems.	67
Figure 4.4. Vibration response of the closed loop cantilever beam systems due to an arbitrary vibration $[-10,10]$ Nm moment exerted at $L/6$ from its base. (a) tip displacement of the full order systems. (b) tip displacement of the reduced order system.	68
Figure 4.5. Cantilever beam results, (a) controller efforts of the full order and reduced order closed loop models (FCL and RCL), (b) disturbance as an arbitrary vibration $[-10,10]$ Nm moment exerted at $x=L/6$	69
Figure 4.6. Bode diagram of the cantilever beam; (a) full order open loop and closed loop systems. (b) full order closed loop and reduced order open loop systems. (c) reduced order open loop and closed loop systems.	71
Figure 4.7. 2L2JM results, (a) tip displacement of the full order open loop and closed loop models (FOL and FCL), (b) zoomed closed loop tip displacement, (c) disturbance as an arbitrary vibration $[-10,10]$ N linear force exerted at $x=L/3$ of the first link.	75
Figure 4.8. 2L2JM full order model results, (a) joint 1 controller effort, (b) joint 2 controller effort.	76

Figure 4.9. 2L2JM results, (a) tip displacement of the reduced order open loop and closed loop models (FOL and FCL), (b) zoomed closed loop tip displacement, (c) disturbance as an arbitrary vibration [-10,10]N linear force exerted at $x=L/3$ of the first link.....	78
Figure 4.10. 2L2JM reduced order model results, (a) joint 1 controller effort, (b) joint 2 controller effort.	79
Figure 4.11. Bode diagram of the 2L2JM, (a) full order open loop and closed loop systems, (b) reduced order closed loop and open loop systems.....	80
Figure 4.12. 5-DOF manipulator results, (a) tip displacement of the full order open loop and closed loop models (FOL and FCL), (b) zoomed closed loop tip displacement, (c) disturbance as an arbitrary vibration [-2000,2000]N linear force exerted at the base.....	82
Figure 4.13. 5-DOF manipulator full order model results, (a) joint 1 controller effort, (b) joint 2 controller effort.	84
Figure 4.14. 5-DOF manipulator results, (a) tip displacement of the full order open loop and closed loop models (FOL and FCL), (b) zoomed closed loop tip displacement, (c) disturbance as an arbitrary vibration [-2000,2000]N linear force exerted at the base.....	85
Figure 4.15. 5-DOF manipulator reduced order model results, (a) joint 1 controller effort, (b) joint 2 controller effort.....	86
Figure 4.16. Bode diagram of the 5-DOF manipulator, (a) full order open loop and closed loop systems, (b) reduced order closed loop and open loop systems.	87
Figure 5.1. Equipment for displacement measurement, (left) B&K type 4370 accelerometer, (right) B&K 2635 charging amplifier.	90
Figure 5.2. The circuit to map the -5 to +5 VDC converts to 0 to 5 VDC [36].....	90
Figure 5.3. Fast Fourier transform of the Accelerometer output, when stimulated at 5 and 10 Hz.	91
Figure 5.4. Fast Fourier transform of the Laser output, when stimulated at 5 and 10 Hz.	92

Figure 5.5. Shaker displacement measured by the accelerometer and Laser sensors..... 93

Figure 5.6. Torque-velocity profile from stepper motor datasheet [44]. 95

Figure 5.7. Torque measurement setup for stepper motor field of operation experiment. 96

List of abbreviations

2L2JM	2-link-2-joint-manipulator
BMDC	Balanced-Matched-DC (reduction algorithm)
DOF	Degree-of-freedom
EE	End-effector
FEM	Finite-element-method
FEA-A	Finite-element-analysis through ANSYS
FFT	Fast-Fourier-transform
FIR	Finite impulse response filter
FLM	Flexible-link-manipulator
H_∞	H infinity (Refers to Hardy space infinity norm)
I/O	Input-and-output
LQR	linear-quadratic-regulator
MIMO	Multi-input-multi-output
PSD	Power spectral density
PWM	Pulse Width Modulation
RMS	Root Mean Square
SISO	Single-input-single-output

List of symbols

ζ	Damping coefficient (N.s/m)
θ_{link}	joint angle of <i>link</i> (rad)

ρ	Density (kg/m ³)
φ	Hermit shape function
ω	excitation frequency (rad/s)
ω_n	n_{th} Natural frequency (Hz)
A	State matrix
\tilde{A}	Transformed state matrix
B	Input matrix
\tilde{B}	Transformed input matrix
C	Output matrix
\tilde{C}	Transformed output matrix
D	Feed-forward matrix
E	Modulus of elasticity (Pa)
Ele	Element
F	External moment (N.m)
G	Plant transfer function
K	Global stiffness matrix (N/m)
K_i	stiffness matrix of the i_{th} element
K_c	controller transfer function
L	link total length (m)
M	Global Mass matrix
M_i	Mass matrix of the i_{th} element (kg)
P	Generalized system transfer function
Q	State weighting function

R	Input weighting function
S	Sensitivity transfer function
T	Gramian transformation matrix
U	input vector
V	The solution of Riccati equation
W_c	Controllability Gramian
W_o	Observability Gramian
W_s	Sensitivity weighting function
W_u	Actuator weighting function
X	State vector
Y	Output vector
$\vec{Z}^{(n)}$	nth mode shape
$[Z]_{modal}$	Modal matrix
a	cross-section area (m ²)
b	Base displacement (m)
c	damper constant (N.s/m)
e	End-effector displacement (m)
f	Final node of each link
g	Number of outputs
h	Number of inputs
i	number of a node

j	imaginary unit ($\sqrt{-1}$)
k	spring stiffness (N/m)
l_{ac}	Accumulated length, or the distance from the base to point (x, y) (m)
l_{el}	length of element (m)
$link$	The number of link for the 2-link manipulator
m	point mass (kg)
n	Number of degrees of freedom
o_i	Location of a node on the undeformed link
q	generalized coordinate
r	position of a point in i_{th} element (m)
s	Laplace complex variable
t	time (s)
u	displacement of node (m)
v	slope of node (rad)
x_i	Horizontal axis of i_{th} element fixed to undeformed link
x	Coordinate of a point on x_i axis (cantilever)
x_{link}	Coordinate of a point on $x_{i,link}$ axis (2-link manipulator)
y_i	vertical axis of i_{th} element fixed to undeformed link
y	Coordinate of a point on y_i axis (cantilever)
y_{link}	Coordinate of a point on $y_{i,link}$ axis (2-link manipulator)
z_i	i_{th} element's generalized coordinate
z_{pn}	n_{th} principal coordinate

Chapter 1. Introduction

1.1 Motivation

It has been predicted that humanity's demand for food and resources will increase in the future. It is clear that not only should available resources be managed for the future, but also the quality and quantity of food productions should be increased. Improving breeding techniques through phenotyping is one of the most important tasks to prepare enough food resources for the next generation. This includes measuring characteristics of crops such as a plant's height, temperature, and vegetation indices. Engineers from different areas like mechanical engineering, electrical engineering, and computer scientists are trying to make progress and improvements in phenotyping research [1].

Data collection through plant phenotyping needs to be done for different types of farm fields. The monitoring is performed using different vehicles, (unmanned aerial vehicles) UAVs, and mobile robots [2]. The motivation of this study was to develop a vehicle for automated crop monitoring. A 5-DOF manipulator was already developed in-house and is going to be installed on a mobile robot for autonomous travelling on a farm/breeding field. The manipulator develops vibration when the mobile robot, which carries it, traverses a rough farming terrain. In this thesis vibration transmitted to the EE of the manipulator was studied.

1.2 Background

A five-degree-of-freedom (5-DOF) robot manipulator for agricultural applications was developed by previous members of the robotic lab at the University of Saskatchewan. The manipulator was designed to be installed on a mobile base vehicle for monitoring targeted crops in a farm field using sensors installed on its tip.

The degrees of freedom of the manipulator are illustrated on Figure 1.1. The first degree of freedom controls the yaw angle of the manipulator. It is located on the base of the arm. The 2nd and 3rd joints are on top of the base. The 2nd joint is for back-and-forth motion of the upper arm,

while the 3rd joint is for pitch angle adjustment of the upper arm. The 4th joint is a prismatic joint and is defined for upper arm elongation. The 5th joint is for the pitch angle of the EE.

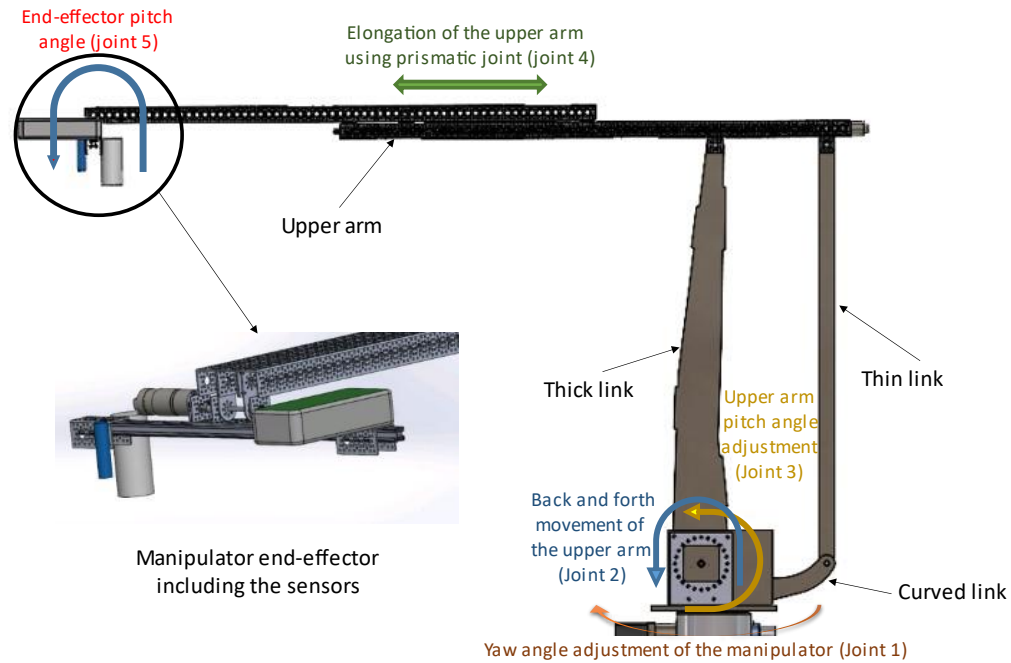


Figure 1.1. 5-DOF manipulator of U of S.

1.3 Problem statement

The manipulator has been designed to be light. In particular, the linear actuator was made up of aluminum c-channels with many holes. Thus, the stiffness of the upper arm is very low and susceptible to vibrational forces. This part of the beam could be characterized as a cantilever beam with a mass at the free end. When the manipulator mobile base moves along the field, vibration is induced from farm terrain to the base of manipulator. Thus, the sensors mounted at the end-effector (EE) of the manipulator will not record data accurately.

In order to address the problem, vibration needs to be suppressed. One possible way is to use passive vibration suppression system (open-loop system). Due to the characteristic of the manipulator which needs to change its configuration during operation, it is difficult to add vibration-isolators or absorbers. Another possible solution could be through adhesive dampers to be attached to the links. Since the vibration is due to the flexible links and not the joints, the

vibration of the upper arm could be attenuated by adding adhesive dampers to the link. However, this means more mass is added to the upper arm in addition to wiring; therefore, this was deemed not to be acceptable. Therefore, active vibration suppression (closed-loop system) was selected for this manipulator. In other words, a controller was designed and implemented so that one or two joints would operate to damp the vibration of the EE. Therefore, in this thesis, the designed controller used the 2nd and 3rd joints and all other joints were considered fixed.

1.4 Literature review

Active vibration control of flexible link manipulators (FLM), similar to any control problem, requires mathematical modeling and a controller design. However, there are a few control schemes that can be implemented without the need for mathematical modeling. One simple and non-model-based approach for vibration suppression of FLM is by means of strain gauge measurement. In this approach the gravity liberated strain of the clamped side of the FLM is fed to the controller. Based on that, Phung *et al.* [3] applied a multi-layer perceptron neural network (MLP NN) for forward and inverse kinematics of a 3-DOF FLM under gravity. For the vibration suppression task, the mean liberated strain is fed to the P-action controller in the cascade controller. In another study on the same FLM, a cascade control scheme for position and vibration suppression is proposed by Malzahn *et al.* [4]. They implemented two different control approaches based on direct strain feedback or DSFB. One was a half integrator controller for joint positions and the other was the classic proportional controller for the joint velocities. In order to eliminate the effect of gravity on the strain gauge measurement, the mean liberated strain was derived through a finite impulse response filter (FIR filter). In another study, Njery *et al.* [5] used a NN to tune the gain of DSFB (direct strain feedback) for bending and torsional vibration control of a 3-DOF FLM in the presence of gravity. Another non-model-based approach is through Iterative Learning Control (ILC). It is a simple method for control of repetitive motions such as periodic vibration. In other words, the controller performance is improved by learning from past experience. In this regard, Meng *et al.* [6] implemented a PD-type boundary ILC law for vibration control of a 1-DOF FLM with command torque being exerted on the joint. The same authors in another publication [7] implemented ILC with consideration of input saturation of the joint torque. Regarding Neural Network modeling, Jamali *et al.* [8] investigated modeling of a 2-DOF FLM. Then, in another

publication [9], two PID controllers for each link were designed for vibration and motion control. The vibration of the links was measured by accelerometers at the end of each link and suppressed by PZT (piezo-electric) actuators. For each PID controller, a P-type iterative learning algorithm was designed for online gain tuning. Although non-model-based control schemes are capable of vibration attenuation, there is a low confidence on controller performance and system stability [10].

Among model-based active control studies, the AMM (assumed mode method) and FEM (Finite element method) modeling are of interest. Based on the first method, Pereira *et al.* [11] presented a double-loop control scheme for motion and vibration control of a 1-DOF FLM. The inner loop is a PD-controller while the outer loop is a zero-order controller called integral resonant control. In similar studies, authors of [12]–[15] used different methods such as classic controller, SMC (sliding mode control), SDRE (State-Dependent Riccati Equation), and a fuzzy sliding mode controller to attenuate the EE vibration of a 1-DOF FLM. In [16] Nestorović *et al.* a multi-input-multi-output (MIMO) model of a piezoelectric cantilever beam was obtained based on the subspace algorithm. Then they used a linear quadratic regulator (LQR) to control the vibration of the beam's end. For a wind tunnel cantilever sting (being treated as a cantilever beam), Shen *et al.* [17] fitted a transfer function to a measured frequency response of the first mode of vibration. Then a PID controller was used, and controller gains were tuned using a neural network.

The above studies were for manipulators with relatively simple geometry. To deal with more complex geometry, it is better to take advantage of FEM; besides, it is computationally efficient for model-based real-time control [18]. Based on the Newmark method for solving FEM, Karagülle *et al.* [19] presented a simple residual vibration damping for a 2-DOF FLM. In another study, Dubay *et al.* [20] presented an active vibration controller using MPC (model predictive control). First, the FEM model of a 1-DOF manipulator is derived, then a finite element based MPC is obtained and is solved using the Newmark approach. The manipulator is controlled with a joint's motor and a linear piezoelectric actuator. In [21], Shao *et al.* presented an impulse controller to control the forced harmonic excitation of a 1-DOF flexible-link flexible-joint manipulator. Given LQR control, the manipulator takes advantage of a pair of piezoelectric actuators. To reduce computational cost, a reduced model is applied by increasing the inertia of the hub. Khot *et al.* [22] used finite element analysis (FEA) to obtain eigenvectors of a cantilever

beam. They obtained a reduced state-space model of the beam using principal coordinates. They also used linear optimal control to suppress the beam's tip vibration. Using FEA and Hamilton's principle, the authors of [23] obtained mathematical model of a cantilever beam and implemented combination of a classic controller and fuzzy logic for vibration control of the beam's tip. Similarly, Kamel *et al.* in [24] suppressed vibration of a cantilever beam using FEA and fuzzy-classic controllers. In a recent paper [25], Ebrahimi *et al.* utilized a so-called L1 adaptive-controller for a model obtained using finite-element for a cantilever beam and controlled its vibration. Hatch in [26] studied a state-space model reduction of a flexible link manipulator (FLM). According to this work, balanced realization with the help of Match-DC-Gain model reduction is applicable for MIMO systems.

Among mathematical modeling found in the literature and reported here, finite element modelling seems to be the most suitable; however, it results in a large model, which may be difficult for the controller in terms of computational cost. It is worth mentioning that in some articles the actuator to control the vibration of the link is a PZT actuator, which is not applicable for the 5-DOF manipulator.

Manipulator modeling was studied in this thesis through FEA with the focus of model reduction to improve the controller performance. Besides, unlike most of the cases in the literature, only joints would operate in the present study to suppress the vibration of the manipulator.

1.5 Objectives

The research question is: Do we need active vibration control for the 5-DOF mobile-manipulator developed for an agriculture setting?

When the vehicle is moving on an agricultural setting, the 5-DOF mobile-manipulator shows vibration due to its large size and flexibility. Therefore, the sensors mounted on the EE of this manipulator have difficulty recording phenotyping data accurately. The linear actuator of the manipulator with relatively lower stiffness is more prone to vibration. To address this issue, there is a need to damp the vibration of the manipulator, particularly due to its prismatic joint (slider pair). This overall objective can be divided into the following sub-objectives:

1. Evaluation of the amplitude of vibration experienced by the manipulator; if vibration is deemed to be excessive, then

2. Design active vibration control with several control algorithms to minimize vibration of the manipulator's EE.

The research is divided into 3 main sections: modeling, control, and experimental testing.

1.6 Methodology

1. For the first objective, for the free vibration evaluation, first, the natural frequencies and mode shapes of the 5-DOF manipulator were obtained using finite element analysis (FEA), with the commercial FEA software ANSYS (FEA-A). Then, a comparison was made between the numerical values and experimental modal analysis. A similar effort was done by another group member [27]. They obtained the natural frequencies and mode shapes of the manipulator using the software and verified those results by a hammer test. However, that part of the program was not reported in this thesis.

Then, forced vibration analysis of the arm was studied while its base (tractor) was moving. This is done using simulation (FEA-A). Then, displacement transmissibility (ratio of EE's displacement over maximum base displacement) using simulation was obtained.

2. For the second objective, the first step to obtain the model of the manipulator was to use finite element method (FEM), then active vibration control for the manipulator was achieved. For this purpose, a few control approaches (particularly, LQR and H_∞ controllers) were explored and simulations were done in a commercial software called MATLAB (here referred to as M-software). The control inputs were applied only on the 2nd and 3rd joints (see Figure 1.1).

3. The experimental tests were limited to implementing the input and output of the closed loop system. A look-up table was generated for experimental study of the stepper-motors as the inputs. Besides, the accelerometer was calibrated as a measurement unit or output.

1.7 Key contribution of thesis

The focus of this study was on modeling and vibration control of the 5-DOF manipulator. Although the approach used in this thesis is not new, some novelty can be attributed to implementing this approach for such a large 5-DOF manipulator, with a reach of about 3-meters. The contributions of this research can be listed as follows.

1. The dynamic modeling of the 5-DOF manipulator using master DOFs (numerical FEM) was the main contribution of this thesis. It modeled the complex robotic structure of the novel 5-DOF manipulator. Unlike other literature that simplify the model to a cantilever beam or a 2-link-manipulator, the modeling dealt with the actual model of the manipulator. In addition, the FEM modeling through master DOFs has been used for a one DOF manipulator in the literature; however, the manipulator in this thesis dealt with five DOFs.
2. The mathematical modeling was verified using FEA-A software; the model was also reduced to provide a better performance for the controller.
3. The controller took advantage of 2 joints, unlike most of the literature reviewed that used a PZT actuator to provide moments for the link or moving one joint.
4. Another contribution is paving path for forced vibration evaluation of the 5-DOF manipulator. For experimental implementation, a look-up table was created for the actuators to give the proper amount of torque at a certain rotational speed and acceleration.

1.8 Outline of the thesis

This thesis has 5 chapters. Chapter 1 introduces the 5-DOF manipulator and discusses the problem of the manipulator during operation. It also specifies the methodology to address this issue based on the efficient methods provided in the literature.

Chapter 2 is devoted to the 1st objective. In this chapter, free vibration evaluation was done using the modal module of FEA-A to obtain the natural frequencies and mode shapes of the 5-DOF manipulator. However, for the forced vibration evaluation, displacement transmissibility of

the EE was evaluated. In other words, the ratio of the EE's vibratory displacement over that of the base was tested. This value was obtained and verified using the harmonic and transient modules of FEA-A. First, using the harmonic module the base was excited harmonically, and the ratio was recorded as a frequency response diagram. Second, in the transient module, base was excited via random vibration and the EE's displacement was recorded. Then, using a PSD (power spectral density) approach, the ratio in frequency domain was obtained.

In Chapter 3, manipulators modeling was studied which covers a part of the 2nd objective. The modeling approach was performed on 3 different flexible geometries: a Cantilever Beam, a 2L2JM, and a 5-DOF manipulator. The models for the first two geometries were obtained using manual FEA and verified through the modal module of FEA-A. However, due to the complexity of the 5-DOF geometry, the FEA model was only obtained from FEA-A eigenvectors. Then a reduction algorithm was applied on the obtained models. To verify the state-space models, FEA-A transient analyses were compared to the state-space models.

Chapter 4 relates to the controller design, which covers the rest of the 2nd objective. For the vibration control, LQR was applied to the cantilever beam model and H_∞ controllers were applied to the 2L2JM and 5-DOF models.

Chapter 5 discusses implementation of the designed controller on the real arm (3rd objective). The manipulator's inputs were assumed to be the 2nd and 3rd joints, which were run with stepper motors. The output was assumed to be the acceleration measured by the accelerometer at the EE.

Chapter 2. Vibration Evaluation

In this chapter, the amplitude of manipulators' vibration was evaluated. In this regard, first, free and forced vibration evaluation of the 5-DOF manipulator were studied. Then, based on the results a decision was made if the active vibration was needed for the vibration suppression of the manipulator.

2.1 Free vibration evaluation

If a system vibrates due to an initial disturbance and no external force, the vibration is known as free vibration. On the other hand, if the system is subjected to external force the vibration is known as forced vibration. Based on [28], the equation of motion for the vibration of an undamped system is:

$$[M]\ddot{\vec{q}} + [K]\vec{q} = 0 \quad 2-1$$

where $[M]$ and $[K]$ are the mass and stiffness matrices, and q is the vector of generalized coordinates. The general solution of the differential equation would be:

$$\vec{q}(t) = \sum_{n=1}^{\eta} \vec{Z}^{(n)} \beta_n \cos(\omega_n t - \phi_n) \quad 2-2$$

where $\vec{Z}^{(n)}$ and ω_n are the n th mode shape and natural frequency, respectively. The number of modes extracted are from 1 to η (last extracted mode). β_n and ϕ_n are constants.

Free vibration evaluation is referred to as finding natural frequencies and mode shapes of a structure. These values are obtained using hammer test or modal module of FEA-A. In this regard, the CAD model of the 5-DOF was modeled in SolidWorks. Then it was meshed in the modal module of FEA-A. This analysis assumed a fixed base and fixed joints for the manipulator. The analysis parameters are as follows:

1. The material for the upper arm and the EE was Aluminum Alloy, and other components were structural steel. The properties were given in Table 2.1.

Table 2.1. Material properties for FEM modeling

	Density (kg/m ³)	Young's Modulus (Pa)
Aluminum Alloy	2770	7.1e10
Structural steel	7850	2e11

2. The mesh was given in Figure 2.1. The mesh method and sizing were automatically chosen by the software; however, a refinement was defined on the thin link. The properties were extracted from modal solution information. The contact between the parts was modeled using CONTA174, which was a 3-D 8-Node Surface-to-Surface Contact element. Moreover, the joints were revolute MPC184 and were fixed. For the manipulator body, elements used were SOLID186, and SOLID187 which were 3-D 20-Node Structural Solid, and 3-D 10-Node Tetrahedral Structural Solid, respectively. Moreover, TARGE170 was used to define the boundary of a deformable body associated with contact elements. Mesh statistics are as follows:

Number of total nodes = 179975

Number of solid elements = 60366 (SOLID186, and SOLID187)

Number of total elements = 145390 (including contacts and solid elements)

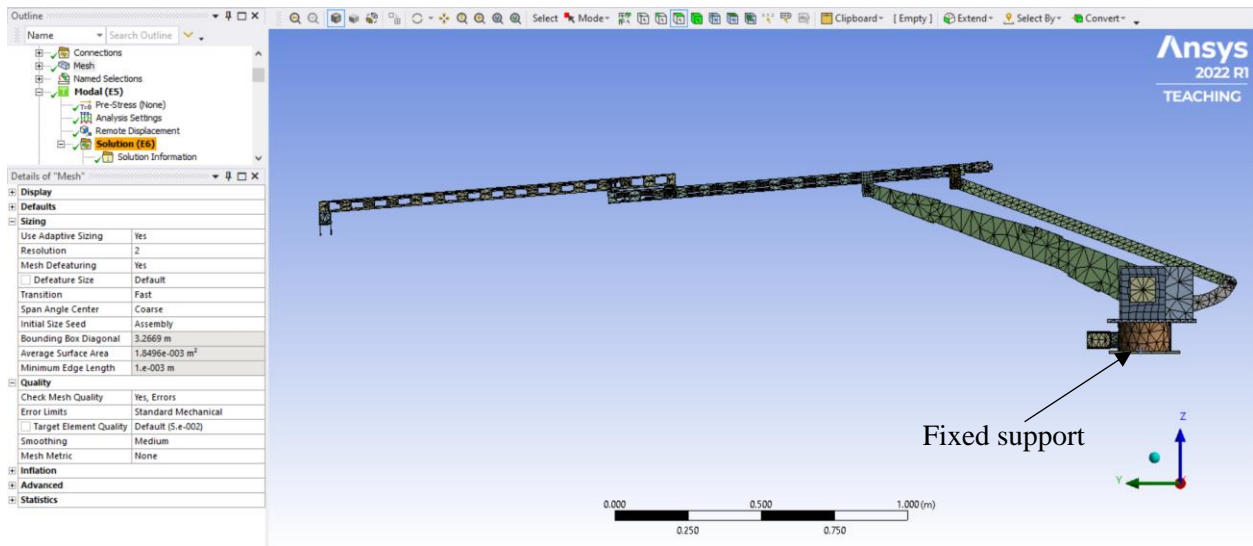


Figure 2.1. The 5-DOF manipulator mesh results in FEA-A workbench.

3. The boundary conditions were fixed support (as shown in Figure 2.1) at the base that was defined with remote displacement to avoid support-plate vibration. Besides, all joints were defined as bounding not to rotate.

The result of the modal analysis, *i.e.*, the natural frequencies of the manipulator were shown in Table 2.2.

Table 2.2. Natural frequencies and mode characteristics of the 5-DOF manipulator (fixed base and joints).

Mode number	Natural frequency [Hz]	Mode characteristic
1	8.312	1 st Lateral
2	9.797	1 st Vertical
3	22.02	2 nd Lateral
4	27.11	2 nd Vertical
5	35.96	3 rd Vertical
6	47.68	3 rd Lateral
7	51.31	4 th Vertical
8	60.11	Ball screw vertical mode
9	62.36	Ball screw lateral mode
10	64.95	4 th Lateral

The manipulator first 10 mode shapes were given in Appendix A. To clarify the lateral and vertical modes of the 5-DOF manipulator with fixed joints and base, refer to Figure 2.2 and Figure 2.3, respectively.

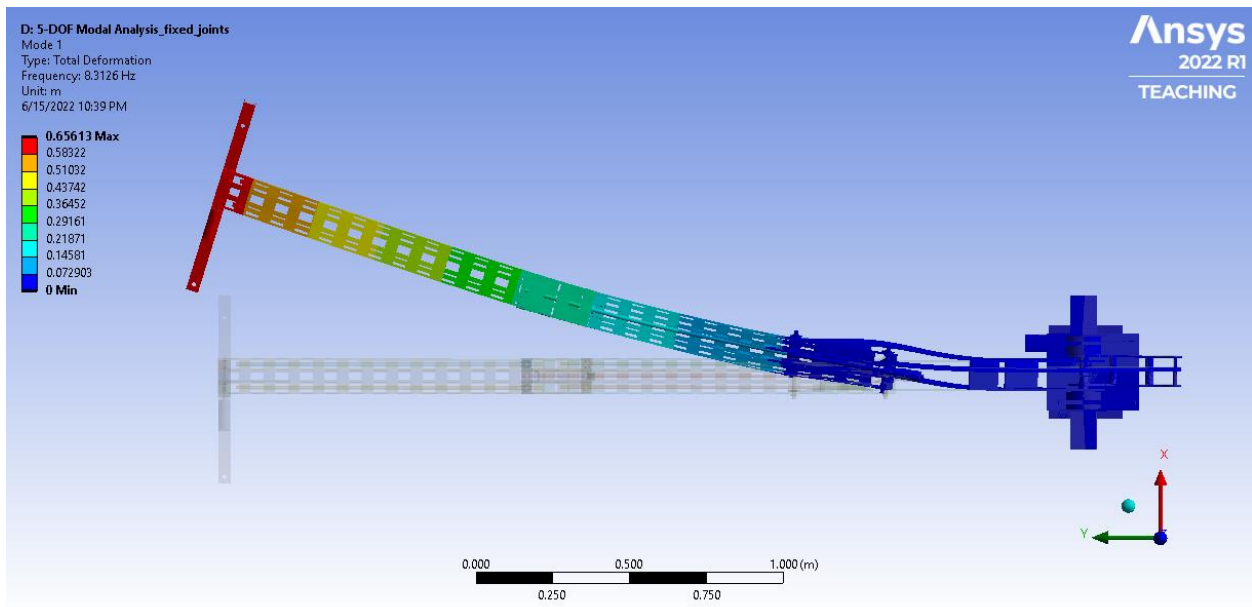


Figure 2.2. Plan view of first mode of the 5-DOF manipulator with fixed base and joints (1st lateral).

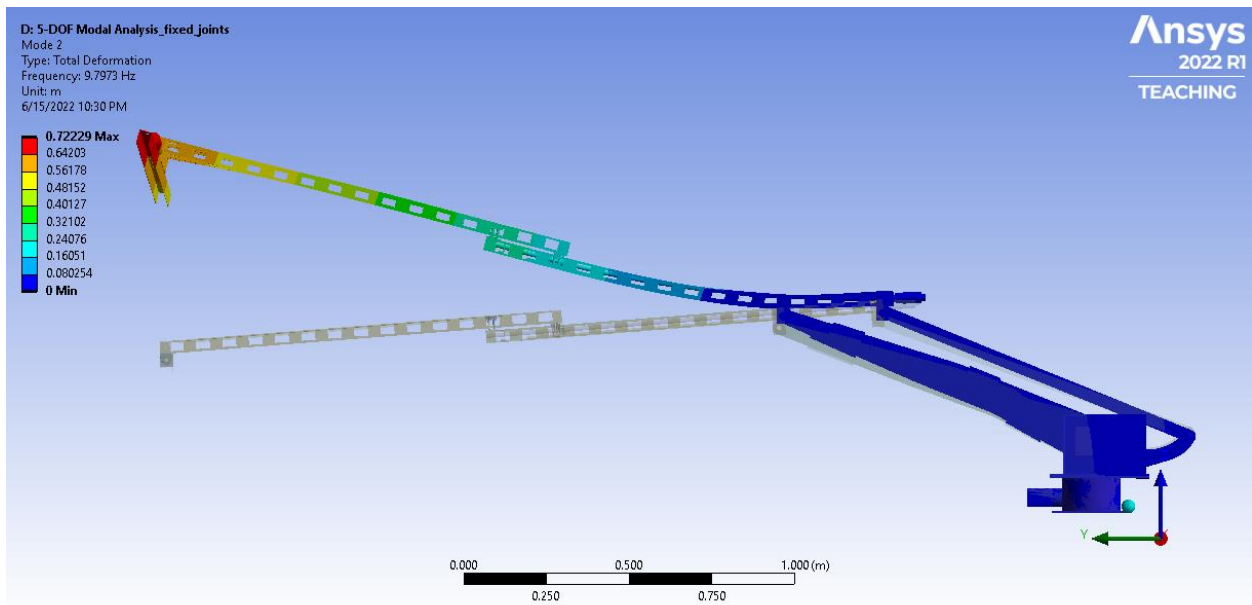


Figure 2.3. Side view of second mode of the 5-DOF manipulator with fixed base and joints (1st vertical).

The lateral modes, especially for higher frequencies were mixed with the vertical modes. This would have adverse effect on the sensor measurement for vertical motion of the EE. However, the active vibration suppression was only able to attenuate the vertical modes, i.e., the 2nd, 4th, 5th, and 7th. Since, The manipulator's 2nd and 3rd joints were only capable of moving the EE in the vertical

direction and not lateral ones. Therefore, the vertical modes were studied for vibration suppression of the EE.

It was noteworthy that the vertical modes of the manipulator with fixed base and joints were studied only in Chapter 2 for vibration evaluation, and the vertical modes of the manipulator with free base and free joints (2nd and 3rd joints) were studied for modeling and controller design.

2.2 Forced vibration evaluation

To evaluate the amount of EE vibration caused by the base vibration, displacement transmissibility is defined. Since the main contribution of this thesis was manipulator modeling and active vibration control, the analytical displacement transmissibility was briefly defined, and the values were obtained by FEA-A. As mentioned earlier, the 5-DOF manipulator is installed on a mobile robot or a tractor. For simplicity the manipulator could be assumed as a mass-damper-spring system which is attached to a moving base as shown in Figure 2.4.

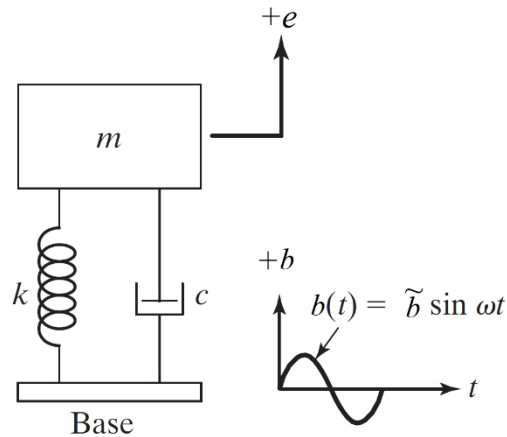


Figure 2.4. Mass-damper-spring model of the manipulator with moving base.

According to Rao [28], when the mass-damper-spring system undergoes base excitation, the equation of motion of the system is as follows:

$$m\ddot{e} + c(\dot{e} - \dot{b}) + k(e - b) = 0 \quad 2-3$$

If the base is in harmonic excitation, then

$$b(t) = \tilde{b} \sin \omega t \quad 2-4$$

This results in the mass moving with the same frequency but with a phase difference as:

$$e(t) = \tilde{e} \sin(\omega t - \phi) \quad 2-5$$

The ratio of the displacement amplitudes is called displacement transmissibility.

$$T_d = \frac{\tilde{e}}{\tilde{b}} = \sqrt{1 + \left(\frac{2\zeta\omega}{\omega_n}\right)^2} |H(j\omega)| \quad 2-6$$

where $H(j\omega)$ is the complex frequency response. The parameters j , ω and ζ are the imaginary number, the frequency of excitation, and damping coefficient, respectively.

The harmonic module of FEA-A is based on modal superposition which is explained in section 3.3. Time integration for this module was based on the semi-discrete Newmark method [29]. Using this module, the base was excited by harmonic displacement with a base displacement of 1cm enforced over the frequency range of [0.1,100] Hz. The reason for 1 cm was that the base excitation in a real harmonic test (not simulation) for such manipulator would be chosen around this value; also, the frequency range would cover the natural frequencies in Table 2.2. The frequency response plot of the displacement transmissibility was shown in Figure 2.5. This transmissibility was obtained by dividing the frequency response plot of the EE displacement in the global vertical direction over the constant displacement of the base. As shown in Figure 2.5, the magnitude of the transmissibility for vertical modes were significant; *i.e.*, if the base vibrates at the first vertical mode or the second mode of vibration at 9.80 Hz, the displacement transmissibility will be 45.0 dB, which is $10^{45/20} = 178$. This indicates that if the base vibrates at the second natural frequency, the EE will vibrate more than 177 times as high as the base. Looking at the other modes rather than the vertical ones, someone could observe that the EE has experienced vertical displacement. Since, due to the complexity of the geometry, each mode has a certain amount of vertical motion.

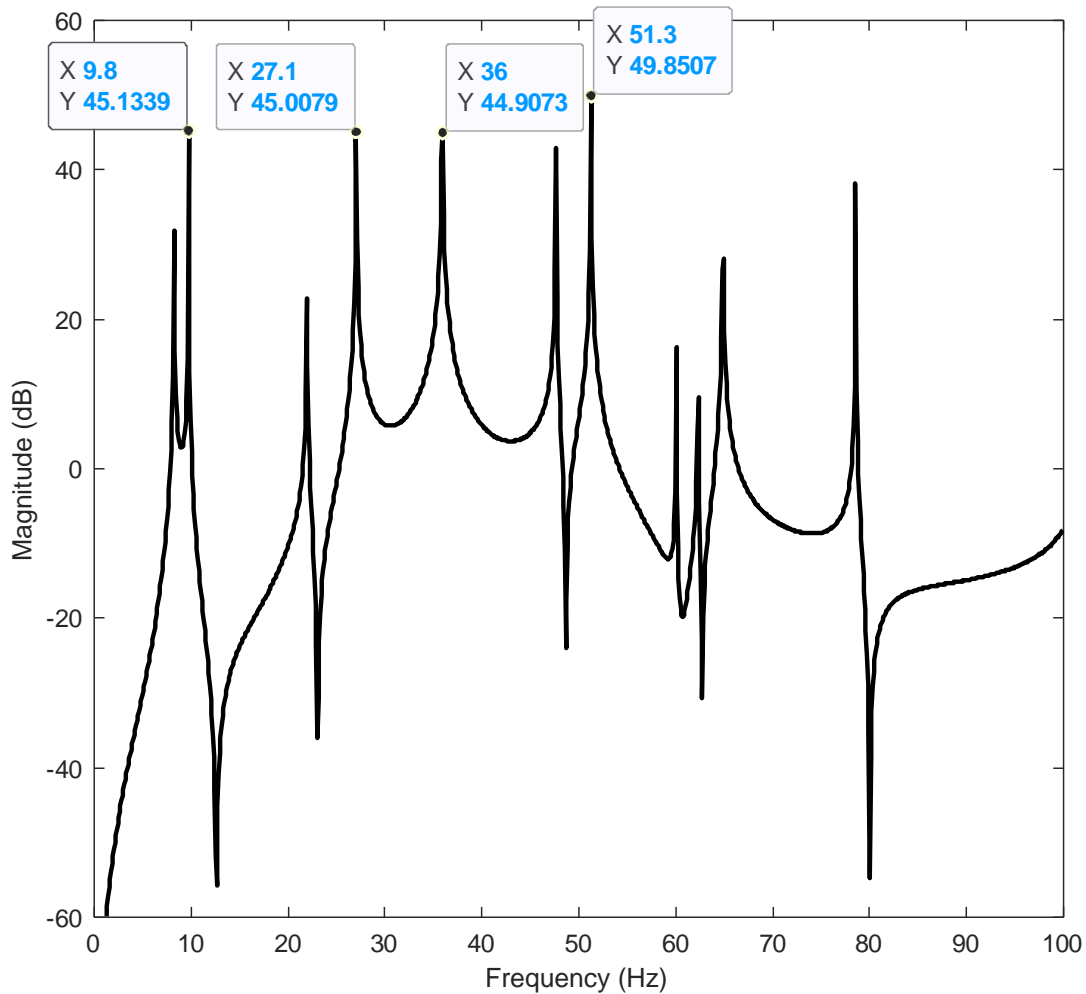


Figure 2.5. 5-DOF displacement transmissibility in frequency domain (EE displacement / base displacement). The base is under harmonic excitation (equation 2-4) over the range of [0.1,100] Hz. The 4 indicated points are the first 4 vertical modes.

When the base is moving on the rough terrain, for simplicity, the excitation could be assumed as random vibration. The random vibration was a white noise, which was generated using the command “rand” in the M-software. Based on the definition, white noise is a signal with the same intensity at different frequencies; i.e., the power spectral density (PSD) of the noise is constant. This noise was generated with the sample rate of 100 Hz for 10 seconds in the range of [-1,1] cm. Although generating data in a longer duration would result in a more reliable signal (covering more

frequencies), more data was not supported by the license for FEA-A. The PSD of the generated noise was obtained by “pwelch” command in M-software without filtering or averaging. The PSD was shown in Figure 2.6. According to the figure, the PSD of the noise varied randomly about -125 dB.

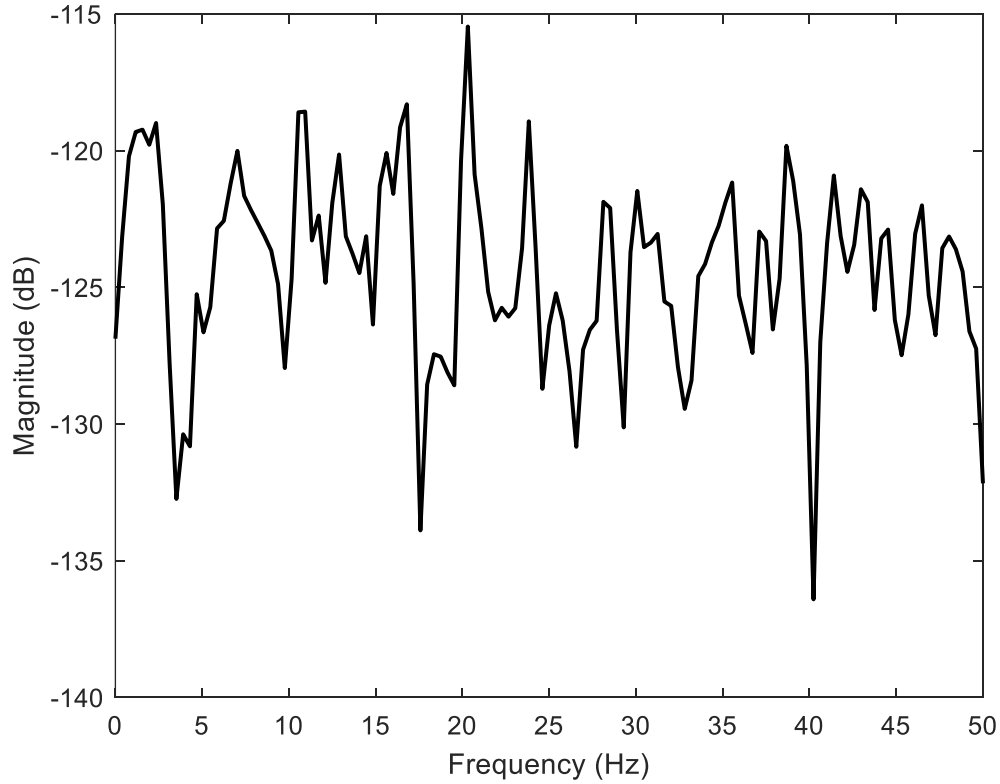


Figure 2.6. PSD of the random vibration for the base excitation.

To obtain displacement transmissibility through random vibration, first, the random excitation was exerted on the base. Then the displacements of the base, and the EE were recorded. Finally, using Welch’s power spectral density (PSD) estimation, the displacement transmissibility was obtained as follows [30]:

$$T_d = \sqrt{\frac{PSD_{EE}}{PSD_{base}}} \quad 2-7$$

Using the transient module of FEA-A a random excitation was applied on the base. Similar to the harmonic module this module was based on mode superposition method. Time integration for this module was based on the semi-discrete Newmark method [29]. This method updates the displacement and velocity of the dynamic equation of motion in each iteration as follows:

$$\dot{x}_{[p+1]} = \dot{x}_{[p]} + [(1 - \delta)\dot{x}_{[p]} + \delta\ddot{x}_{[p]}]\Delta t \quad 2-8$$

$$x_{[p+1]} = x_{[p]} + \dot{x}_{[p]}\Delta t + \left[\left(\frac{1}{2} - \alpha\right)\dot{x}_{[p]} + \alpha\ddot{x}_{[p]}\right]\Delta t^2 \quad 2-9$$

where α and δ are Newmark's integration parameters. In addition, Δt is the timestep, and p stands for the p th iteration. In the Newmark method, the amount of numerical algorithm dissipation can be controlled by γ .

$$\begin{aligned} \delta &= \frac{1}{2} + \gamma \\ \alpha &= \frac{1}{4}(1 + \gamma)^2 \\ \gamma &\geq 0 \end{aligned} \quad 2-10$$

The software enables user to chose γ by “TINTP” command. All over the thesis this value was chosen 0.005 as default.

The program to generate the random vibration, and the displacement transmissibility were given in Appendix F. The base excitation and transmitted vibration to the EE are shown in Figure 2.7. The constant time step for this simulation was 1e-2s.

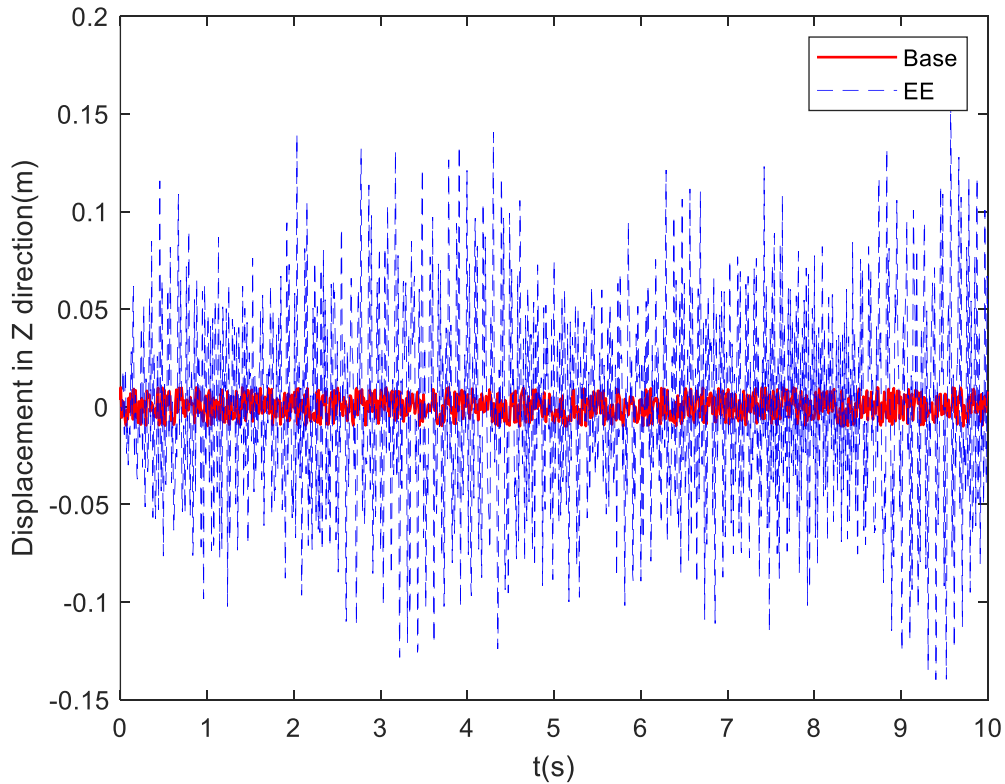


Figure 2.7. The displacement of the base and EE of the 5-DOF manipulator in time domain. the base of the 5-DOF manipulator (see appendix A) is under random vibration (red solid line). This vibration is transmitted to the EE (blue dashed line).

The random vibration for the base and the EE shown in Figure 2.7 were substituted in equation 2-7 to calculate the displacement transmissibility, with the results given in Figure 2.8 (red line). The random vibration result shown here was just one simulation; for more accurate results, more simulations with different random excitations should be conducted and the average considered. According to Figure 2.8, as the frequency increases the peaks of the random excitation separate from the harmonic excitation. That is because of the complexity of the geometry that led to mixture of the modes for the random excitation. Another justification could be due to the fact that the random data was not an ideal white noise. This could have been improved by applying filter to the generated data and including more data points.

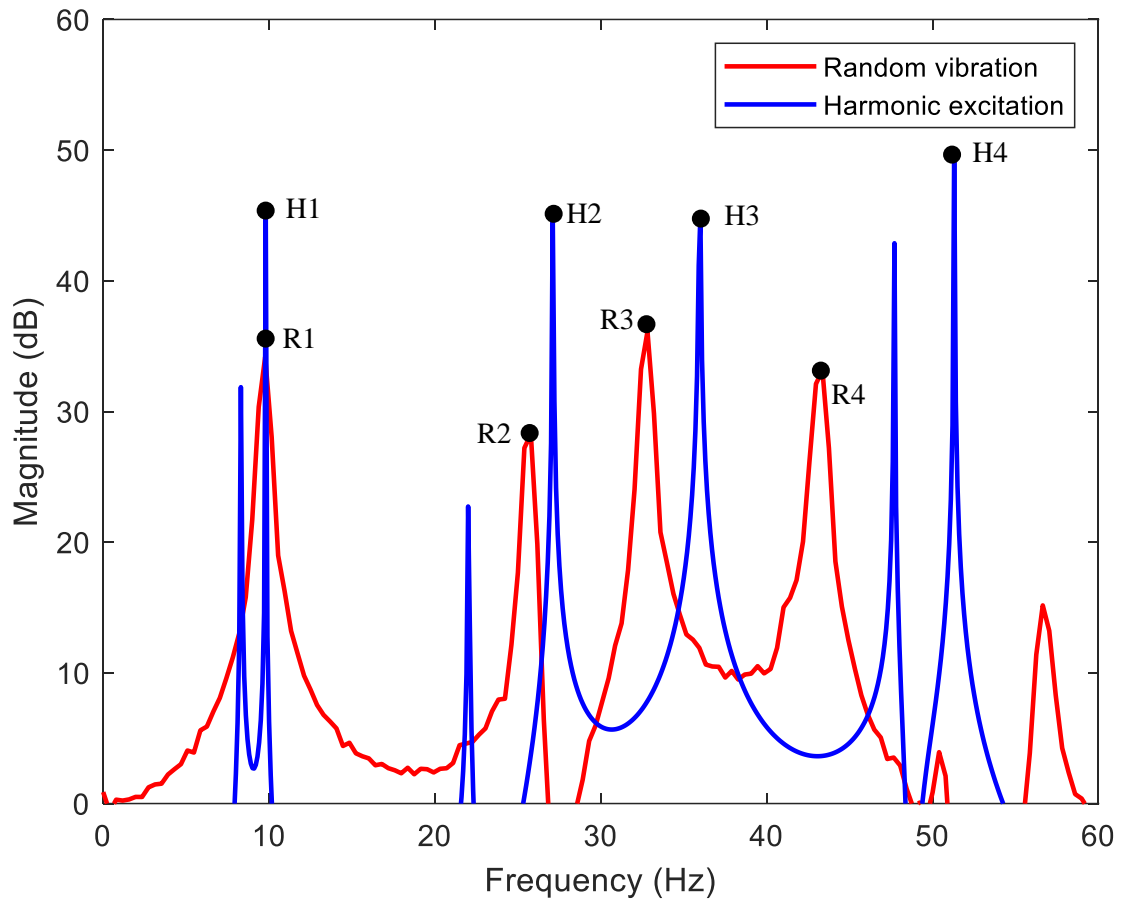


Figure 2.8. The 5-DOF manipulator displacement transmissibility under harmonic and random vibration. Indicated points are explained in Table 2.2.

Table 2.3. Displacement transmissibility of harmonic excitation and random vibration on the base of the 5-DOF manipulator. Indicated points correspond to Figure 2.6.

Mode Characteristic	Harmonic excitation			Random vibration		
	Figure 2-6	Frequency Hz	Magnitude dB	Figure 2-6	Frequency Hz	Magnitude dB
1 st vertical	H1	9.80	45.1	R1	9.76	36.4
2 nd vertical	H2	27.1	45.0	R2	25.8	27.4
3 rd vertical	H3	36.0	44.9	R3	32.4	38.2
4 th vertical	H4	51.3	49.8	R4	42.6	30.5

As shown in Figure 2.8, considering the random vibration (red line), if the base vibrates at 9.76 Hz, the displacement transmissibility will be 36.4 dB which is $10^{36.4/20} = 66.0$. This indicates that if the base vibrates at this frequency, the EE will vibrate more than 60 times as high as the

base. Beside, as shown in Figure 2.8 and Table 2.3, due to the complex structure and mixture of the modes, as the frequency increases, the transmissibility from random excitation does not follow the harmonic excitation. This implies that for vertical vibration suppression, other modes than the vertical ones should also be considered.

2.3 Summary

In this chapter the 5-DOF manipulator vibration was evaluated. For the free vibration evaluation, the natural frequencies and mode shapes were studied. Moreover, the forced vibration evaluation was studied through the displacement transmissibility. The transmissibility from harmonic excitation showed that the vertical vibration transmitted from the base was significant. However, the transmissibility from random vibration not only showed the vibration from the base affected the EE, but it also indicated that all the modes should be considered in vibration suppression. Finally, one could conclude that the vibration transmitted to the EE would be significant and causes inaccurate data acquisition. As stated in the chapter, the vibration transmitted to the EE could be more than 100 times as the base. This necessitated an active vibration suppression for the manipulator's EE.

Chapter 3. Finite Element Model of Manipulators

This chapter is devoted to the FEM modeling of three different manipulators. First, a cantilever beam and a two-link two-joint manipulator (2L2JM) were considered. Using manual FEM, the natural frequencies of the manipulators were derived and verified with FEA-A. Then, using the eigenvectors from FEA-A, a modal matrix was set up. Subsequently, considering the I/O (inputs and outputs) of the system, a state-space model was represented and followed by a model reduction. Finally, using the Solid-works model of the 5-DOF manipulator, its modal matrix was obtained. Then the reduced model of the manipulator was derived. At the end of the chapter the state-space models were tested and verified with the transient module of FEA-A. The models of the three manipulators were used for controller design in Chapter 4.

3.1 Finite element model of a cantilever beam

A cantilever beam has a simple geometry; therefore, it is easy to obtain its equation of motion. Moreover, the purpose of this part is to give credit to FEA-A eigenvalue problem; *i.e.*, the software results are not meant to be trusted alone and should be accompanied by analytical or hand-calculation results. Although more effort could be made to make the cantilever specifications resemble the 5-DOF manipulator's upper arm, the cantilever beam modeled as follows has arbitrary dimensions. Thus, the dimensions of the cantilever beam are assumed to be of a rectangular cross-section, and its specifications are presented in Table 3.1. It is also restricted to move in the x-y horizontal plane, meaning without gravitation.

Table 3.1. Specifications of the cantilever beam.

Length, L (m)	Width (m)	Height (m)	Modulus of Elasticity, E (Pa)	Density, ρ (kg/m ³)	Material
1.0	0.01	0.01	2.0E11	7850	Structural Steel

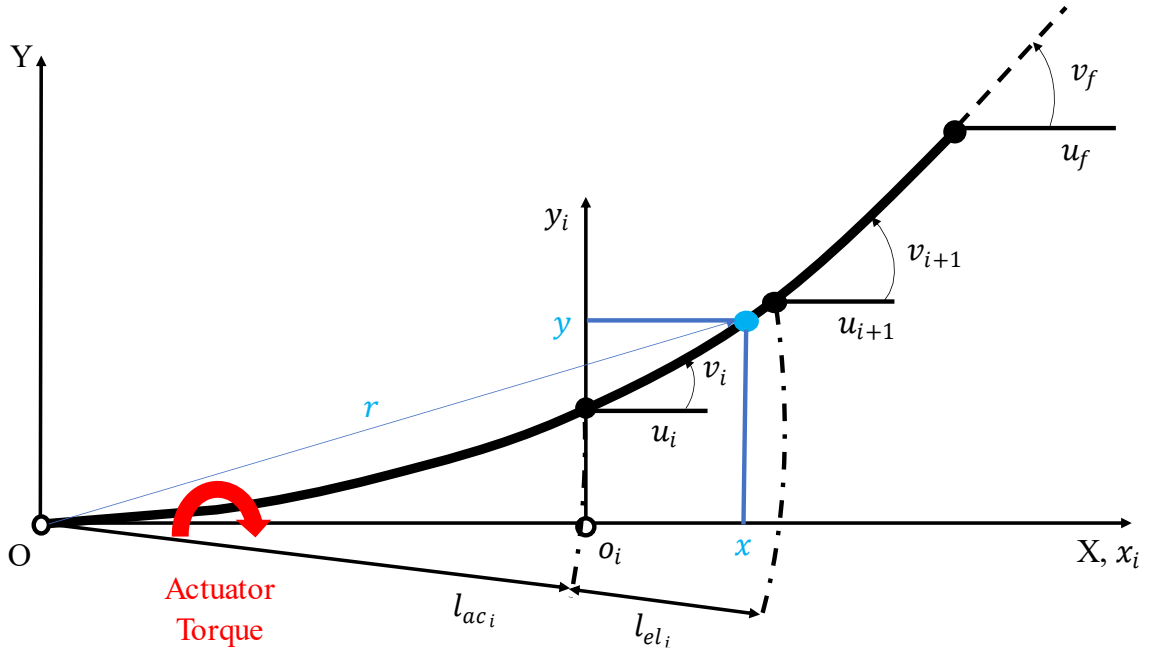


Figure 3.1. Schematic of the cantilever beam with the actuator force applied at one-third its length from the base.

According to the Figure 3.1, (X, Y) is the system of global coordinates, (x_i, y_i) is the system of local coordinates fixed to element i of the undeformed link; also, (x, y) are the local coordinates of a point, l_{ac_i} is the accumulated length, i.e., distance from the base to point (x, y) , l_{el_i} is the length of i th element, (u_i, v_i) are the displacement and slope of node i , and (u_f, v_f) are the displacement and slope of the last node of the beam, respectively.

As shown in Figure 3.1, position of a point in i th element can be represented by r :

$$r = \{ l_{ac_i} + x, y \}^T \quad 3-1$$

Using Hermite shape functions, coordinate y in i th element can be calculated using the following equation:

$$y = \varphi \cdot z_i \quad 3-2$$

where z_i is the i th element's generalized coordinate and φ is the Hermite shape function, which approximates displacements within each element. In Appendix E it is shown how to remove the natural coordinate of the element. The below shape function is based on physical coordinates:

$$\varphi = \begin{pmatrix} 1 - 3x^2/l_{el_i}^2 + 2x^3/l_{el_i}^3 \\ x - 2x^2/l_{el_i} + x^3/l_{el_i}^2 \\ 3x^2/l_{el_i}^2 - 2x^3/l_{el_i}^3 \\ -x^2/l_{el_i} + x^3/l_{el_i}^2 \end{pmatrix} \quad 3-3$$

$$z_i = (u_i, v_i, u_{i+1}, v_{i+1})^T \quad 3-4$$

where, (u_i, v_i) are the displacement and slope of node i , respectively.

The element potential energy can be expressed as

$$PE_i = \frac{1}{2} z_i^T K_i z_i \quad 3-5$$

For a prismatic beam element with Hermite shape functions, the symmetric element stiffness matrix, K_i , can be written as:

$$K_i = \frac{E_i I_i}{l_{el_i}^3} \begin{bmatrix} 12 & 6l_{el_i} & -12 & 6l_{el_i} \\ & 4l_{el_i}^2 & -6l_{el_i} & 2l_{el_i}^2 \\ & & 12 & -6l_{el_i} \\ & & & 4l_{el_i}^2 \end{bmatrix} \quad 3-6$$

The kinetic energy for each element can be calculated as follows:

$$KE_i = \frac{1}{2} \int_0^{l_{el_i}} \rho a \left[\frac{\partial r^T}{\partial t} \cdot \frac{\partial r}{\partial t} \right] dx_i \quad 3-7$$

where, ρ is the beam mass density, a is area of the beam's cross section, and r is the position, as shown in Figure 3.1. Using chain rule ($\frac{\partial r}{\partial t} = \frac{\partial r}{\partial z} \cdot \frac{\partial z}{\partial t}$), Equation (3-7) can be written as:

$$KE_i = \frac{1}{2} \int_0^{l_{el_i}} \rho a \left[\frac{\partial z^T}{\partial t} \cdot \frac{\partial r^T}{\partial z} \cdot \frac{\partial r}{\partial z} \cdot \frac{\partial z}{\partial t} \right] dx_i \quad 3-8$$

The element kinetic energy can be expressed in terms of the element mass matrix, M_i , as follows:

$$KE_i = \frac{1}{2} \dot{z}_i^T M_i \dot{z}_i \quad 3-9$$

Here \dot{z}_i is the speed of the displacement vector, as $\dot{z}_i = \frac{\partial z}{\partial t}$.

Comparing equation (3-8) and Equation (3-9), one can obtain:

$$M_i = \int_0^{l_{el_i}} \rho a \left[\frac{\partial r}{\partial z_i} \right]^T \cdot \frac{\partial r}{\partial z_i} dx_i \quad 3-10$$

In this equation, since $r = \{l_{ac_i} + x, y\}^T$ and $y = \varphi \cdot z_i$, it can be obtained that $\frac{\partial r}{\partial z_i} = \varphi$. This leads to:

$$M_i = \int_0^{l_{el_i}} \rho a \varphi^T \cdot \varphi dx_i \quad 3-11$$

For a beam element with Hermite shape functions, the symmetric element mass matrix, M_i , can be written as:

$$M_i = \frac{\rho a l_{el_i}}{420} \begin{bmatrix} 156 & 22l_{el_i} & 54 & -13l_{el_i} \\ & 4l_{el_i}^2 & 13 & -3l_{el_i}^2 \\ & & 156 & -22l_{el_i} \\ & & & 4l_{el_i}^2 \end{bmatrix} \quad 3-12$$

Since the cantilever beam is fixed at its base, the boundary conditions are:

$$u_1 = 0, v_1 = 0 \quad 3-13$$

The total kinetic and potential energies for the cantilever beam are obtained by the components as follows:

$$KE = \sum KE_i \quad , \quad PE = \sum PE_i \quad 3-14$$

Using Lagrange equation for a conservative system, the equation of motion can be obtained as:

$$\frac{d}{dt} \left[\frac{\partial(KE - PE)}{\partial \dot{q}} \right] - \left[\frac{\partial(KE - PE)}{\partial q} \right] = F \quad 3-15$$

where $\vec{q} = \{u_1, v_1, \dots, u_f, v_f\}$ and \vec{F} is the vector of external forces. The equation of motion can then be written as,

$$[M]\ddot{\vec{q}}(t) + [K]\vec{q} = \vec{F} \quad 3-16$$

where $[M]$, and $[K]$ are mass and stiffness matrices for the cantilever beam. The damping could be added manually as material damping in equation (3-30). Using equation (3-16) one can obtain state-space model of the cantilever beam to control its tip vibration. In the next section the same process is done for a 2L2JM manipulator.

3.2 Finite element model of two-link two-joint manipulator

The 5-DOF manipulator is supposed to suppress the vibration using 2 of its joints. Therefore, modeling a manipulator with 2 joints is necessary. In this regard a two-link two-joint manipulator (2L2JM), as shown in Figure 3-2, with the same specifications as the cantilever beam is proposed (each link has the same dimensions and material as the cantilever). The joints are assumed to have no stiffness and damping. The first joint is assumed as a simply supported condition. This section is based on [31]. According to Figure 3.2, (X, Y) are the global coordinates, $(x_{i,link}, y_{i,link})$ are the local coordinates fixed to element i of the undeformed link where $link = 1, 2$; also, (x_{link}, y_{link}) are the local coordinates of a point on the j th link, $l_{ac,i,j}$ is accumulated length, L_j is the length of j th link, l_{el_i} is the length of i th element for the link, $(u_{i,link}, v_{i,link})$ are displacement and slope of node i of the link, and $(u_{f,link}, v_{f,link})$ are the displacement and slope of the last node of the link, respectively.

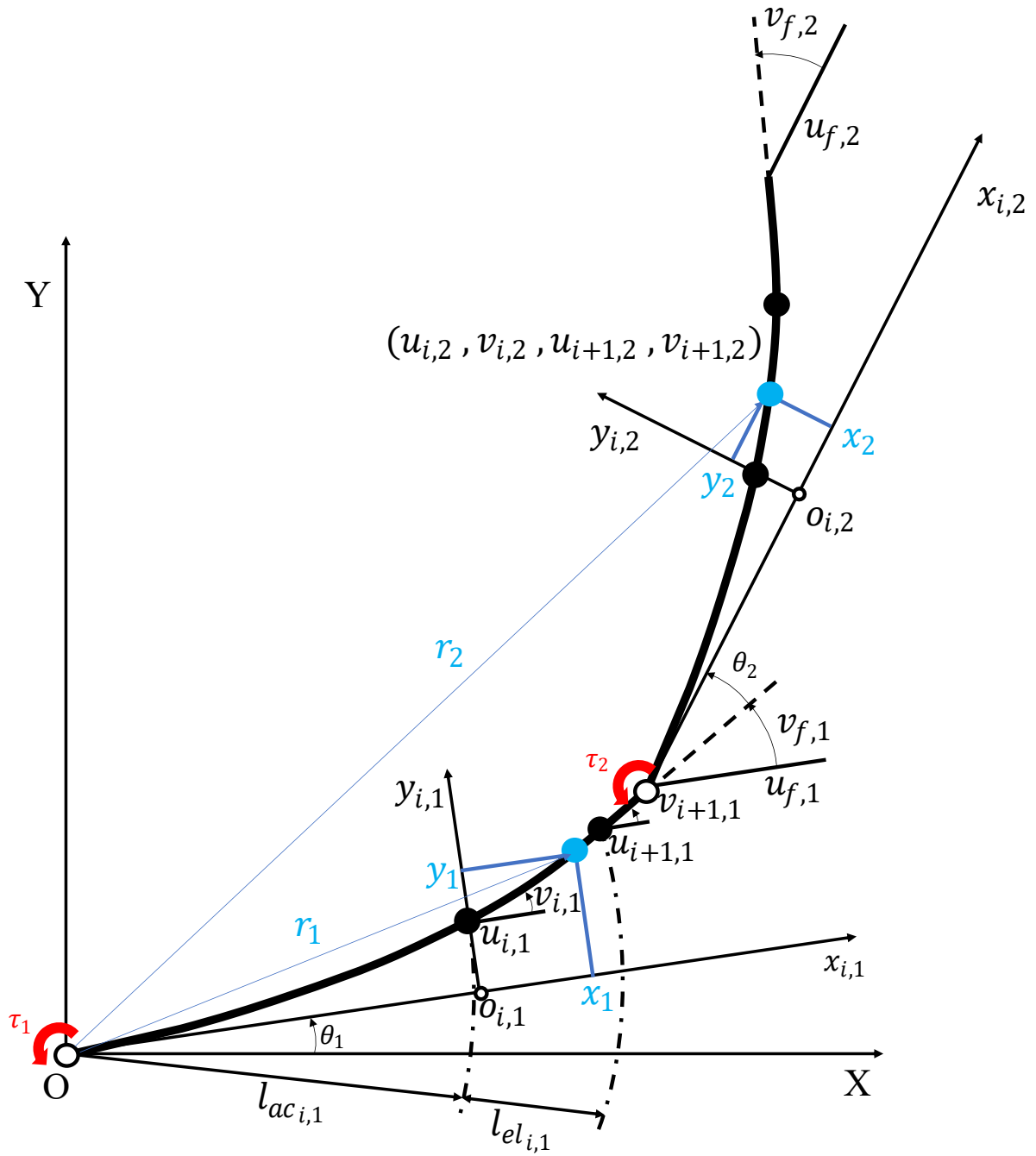


Figure 3.2. Schematic of a two-link two-joint manipulator (2L2JM).

To obtain the location of the point (x_j, y_j) , it is necessary to use transformation matrices as follows:

$$r_1 = \begin{bmatrix} \cos \theta_1 & -\sin \theta_1 \\ \sin \theta_1 & \cos \theta_1 \end{bmatrix} \begin{bmatrix} l_{ac_i,1} + x_1 \\ y_1 \end{bmatrix} \quad 3-17$$

$$r_2 = \begin{bmatrix} \cos \theta_1 & -\sin \theta_1 \\ \sin \theta_1 & \cos \theta_1 \end{bmatrix} \begin{bmatrix} L_1 \\ u_{f,1} \end{bmatrix} + \begin{bmatrix} \cos(\theta_2 + v_{f,2}) & -\sin(\theta_2 + v_{f,2}) \\ \sin(\theta_2 + v_{f,2}) & \cos(\theta_2 + v_{f,2}) \end{bmatrix} \begin{bmatrix} l_{ac_i,1} + x_1 \\ y_1 \end{bmatrix} \quad 3-18$$

The element generalized coordinates are as follows:

$$z_{i,1} = (\theta_1, u_{i,1}, v_{i,1}, u_{i+1,1}, v_{i+1,1})^T \quad 3-19$$

$$z_{i,2} = (\theta_1, u_{f,1}, v_{f,1}, \theta_2, u_{i,2}, v_{i,2}, u_{i+1,2}, v_{i+1,2})^T \quad 3-20$$

In order to meet $y_j = \varphi_j z_{i,j}$, using the equation (3-3), the links' shape functions would be as follows:

$$\varphi_1 = \begin{bmatrix} 0 \\ \varphi \end{bmatrix}, \quad \varphi_2 = \begin{bmatrix} 0_{4 \times 1} \\ \varphi \end{bmatrix} \quad 3-21$$

The mass and stiffness matrices are obtained using the same equations as 3-5 to 3-10. However, due to θ_1, θ_2 , one cannot conclude equation (3-11). Using equation (3-6), element stiffness matrices would be:

$$K_{i,1} = \begin{bmatrix} 0 & 0 \\ 0 & K_i \end{bmatrix}, \quad K_{i,2} = \begin{bmatrix} 0_{4 \times 4} & 0 \\ 0 & K_i \end{bmatrix} \quad 3-22$$

where K_i is the element stiffness matrix in equation (3-6). The mass matrices are obtained as follows:

$$M_{i,link} = \int_0^{l_{el_i,link}} \rho a \left[\frac{\partial r}{\partial z_{i,link}} \right]^T \cdot \frac{\partial r}{\partial z_{i,link}} dx_{i,link}$$

The boundary conditions are:

$$u_{1,1} = 0, v_{1,1} = 0, \quad u_{1,2} = 0, v_{1,2} = 0 \quad 3-23$$

Similar to the previous section the equation of motion (3-16) is derived.

A program based on this section was given in Appendix G for the 2L2JM. Moreover, the same approach could have been used to find a simplified geometry of the 5-DOF manipulator called parallelogram (the approach was coded in Appendix H) [32]. However, the main objective of this thesis was modeling the 5-DOF manipulator and not a parallelogram. Besides, the manual FEM was not feasible for the 5-DOF manipulator since it has a complex structure. Therefore, any state-space model of the 5-DOF manipulator in the following chapters is just based on the eigenvectors extracted from FEA-A.

3.3 State-space modeling using principal coordinates

When exerting force on an n-degrees-of-freedom (n-DOF) system, it undergoes forced vibration. The governing equation of motion is n coupled 2nd order ODE as follows:

$$[M]\ddot{\vec{q}} + [K]\vec{q} = \vec{F} \quad 3-24$$

Proportional damping may be added to this equation [28]. It is easier to uncouple this system of differential equations using modal analysis. For this purpose, the eigenvalue problem can be solved:

$$\omega^2[M]\vec{Z} = [K]\vec{Z} \quad 3-25$$

which results in the natural frequencies $\{\omega\} = \omega_1, \omega_2, \dots, \omega_n$ and its normal modes $\vec{Z}^{(1)}, \vec{Z}^{(2)}, \dots, \vec{Z}^{(n)}$. The matrix of normal modes, the modal matrix, can be written as:

$$[Z]_{modal} = [\vec{Z}^{(1)}, \vec{Z}^{(2)}, \dots, \vec{Z}^{(n)}] \quad 3-26$$

Modal analysis is based on the expansion theorem that the physical coordinates are linear combination of normal modes [28]:

$$\vec{q}(t) = z_{p1}(t)\vec{Z}^{(1)} + z_{p2}(t)\vec{Z}^{(2)} + \dots + z_{pn}(t)\vec{Z}^{(n)} \quad 3-27$$

where $z_{p1}(t), z_{p2}(t), \dots, z_{pn}(t)$ are the principal coordinates. Equation (3-27) is also called the mode superposition principle. For simplicity, equation (3-27) in the vector form is as follows:

$$\vec{q}(t) = [Z]_{modal} \vec{Z}_p(t) \quad 3-28$$

where $\vec{Z}_p(t) = \{z_{p1}(t), z_{p2}(t), \dots, z_{pn}(t)\}$ is the vector of principal coordinates. By substituting equation (3-28) in equation (3-24) one can obtain:

$$[Z]_{modal}^T [M] [Z]_{modal} \ddot{\vec{Z}}_p(t) + [Z]_{modal}^T [C] [Z]_{modal} \dot{\vec{Z}}_p + [Z]_{modal}^T [K] [Z]_{modal} \vec{Z}_p = [Z]_{modal}^T \vec{F} \quad 3-29$$

If the modal matrix is normalized with respect to mass such that $[Z]_{modal}^T [M] [Z]_{modal} = I$, then the system of equation (3-29) becomes n-uncoupled 2nd order ordinary differential equations (ODEs):

$$\ddot{\vec{Z}}_p(t) + 2\{\zeta\}\{\omega\}\dot{\vec{Z}}_p(t) + \{\omega\}^2 \vec{Z}_p(t) = F_p \quad 3-30$$

where F_p is the vector of principal forces, and $\{\zeta\}$ is the vector of material damping which could be considered from [33].

Using modal analysis in FEA-A, the natural frequencies and normalized modal matrix of a geometry could be obtained. The rows and columns of the matrix correspond to the specified DOFs of the geometry and vibrational modes, respectively.

where h is the number of nodes that input forces are exerted on. The output matrix is:

$$C_{g \times 2n} = \begin{bmatrix} \hat{z}_{11} & 0 & \hat{z}_{12} & 0 & \dots & \hat{z}_{1n} & 0 \\ \hat{z}_{21} & 0 & \hat{z}_{22} & 0 & \dots & \hat{z}_{2n} & 0 \\ \vdots & \vdots & \vdots & \vdots & \vdots & \vdots & \vdots \\ \hat{z}_{g1} & 0 & z_{g2} & 0 & \dots & z_{gn} & 0 \end{bmatrix} \quad 3-35$$

where g is the number of generalized coordinates as outputs. For the most systems such as in this thesis, the feedthrough matrix is zero.

Based on the obtained model of the system in (3-32), one cannot distinguish the contribution of the states to the past input and future output energy of the system. To identify this contribution, balancing should be applied on the model[34].

3.4 Balanced realization and model reduction

Dealing with a large order state-space system leads to an inefficient online control system; thus, to obtain low latency and higher control bandwidth, model reduction is necessary [35]. To reduce the model of the system, balanced realization is proposed. Balancing arranges the model based on the contribution of the states to I/O. This method is based on controllability and observability Gramians which identify the amount of controllability and observability of the states. Controllability and observability Gramians are defined as $W_c(t)$, and $W_o(t)$, respectively [35]:

$$W_c(t) = \int_0^t e^{A\tau} B B^T e^{A^T \tau} d\tau \quad 3-36$$

$$W_o(t) = \int_0^t e^{A^T \tau} C^T C e^{A\tau} d\tau \quad 3-37$$

where A , B , and C are the state-space matrices.

For an infinite time, the Gramians would be referred to as W_c , and W_o . The Gramians are n by n matrices. If the eigenvalue problem is solved for the controllability Gramian:

$$(W_c(t))\alpha = \lambda\alpha \quad 3-38$$

and the eigenvalues are sorted from the biggest to the smallest, then the eigenvector corresponding to the biggest eigenvalue would be the most controllable direction in the state-space coordinate. A more controllable direction means that, given an initial condition, reaching a certain state of the system requires less amount of input energy than the other state. Similarly, observability could be sorted to show the most observable direction. A more observable direction means that, given a measurement output, a certain state of the system is estimated in a manner that is less noisy than the other state.

There is a special coordinate transformation T that makes both Gramians equal and diagonal. If $X = T\tilde{X}$ and is substituted in equation (3-32), the transformed state-space system would be:

$$\begin{cases} \dot{\tilde{X}} = T^{-1}AT\tilde{X} + T^{-1}BU \\ Y = CT\tilde{X} + DU \end{cases} \quad 3-39$$

where \tilde{X} is the state vector in an order so that both observability and controllability Gramians are equal and diagonal.

In a simpler notation one can rewrite the following equations:

$$\begin{cases} \dot{\tilde{X}} = \tilde{A}\tilde{X} + \tilde{B}U \\ Y = \tilde{C}\tilde{X} + DU \end{cases} \quad 3-40$$

Then, the Gramians would become as follows:

$$\tilde{W}_c = T^{-1}W_c(T^T)^{-1} \quad 3-41$$

$$\tilde{W}_o = T^T W_o T \quad 3-42$$

By multiplying Gramians:

$$\tilde{W}_c \tilde{W}_o = T^{-1} W_c W_o T \quad 3-43$$

and assuming $\tilde{W}_c = \tilde{W}_o = \Sigma$, then, the equation (3-43) becomes an eigenvalue problem:

$$W_c W_o T = T \Sigma^2 \quad 3-44$$

Solving equation (3-44) will result in the transformation T and the values Σ that represent the equal and diagonal controllability and observability Gramians.

After sorting T based on the biggest to lowest values of Σ , one could truncate the transformed system, to keep the modes with significant contribution to the past input and future output energy of the system. By partitioning the full state vector \tilde{X} to $[\tilde{X}_1, \tilde{X}_2]^T$, where \tilde{X}_1 and \tilde{X}_2 are the state variables to keep and to remove, respectively. Then, equation (3-40) becomes the following system:

$$\begin{cases} \begin{bmatrix} \dot{\tilde{X}}_1 \\ \dot{\tilde{X}}_2 \end{bmatrix} = \begin{bmatrix} \tilde{A}_{11} & \tilde{A}_{12} \\ \tilde{A}_{21} & \tilde{A}_{22} \end{bmatrix} \begin{bmatrix} \tilde{X}_1 \\ \tilde{X}_2 \end{bmatrix} + \begin{bmatrix} \tilde{B}_1 \\ \tilde{B}_2 \end{bmatrix} U \\ Y = [\tilde{C}_1 \quad \tilde{C}_2] \begin{bmatrix} \tilde{X}_1 \\ \tilde{X}_2 \end{bmatrix} \end{cases} \quad 3-45$$

In order to eliminate the fast dynamics or high frequency modes, we need to set $\dot{\tilde{X}}_2 = 0$. This reduction is called Match-DC-gain model reduction algorithm or MDC [36]. Then, the equation (3-45) turns to the reduced system as follows:

$$\begin{cases} \dot{\tilde{X}}_1 = [\tilde{A}_{11} - \tilde{A}_{12} \tilde{A}_{22}^{-1} \tilde{A}_{21}] \tilde{X}_1 + [\tilde{B}_1 - \tilde{A}_{12} \tilde{A}_{22}^{-1} \tilde{B}_2] U \\ Y = [\tilde{C}_1 - \tilde{C}_2 \tilde{A}_{22}^{-1} \tilde{A}_{21}] \tilde{X}_1 + [D - \tilde{C}_2 \tilde{A}_{22}^{-1} \tilde{B}_2] U \end{cases} \quad 3-46$$

The system of equation (3-46) is the reduced state-space representation of the system. This system contains the states that have significant contribution to the past input and future output energy of the system. Thus, it has less computational cost for the controller. For more information about Gramians and balanced realization refer to[37].

After the state-space model of the system was obtained. The model was balanced and reduced using the M-software commands; “balreal” and “modred”, respectively.

3.5 Modal FEA-A for the manipulators studied

The modal FEA-A results including the natural frequencies and mode shapes were used for modeling and vibration control of the manipulators. The mode shapes were given in Appendixes B, C and D. First, the CAD models of the manipulators were modeled in SolidWorks. Then modal analyses were done on these geometries by FEA-A. For the 5-DOF manipulator, the analysis assumed a free base and free rotation for the 2nd, and the 3rd joints of the manipulator. The analyses parameters were as follows:

1. The material for the cantilever beam, 2L2JM and the 5-DOF except its upper arm was structural steel. The upper arm and the EE for the 5-DOF manipulator were an Aluminum Alloy as stated in Table 2.1.
2. The mesh for the manipulators were generated automatically by the software; however, the number of elements for the cantilever beam and the 2L2JM were tested with different number of elements in section 3.6. The comparison on the natural frequencies showed the automatic mesh has achieved the convergence. For the 5-DOF manipulator the smaller element size was not achievable by the software as the number of the elements would have exceeded and the license did not perform the simulation. Therefore, for the 5-DOF manipulator the generated mesh by the software was used. The mesh details for the manipulators were as follows:

The 5-DOF manipulator mesh was shown in Figure 3.3. The mesh method and sizing were automatically chosen by the software; however, a refinement was defined on the thin link. The properties are extracted from modal solution information. The contact between the parts is CONTA174 which is a 3-D 8-Node Surface-to-Surface Contact. Moreover, the

joints are revolute MPC184 that are set to have zero stiffness and damping. The body elements are SOLID186, and Solid 187 which are 3-D 20-Node Structural Solid, and 3-D 10-Node Tetrahedral Structural Solid, respectively. Moreover, TARGE170 is used to define the boundary of a deformable body associated with contact elements. Mesh statistics are as follows:

Number of total nodes = 179974

Number of solid elements = 60366 (SOLID186, and SOLID 187)

Number of total elements = 145388 (including contacts and solid elements)

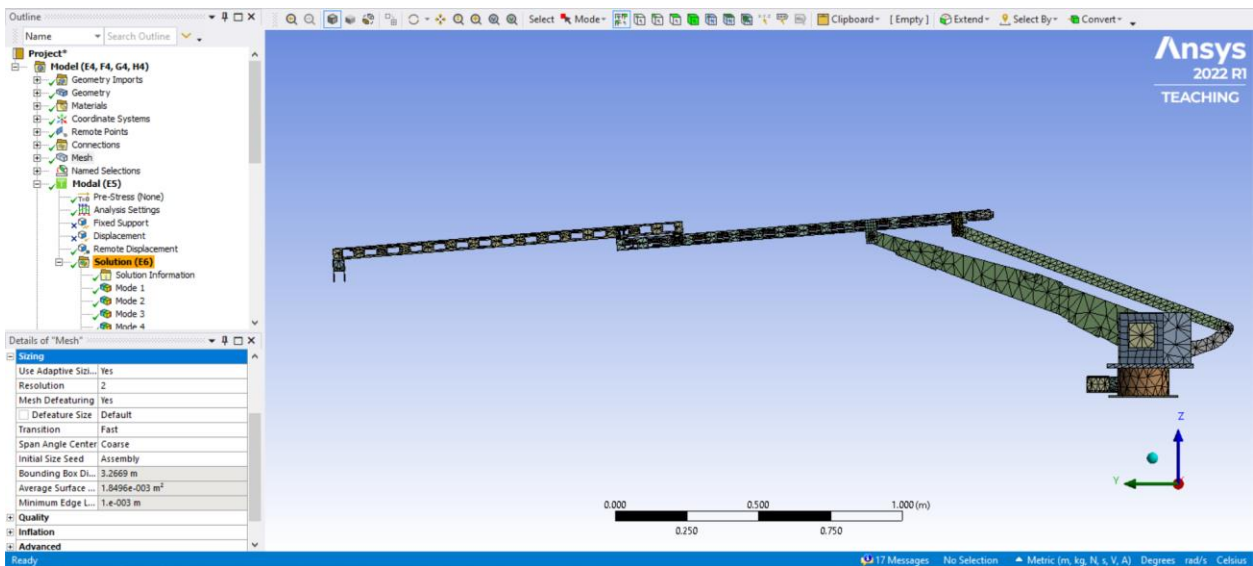


Figure 3.3. The 5-DOF manipulator mesh results in FEA-A workbench.

The Cantilever beam was meshed in FEA-A workbench, as shown in Figure 3.4. The properties were extracted from the modal solution information. The cantilever is a line body. The body elements are Beam188 which is a 3-D 2-Node Beam.

--- Number of total nodes = 86

--- Number of solid elements = 42 (Beam188)

--- Number of total elements = 42

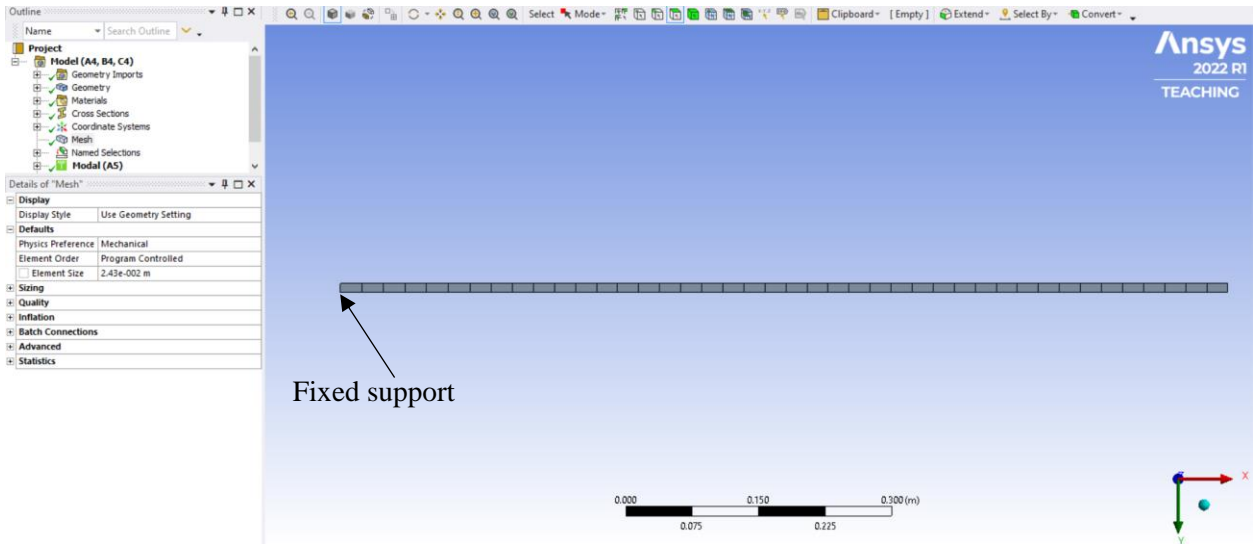


Figure 3.4. The Cantilever beam mesh results in FEA-A workbench.

The 2L2JM was meshed in FEA-A workbench, as shown in Figure 3.5. The properties were extracted from the modal solution information. The 2L2JM is a line body. The body elements were BEAM188 which was a 3-D 2-Node Beam. The first joint was CONTA175 which was a 2-D/3-D Node-to-Surface Contact element. The joint in the middle of the links was a revolute MPC184 with zero stiffness and damping. Moreover, TARGE170 was used to define the boundary of a deformable body associated with contact elements.

--- Number of total nodes = 154

--- Number of solid elements = 74 (37 BEAM188 for each link)

--- Number of total elements = 81

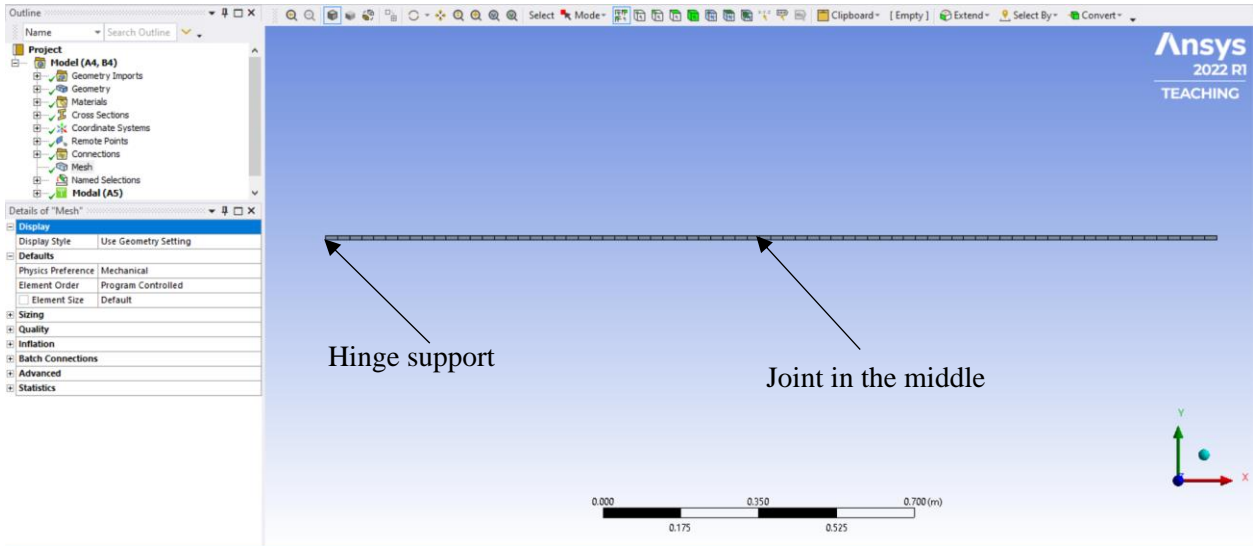


Figure 3.5. The 2L2JM mesh results in FEA-A workbench.

3. The boundary condition for the manipulators are as follows:

For the 5-DOF manipulator, remote displacement was defined such that it let the base only move in vertical direction. For the cantilever beam it was a fixed support at its end. For the 2L2JM it was simple support at one end of the manipulator. It was noteworthy that both cantilever beam and the 2L2JM were restricted to move in x-y plane.

3.6 Verification of finite element models

In this section manual FEM model was used to verify FEA-A results. First, using the mass and stiffness matrices in sections (3.1, 3.2), natural frequencies were obtained and compared with those of FEA-A. After that, the master nodes of manipulators were chosen. Then, given the verified results of FEA-A, the eigenvectors were used to make the state-space models in sections (3.3, 3.4). Finally, the responses of the state-space models were compared with transient module of FEA-A.

The FE results of the cantilever beam and 2L2JM are given in Table 3.2 and Table 3.3, respectively. The manual FEM and FEA-A modal analysis results are compared using a different number of elements. Each row of these tables corresponds to a vibrational mode of the corresponding manipulator. To compare the convergence of the meshing, a change index is defined

as $|\omega_n^{6\text{ Ele}} - \omega_n^{9\text{ Ele}}| / (\omega_n^{9\text{ Ele}})$. Here the index specifies the difference between the natural frequencies of 6 and 9 elements. This change value for the cantilever was calculated for the 6th mode of vibration, whereas that of the 2L2JM was for the 8th mode. The convergence for the manual FEM was considered as being less than a 2% change, whereas that of FEA-A was less than a 0.1% change.

It is noteworthy that in Table 3.3, there were 2 rigid modes with zero natural frequencies since 2L2JM had joints with no stiffness.

Table 3.2. Cantilever beam, natural frequencies for manual FEM and FEA-A for different number of elements.

mode	Natural Frequencies (Hz), manual FEM				Natural Frequencies (Hz), FEA-A			
	3 Ele	4 Ele	6 Ele	9 Ele	3 Ele	9 Ele	42 Ele	100 Ele
1	8.153	8.152	8.152	8.152	8.155	8.153	8.153	8.153
2	51.25	51.14	51.10	51.09	51.66	51.07	51.07	51.07
3	144.8	144.1	143.3	143.1	156.0	143.0	142.9	142.9
4	326.1	284.3	282.1	280.7	251.5	280.9	279.7	279.7
5	613.8	528.9	470.3	465.1	339.3	467.0	461.7	461.7
6	1223.	849.5	703.7	697.7	454.0	705.4	688.5	688.4
% Change	75.29	21.75	0.860	-	34.05	2.470	0.015	-

According to Table 3.2, the 6th mode for the manual FEM of the cantilever beam with 6 and 9 elements per link had 0.86% change, which proved the convergence of the manual FEM for this geometry. On the other hand, the 6th mode for the FEA-A of the cantilever beam with 42 and 100 elements had 0.01% change, which proved the convergence of the FEA-A for this geometry. Given the 6th mode for the manual FEM with 6 elements, the natural frequency of the 6th mode for the FEA-A with 42 elements per link had $(703.7-688.5) / 703.7 = 2.16\%$ error. Therefore, the FEA-A results were verified. Moreover, the FEA-A eigenvectors of the manipulator with 42 elements were chosen for state-space modeling. The eigenvectors extracted from FEA-A are normalized with respect to mass which is required in section 3.3.

Table 3.3. The 2L2JM, natural frequencies for manual FEM and FEA-A for different number of elements.

mode	Frequencies (Hz), manual FEM			Frequencies (Hz), FEA-A			
	3 Ele/link	6 Ele/link	10 Ele/link	3 Ele/link	10 Ele/link	37 Ele/link	100 Ele/link
1	0	0	0	0	0	0	1.100e-3
2	0	0	0	0	0	0	1.203e-3
3	16.97	21.58	23.62	26.78	26.69	26.69	26.69
4	48.93	47.88	47.32	46.60	46.18	46.18	46.18
5	98.28	114.0	109.0	103.1	99.31	99.28	99.28
6	123.5	120.6	127.6	142.7	133.6	133.5	133.5
7	154.8	172.9	189.7	228.2	217.6	217.2	217.2
8	311.7	275.5	272.5	243.9	267.3	266.6	266.7
% Change	14.39	1.101	-	8.549	0.225	0.038	-

According to Table 3.3, the 8th mode for the manual FEM of the 2L2JM with 6 and 10 elements had 1.10% change, which proved the convergence of the manual FEM for this geometry. On the other hand, the 8th mode for the FEA-A of the cantilever beam with 37 and 100 elements had 0.038% change, which proved the convergence of the FEA-A for this geometry. Given the 8th mode for the manual FEM with 6 elements, the natural frequency of the 6th mode for the FEA-A with 37 elements had $(275.5-266.6) / 275.5 = 3.23\%$ error. Therefore, the FEA-A results were verified. Moreover, the eigenvectors of the FEA-A with 37 elements per link were chosen for state-space modeling.

3.7 State-space modeling for the manipulators

After verifying the modal results of FEA-A, the eigenvectors of the meshed geometries were used to make the state-space models of the manipulators. First, an APDL program was made to take only the relative displacement of the specified master nodes for the first n modes. These

programs for the manipulators were given in Appendix I. Second, the master DOFs were extracted from one of the 6 displacements (ux, uy, uz, rotx, roty, rotz) of the master node for all the first n modes. One sample of this extraction is shown in Figure 3.6 which corresponds to the 4th mode of the 5-DOF manipulator. Third, the extracted master DOFs for the first n modes were placed in a matrix to build the modal matrix. This table for the manipulators is given in Appendix J. Finally, a M-software program was coded to create the state-space models from the modal matrices. The resulting state-space matrices for the 5-DOF manipulator were given in Appendix K.

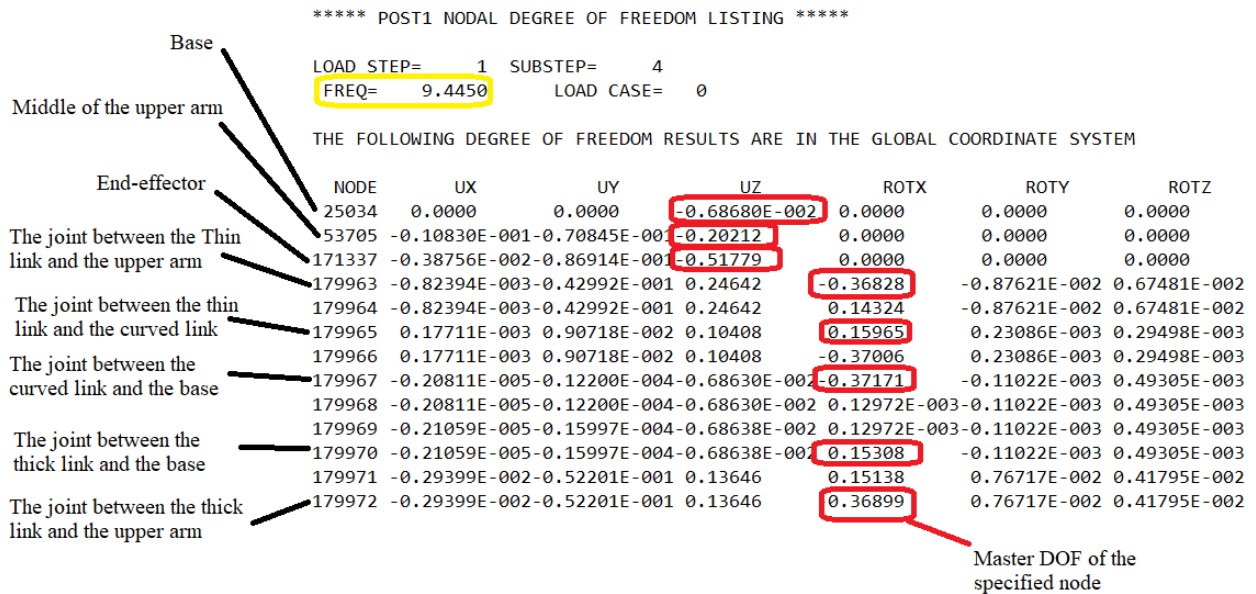


Figure 3.6. Master DOF extraction for the 4th mode of the 5-DOF manipulator.

For dynamic problems, master DOFs are typically chosen as displacements of the nodes with higher mass and rotations of the nodes with higher mass moment of inertia. On the other hand, the slave degrees of freedom are the displacements and rotations of the relatively lower inertia nodes [26]. According to equation (3-31), the rows of the matrix correspond to one generalized coordinate of the master nodes. These nodes are chosen from geometry after that the mesh is done. These nodes contain the main dynamic characteristic of the system so that the relative displacement of these nodes would be sufficient to show the dynamic behavior of the system. The input and output of the system are the necessary master nodes; however, other nodes could also be chosen for more accurate modeling. More information about the mesh properties of the manipulators is

provided in appendixes B, C, and D. The master DOFs of the manipulators are shown in Figure 3.7.

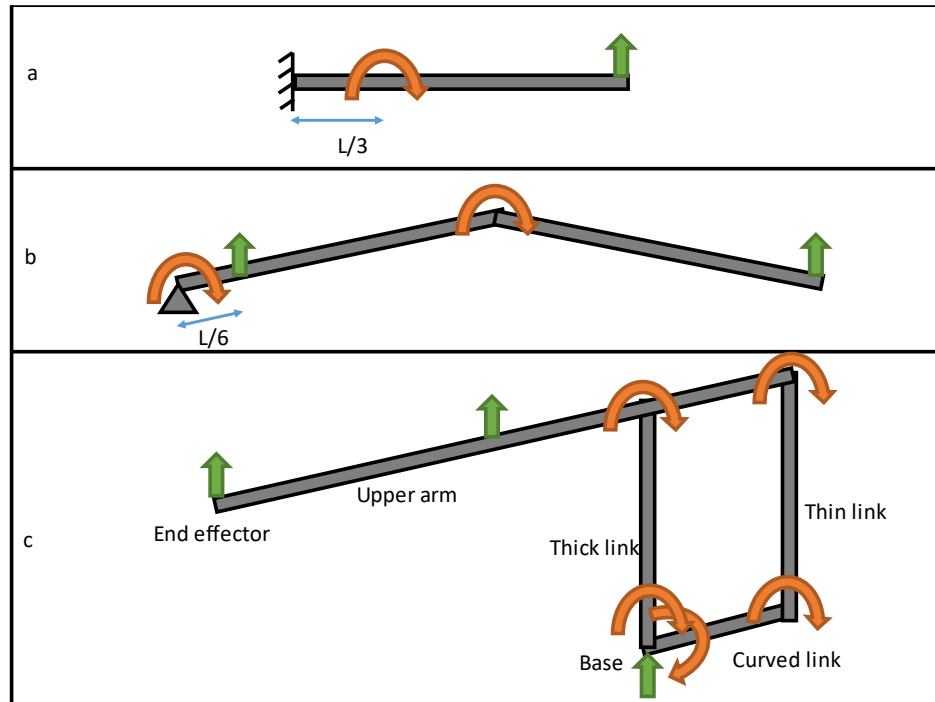


Figure 3.7. Master DOFs of the manipulators. The vertical displacements are represented with green arrows, while the rotational displacements are shown by orange curved arrows. (a) Master DOFs of the cantilever beam. (b) Master DOFs of the 2L2JM. (c) Master DOFs of the 5-DOF manipulator.

According to Figure 3.7, For the cantilever beam, the eigenvectors include the relative displacements of 2 master DOFs, the linear displacement of the tip and rotational displacement of a point located at $L/6$, where the actuator is located. This location is for the actuator and disturbance needs to be far from the vibrational nodes of the first n modes. Looking at appendix C, one could observe that for vibration suppression of the first 6 modes, a location between $[0, L/5]$ was proper to place the actuator.

For the 2L2JM, the eigenvectors include the relative displacements of 4 master DOFs: the linear displacement of the tip and the actuator, plus the rotational displacement of the joints. In Chapter 4, these joints act as the actuators for vibration suppression. Unlike the cantilever beam for which the disturbance and the vibration suppression actuators were at the same point, for 2L2JM, it was

assumed that there was a nodal force on the point at $L/3$ of the first link to produce a linear force as a disturbance. This configuration leads to MIMO controller in Chapter 4.

For the 5-DOF manipulator, 8 generalized coordinates are used as the master DOFs. According to Figure 1.1 and Figure 3.7, the vertical displacement of the EE, base, and middle of the upper arm as well as rotational displacement of 5 joints. These joints are: 1. the joint between the base and the curved link; 2. the joint between the curved link and thin link; 3. the joint between the thick link and the base; 4. the joint between the thin link and the upper arm; 5. the joint between the thick link and the upper arm. The reason for choosing the middle of the upper arm as one of the locations for master DOF was due the overlap of the prismatic joint which was twice as heavy as other parts of the upper arm.

3.8 Transient analysis methodology

After obtaining the state-space models of the manipulators, transient responses of the manipulators were simulated in M-software using “lsim” command. This command, first, discretizes the state-space model based on the applied input. If the input is discontinuous (not-smooth) such as in sections 3.11, and 4.2, the discretization is based on zero-order-hold. whereas, for the smooth input simulations, such as all the simulations in Chapter 3 and 4, except sections 3.11 and 4.2, the discretization method is first-order-hold [38]. After discretization, “lsim” propagates the discrete-time state-space equations. The propagation means solving the equation from the initial condition at $p = 1$ to the final iteration as follows:

$$\begin{cases} X[p + 1] = AX[p] + BU[p] \\ Y[p] = CX[p] \end{cases} \quad 3-47$$

where p is the number of iterations. The time step for “lsim” is based on the time step for the applied input. For simplicity on impulse simulation in section 4.2, the “impulse” command was used which is like “lsim”. Similarly, it discretizes the state-space model based on zero-order-hold. Then, the propagation is solved based on the unforced system with initial condition as follows:

$$\begin{cases} X[p + 1] = AX[p] \\ Y[p] = CX[p] \end{cases}, \quad X[1] = B \quad 3-48$$

The time-step for “impulse” is automatically chosen based on the dynamics of the system.

The excitation had an arbitrary pattern to distinguish different models. In addition to these state-space models, an FEA-A transient response was simulated. For this purpose, the FEA-A modal results presented in section 3.5 were connected to transient module of FEA-A. Then the same initial condition and excitation as for the state-space models was applied to this module. The “FEA-A transient” plot in the following figures indicate the mentioned response by FEA-A.

For the cantilever beam, the eigenvectors of the FEA-A manipulator with 42 elements were chosen for state-space modeling. Then among all DOFs, two generalized coordinates were specified as the master DOFs (vertical displacement of a point at $L/3$ and the tip). The state-space matrices for the cantilever beam are given in Appendix K. The full state-space model includes all the 20 eigenvectors of the cantilever beam extracted from FEA-A (20 modes was chosen to be extracted). Then they were processed using section 3.3. The Truncated¹ model includes the first 2 modes of vibration, *i.e.*, it has the first 4 columns and the first 4 rows of the full order state-space model. Finally, the BMDC stands for the balanced realization of the full order model which is followed by reduction to 2 modes using section 3.4.

For 2L2JM, the eigenvectors of the FEA-A manipulator with 37 elements (links) were chosen for state-space modeling. Then among all the DOFs, 4 generalized coordinates were specified as the master DOFs. The state-space matrices for the cantilever beam are given in Appendix L. The full state-space model includes all 20 eigenvectors of the manipulator extracted from FEA-A. Then they were processed using section 3.3. The Truncated model includes the first 4 modes of vibration, *i.e.*, it had the first 8 columns and first 8 rows of the full state-space model. However, for the BMDC model, first, the full order model without the rigid modes was balanced, then the balanced-oscillatory model was reduced to keep only 2 modes. Finally, the 2 rigid modes were attached to result in the model with 4 modes. The pictures for the rigid modes are shown in Appendix D.

The 5-DOF manipulator for the modeling and control was assumed to be free from the ground (only free in vertical direction) which resulted in the first rigid body mode. That base is where the disturbance/excitation is exerted to the manipulator. Also, the 2nd and the 3rd joints were not fixed,

¹ Throughout this thesis, Truncated model refers to the model reduction without balancing.

and they had no stiffness and damping. These joints were the actuators that control the excitation. Because of the 2 revolute joints, the manipulator had 2 more rigid body modes. Thus, the modes 1,2, and 4 were the rigid modes (Appendix B). Among all DOFs, 8 generalized coordinates were specified as the master DOFs. The full state-space model includes all 30 eigenvectors of the manipulator extracted from modal module of FEA-A. Then they were processed using section 3.3. The Truncated model includes the first 5 modes of vibration, *i.e.*, it has the first 10 columns and first 10 rows of the full state-space model. However, for the BMDC model, first, the full order model without the rigid modes was balanced, then the balanced-oscillatory model was reduced to keep only 2 modes. Finally, the 3 rigid modes were attached to result in the model with 5 modes. The pictures for the rigid modes are shown in Appendix B.

Regarding the material damping for the simulations including sections 3.9, 3.10, 3.11, 4.4, and 4.5, material damping was set to the almost zero value of $5e-5$. The reason for having almost no damping for these simulations was to perform simulations for the worst-case scenario. In other words, simulations in Chapter 3 would show the vibrational behavior of models better if there was no damping. Besides, the controllers' performance in Chapter 4 show the ability of controllers to suppress the vibration without help from passive dampers. A small value for material damping was used to avoid instability for H-infinity controller in sections 4.4, and 4.5.

For section 4.2, the cantilever beam was a SISO problem which was under impact. It was decided to consider a damping ratio of $\zeta = 0.02$ according to [33], to show that the model reduction did not affect the response of the system compared with the full order model.

3.9 Results, cantilever beam model

This section is devoted to different state-space models of the cantilever beam. The responses of the models to an arbitrary vibration applied on the actuator were depicted. In addition, the models were verified in the presence of the transient module of FEA-A with the same condition. Then, the Gramians of balanced and unbalanced systems were discussed. The time step for the state-space simulations in this section was $5e-4s$ for the entire duration, whereas that of the FEA-A was $5e-3s$.

Plot a and b in Figure 3.8 shows three different state-space models of the cantilever beam that are compared with the transient module of FEA-A under an arbitrary vibration excitation. Plot c,

shows the excitation that was applied to the $L/6$ of the beam. The excitation was an arbitrary moment in the duration of 0.5s.

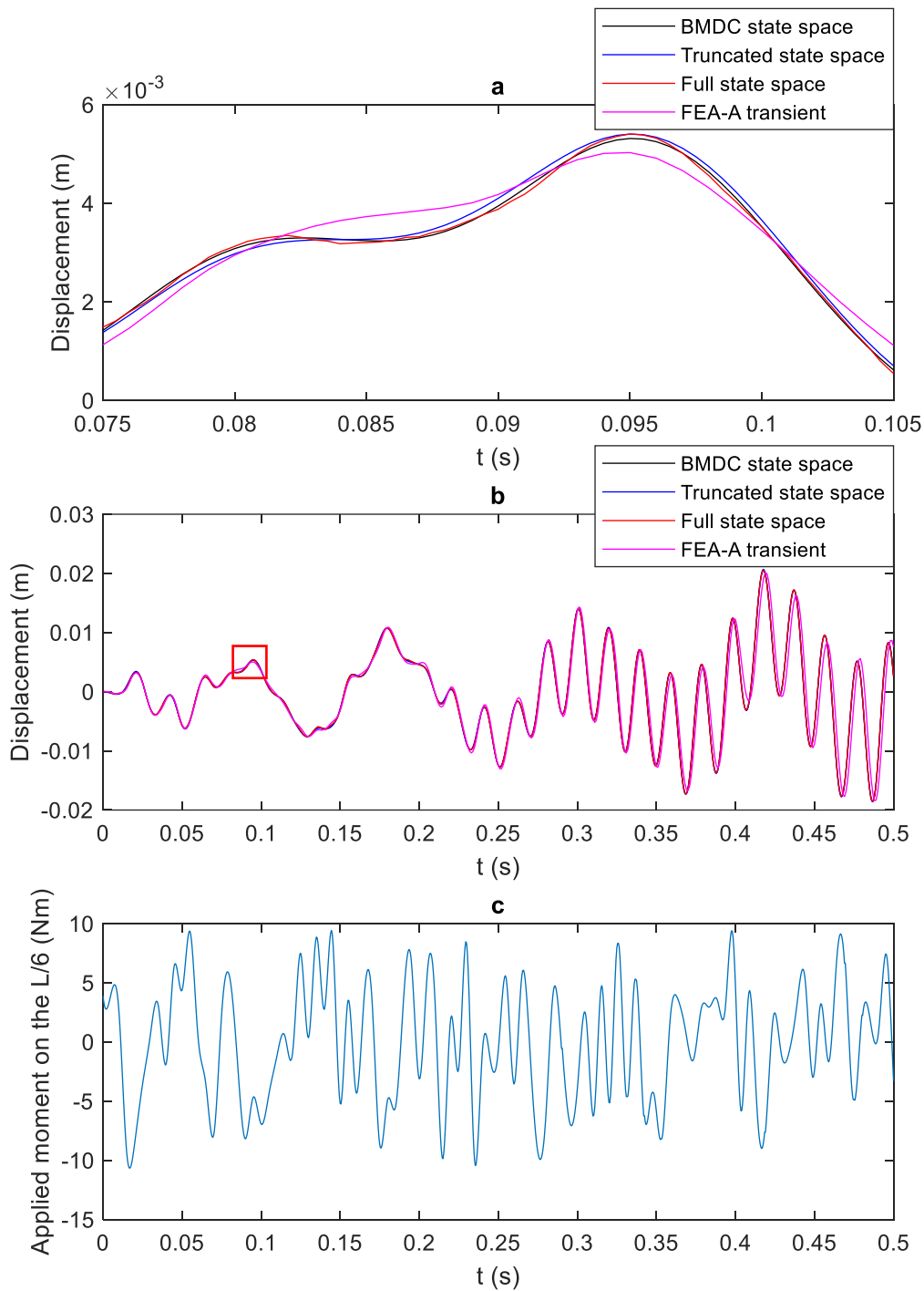


Figure 3.8. Cantilever beam's tip displacement and moment for 3 different state-space models as well as FEA-A transient. a- the response for small time duration, for comparison, b- the response for 0.5 second interval, c- an arbitrary excitation moment between $[-10,10]$ N-m applied on $L/6$ of the beam.

As shown in Figure 3.8, the red and magenta plot on top of each other. It proves that the full order mathematical model with state matrix of 40 by 40 is almost the same as the FEA-A. This indicates the accuracy of the full order model with only 2 master DOFs and 20 modes. More importantly, the black line which is for the BMDC model with state matrix of 4 by 4 is similar to the FEA-A results. This indicates the accuracy and efficiency of the BMDC with only 2 master DOFs and 2 modes. Since the cantilever is a relatively simple geometry, the BMDC and Truncated models give the same result.

The difference index of the models was represented by the normalized RMS values in Table 3.4. the RMS is defined as follows:

$$RMS = \sqrt{\frac{1}{N} \sum_{n=1}^N |variable_n|^2} \quad 3-49$$

where *variable* is the difference of the tip displacement from any of the state-space models with that of the FEA-A transient (reference model). *n* and *N* are the *n*th variable and the total number of variables, respectively. Then the RMS values were normalized with respect to the maximum value, which was obtained from the worst model.

Table 3.4. Normalized RMS values of different models and their comparison with FEA-A transient for the cantilever beam.

	Full order	BMDC	Truncated
Normalized RMS	1	0.9960	0.9966

According to Table 3.4, the normalized RMS values did not show any significant difference between the state-space models and the FEA-A transient; *i.e.*, they did not have any significant difference. This was due to the fact that the cantilever beam was a relatively simple geometry.

As discussed in section 3.4, the balanced realization deals with Gramians. After developing state matrices, A, B, C, and D, one could use the “gram” command in M-software to find the observability and controllability Gramians which are *n* by *n* matrices. This command is based on equations 3-36 and 3-37. According to [39], for the systems with a small damping coefficient, and

described in modal coordinates, the diagonal elements of the Gramian matrices are dominant. Thus, the diagonal elements of the controllability or observability Gramian give information about the relative controllability or observability of the different modes, respectively. To show these diagonal elements of the observability or controllability Gramian, “meshz” was used. The result is shown in Figure 3.9 and Figure 3.10. Similarly for the 2L2JM these results were given in Figure 3.12 and Figure 3.13, and for the 5-DOF manipulator in Figure 3.15 and Figure 3.16.

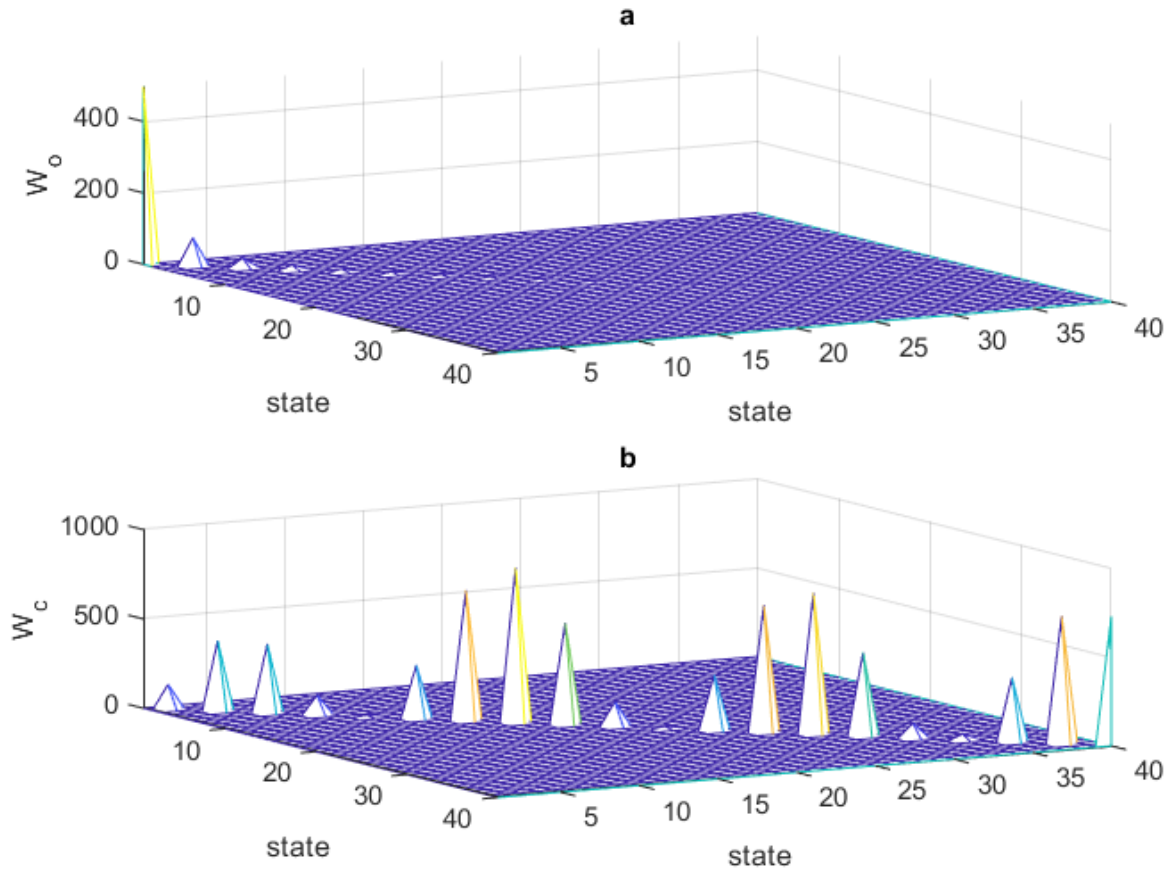


Figure 3.9. Cantilever beam, full order model, a. Observability Gramian and b. Controllability Gramian.

According to Figure 3.9, the Gramians of the 40 states of the 20 modes from the full order model were scattered in the plane of the states. It was noted that model reduction before balancing could remove the states with higher priority in terms of observability or controllability. Therefore, balancing was recommended for model reduction.

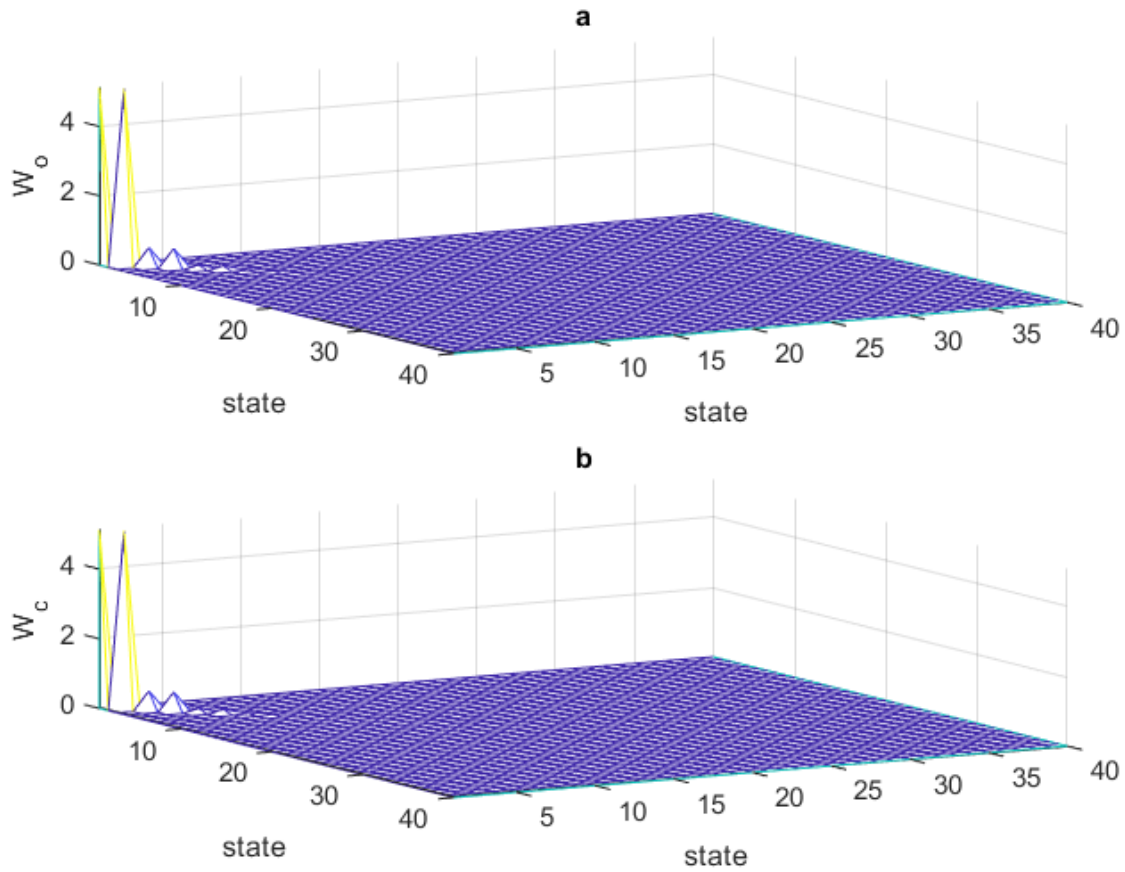


Figure 3.10. Cantilever beam, balanced full order model, a. Observability Gramian and b. Controllability Gramian.

As shown in Figure 3.10, the balanced algorithm made both Gramians equal and sorted. Then model reduction would consider modes' priorities. It is obvious that the first 2 modes or 4 states would give almost entire dynamic behavior of the system.

3.10 Results, two-link two-joint manipulator (2L2JM)

In this section, like the previous section, different state-space models of the 2L2JM were studied. The manipulator in this section has 2 rigid modes as its revolute joints are not constrained. For the balanced realization, first, these modes were removed and then balancing was applied. Then, the rigid modes were added to the balanced oscillatory system to form the balanced full

order model. It is noted that Gramians exists only for the stable systems *i.e.*, system poles are on the left-hand plane. Therefore, the rigid modes need to be removed for balancing and model reduction, and finally, they are added to the system. The time step for the state-space and FEA-A simulations in this section was $5e-4s$ for the entire duration.

Figure 3.11 shows three different state-space models of the manipulator that are compared with the transient module of FEA-A.

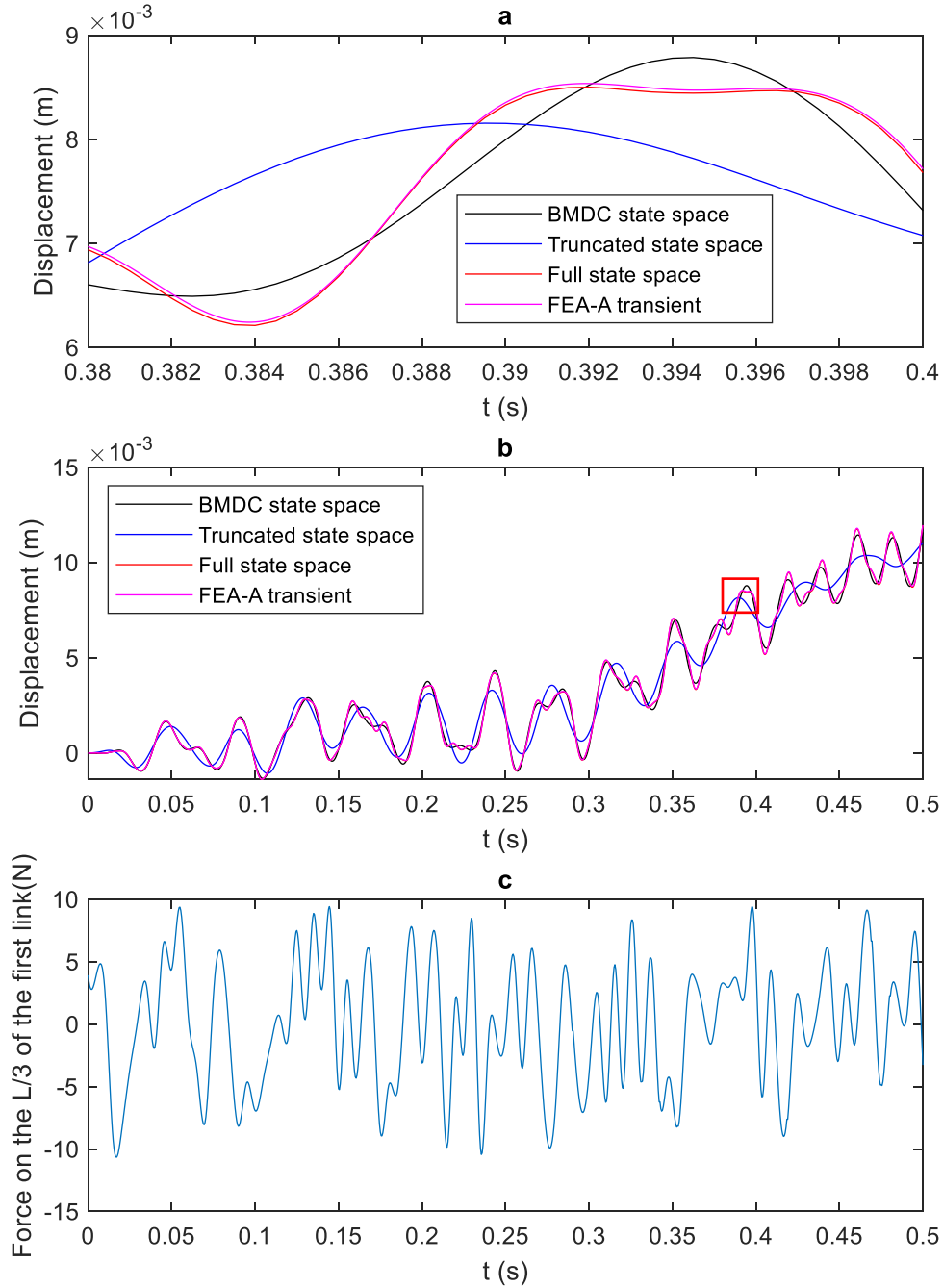


Figure 3.11. 2L2JM's tip displacement and moment for 3 different state-space models as well as FEA-A transient. a- the response for small time duration, for comparison, b- the response for 0.5 second interval, c- an arbitrary excitation Force between [-10,10] N applied on L/3 of the first link.

As shown in Figure 3.11, the red and magenta plot on top of each other. It proves that the full order mathematical model with a state matrix of 40 by 40 is almost the same as the FEA-A. This indicates the accuracy of the full order model with only 4 master DOFs and 20 modes. More importantly, the black line which is for the BMDC model with state matrix of 8 by 8 comply with the FEA-A. This indicates the accuracy and efficiency of the BMDC with only 4 master nodes and 4 modes. Here, since the manipulator has more complex geometry the balancing effect is obvious between BMDC and the Truncated algorithms. The difference index of the models was represented by normalized RMS values in Table 3.5.

Table 3.5. Normalized RMS values of different models and their comparison with FEA-A transient for the 2L2JM.

	Full order	BMDC	Truncated
Normalized RMS	0.0471	0.2612	1

According to Table 3.5, the normalized RMS values show that the full order and BMDC were almost the same as the FEA-A transient values; however, the Truncated model has shown the worst performance among the 3 state-space models.

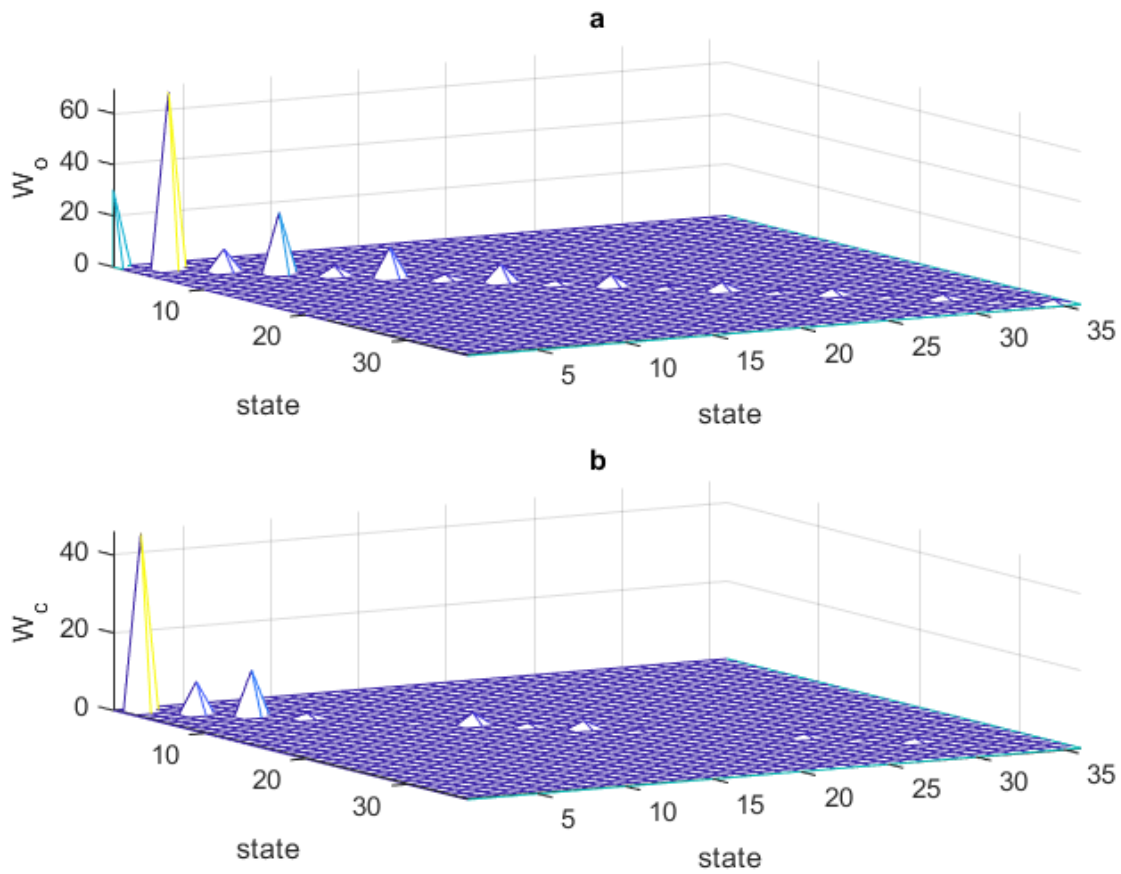


Figure 3.12. 2L2JM, full oscillatory model, a. Observability Gramian and b. Controllability Gramian.

According to Figure 3.12, the Gramians of the 36 states or the 18 oscillatory modes from unbalanced model are scattered in the plane of the states. It is noted that truncation before balancing could remove the states with higher priority in terms of observability or controllability. That is the reason why the Truncated (blue line) had the worst performance in Figure 3.11. However, the BMDC (black line) had covered the FEA-A or the full model behavior with just 4 modes.

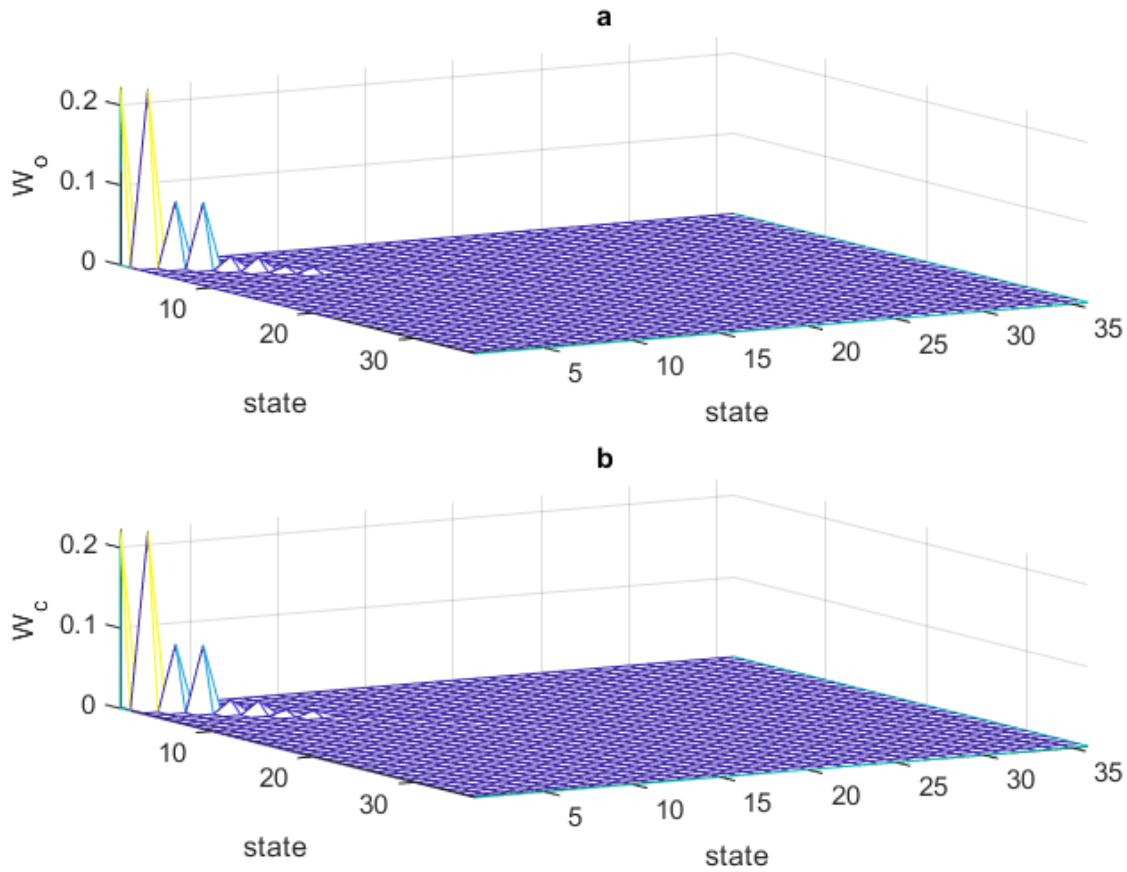


Figure 3.13. 2L2JM, balanced-full oscillatory model, a. Observability Gramian and b. Controllability Gramian.

As shown in Figure 3.13, the balanced algorithm made both Gramians equal and sorted. Then model reduction would consider mode priorities. It is obvious that the first 2 modes or 4 states (plus the 2 rigid modes) would give almost the entire dynamic behavior of the system.

3.11 Results, 5-DOF manipulator

In this part, like the last 2 parts, the different state-space models are compared with FEA-A transient then the Gramians are discussed. The state-space matrices for the 5-DOF manipulator are given in Appendix M. The time step for the state-space and FEA-A simulations in this section was 1e-3s for the entire duration.

Figure 3.14 shows three different state-space models of the manipulator that are compared with the FEA-A results. The disturbance generated here was based on an arbitrary excitation with the frequency of 25Hz to mostly excite the sixth mode of the 5-DOF manipulator with the free base and free joints (Appendix B). This was because the sixth mode was the first oscillatory mode of this manipulator in vertical direction. In other words, any excitation with a lower frequency would only show the rigid motion of the manipulator.

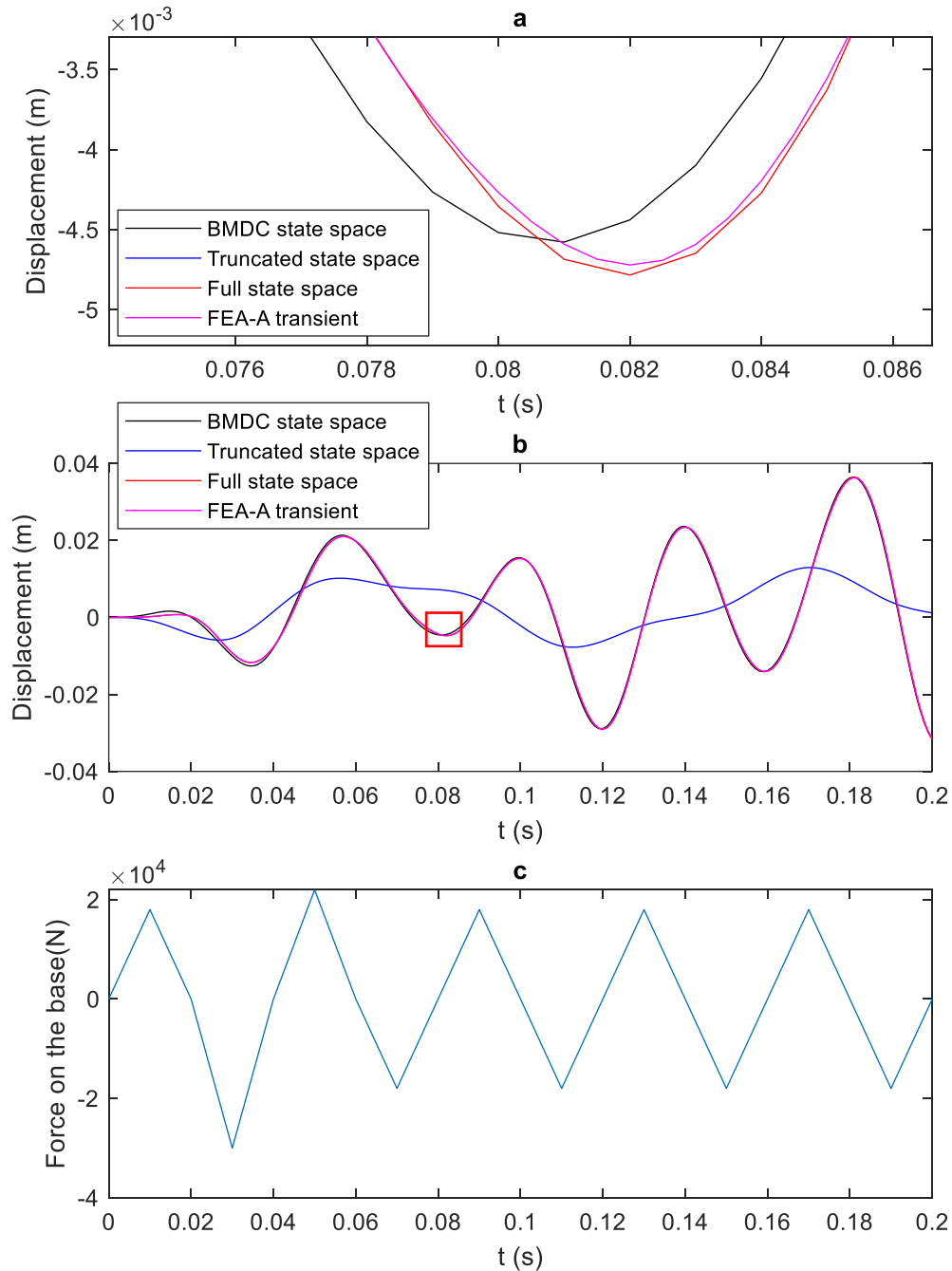


Figure 3.14. 5-DOF manipulator tip displacement and moment for 3 different state-space models as well as FEA-A transient. a- the response for small time duration, for comparison, b- the response for 0.2 second interval, c- an arbitrary excitation force between $[-2,2]$ kN applied on the base.

As shown in Figure 3.14, the red and magenta plot on top of each other. It proves that the full order mathematical model with a state matrix of 60 by 60 is almost the same as the FEA-A. This

indicates the accuracy of the full order model with only 8 master DOFs and 30 modes. More importantly, the black line which is for the BMDC model with state matrix of 10 by 10 comply with the FEA-A. This indicates the accuracy and efficiency of the BMDC with only 8 master nodes and 5 modes. Here, since the manipulator had more complex geometry than the two other geometries, the balancing effect is obvious between BMDC and the Truncated algorithm. The difference index of the models was represented by normalized RMS values in Table 3.6.

Table 3.6. RMS values of different models and their comparison with FEA-A transient for the 5-DOF manipulator.

	Full order	BMDC	Truncated
Normalized RMS	0.0765	0.0573	1

According to Table 3.6, the normalized RMS values show that the full order and BMDC were almost the same as the FEA-A transient values; however, the Truncated model has not shown the behavior of the system.

As discussed in section 3.4, the balanced realization deals with Gramians. Diagonal elements of the controllability or observability Gramian give information about the relative controllability or observability of the different modes, respectively. The balancing algorithm finds a direction to make both observability and controllability Gramians equal and sorted.

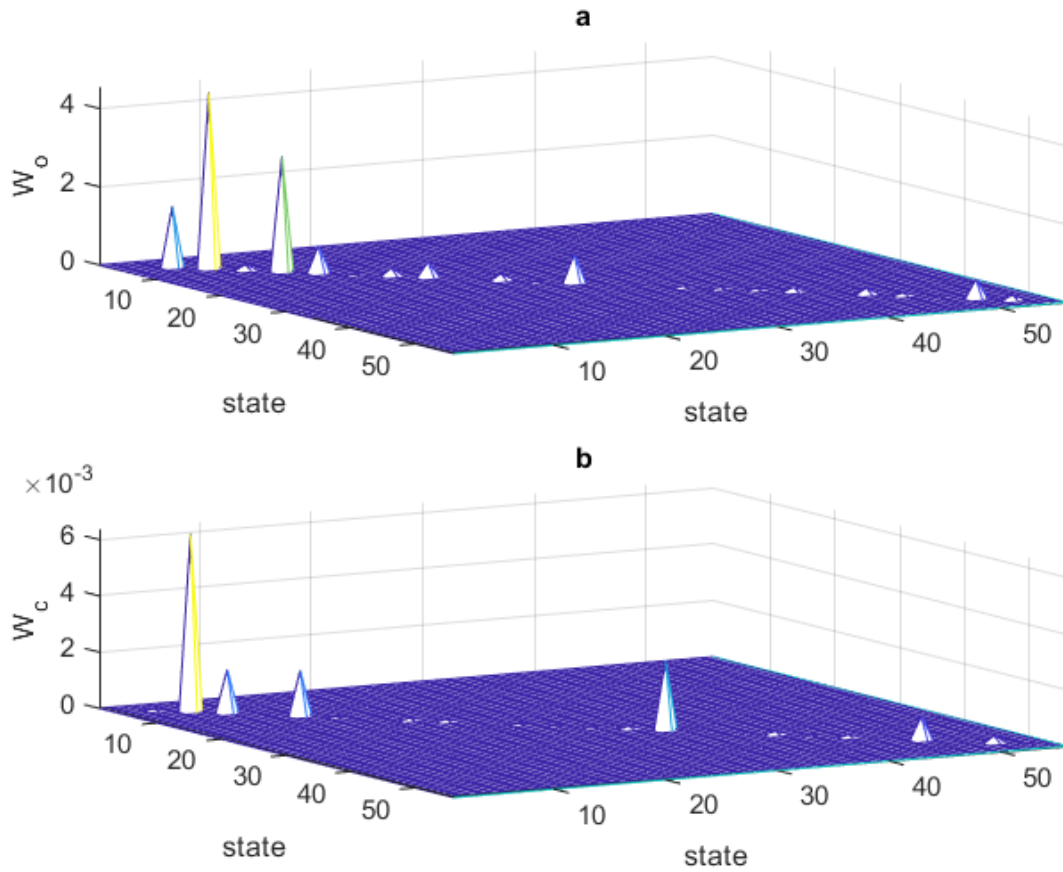


Figure 3.15. 5-DOF manipulator, full oscillatory model, a. Observability Gramian and b. Controllability Gramian.

According to Figure 3.15, the Gramians of the 54 states or the 27 oscillatory modes from unbalanced model are scattered in the plain of the states. It is noted that truncation before balancing could remove the states with higher priority in terms of observability or controllability. That is the reason why the truncated (blue line) has the worst performance in Figure 3.14. However, the BMDC (black line) has covered the FEA-A or the full model behavior with just 5 modes.

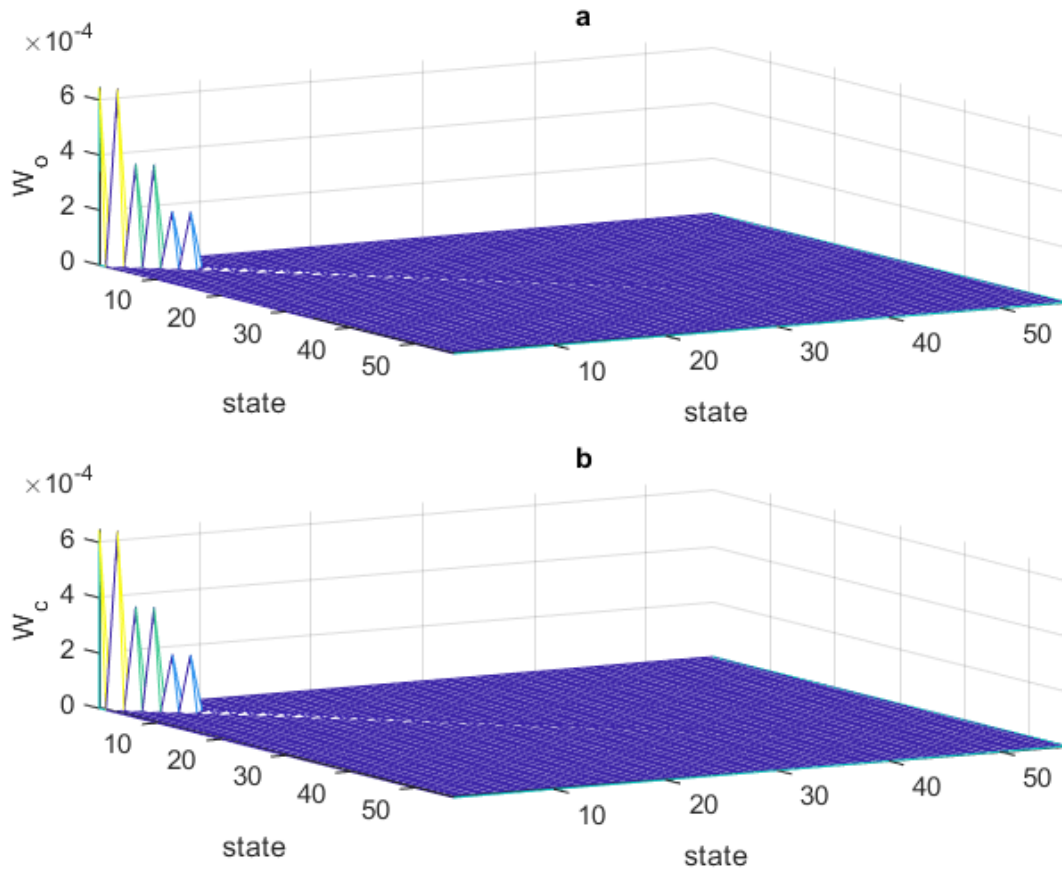


Figure 3.16. 5-DOF manipulator, balanced-full oscillatory model, a. Observability Gramian and b. Controllability Gramian.

As shown in Figure 3.16, the balanced algorithm makes both Gramians equal and sorted. Then truncating would consider mode priorities. It is obvious that the first 3 modes or 6 states (plus the 3 rigid modes) would give almost entire dynamic behavior of the system. However, for the system response in Figure 3.14, 2 oscillatory modes were sufficient for the BMDC. Therefore, only 2 oscillatory modes plus the 3 rigid modes were used.

3.12 Summary

In this chapter the finite element models of manipulators were discussed. First the manual FEM was used to obtain the equation of motion for the cantilever beam and the 2L2JM. Then they were verified with the manual FEM using the change index. Second, state-space models were obtained

based on the eigenvectors from FEA-A using the principal coordinate method. In addition, a model reduction algorithm was presented to reduce the order of the obtained models from eigenvectors. The resulting state-space models are presented in Appendixes K, L, and M. Finally, the responses of the state-space models under random vibration were tested. The result of the models compared with transient module obtained from FEA-A showed the effectiveness of the modeling and reduction approach.

Chapter 4. Vibration Controller Design

In this chapter, the verified models were used to design closed loop systems to control the vibration. Based on the definition in [40], “the closed-loop system compensates for disturbances by measuring the output response, feeding that measurement back through a feedback path, and comparing that response to the input at the summing junction. If there is any difference between the two responses, the system drives the plant (plant includes the process system and the actuator), via the actuating signal, to make a correction. If there is no difference, the system does not drive the plant, since the plant’s response is already the desired response”. The models used in this chapter were both the full and reduced models obtained in Chapter 3 (open loop systems). Based on [40], “Open-loop systems, then, do not correct for disturbances and are simply commanded by the input”. The cantilever beam was assumed to be a SISO (single-input-single-output) problem; *i.e.*, the actuator moment at $L/3$ was the input, and the manipulator’s tip displacement was the output. The controller for this problem was a linear quadratic regulator (LQR).

The 2L2JM manipulator had 2 joint torques as the input actuators and its tip’s displacement as the output. Also, a linear force was assumed to be the disturbance at $L/6$ of the first link. Since this problem had multiple inputs, it was MIMO (multi-input-multi-output), so the classic controllers could not be used. The controller for this manipulator was an optimal controller called H_∞ . This controller is also a robust controller that could cope with uncertainties and disturbances, so it paved the way for the 5-DOF problem with complexity.

For the 5-DOF manipulator, the moment of the 2nd and 3rd joints were inputs, and the tip displacement was the output. The 5-DOF manipulator had a quite complex geometry and the simplification in the modeling led to uncertainties. However, this thesis was not meant to deal with the manipulators’ uncertainties. Instead, the H_∞ controller could compromise between different controlling purposes of a MIMO problem by solving an optimization problem. Therefore, the main purpose of this thesis, which was neutralizing the disturbance from the base, could be achieved.

4.1 Vibration controller using LQR for cantilever beam

The controller in this part was designed based on the full order model and the BMDC reduced model of section (3.6). In the previous chapter, the state-space models were derived using 20 modes of the cantilever beam from modal module of FEA-A. For the full order model all the 20 modes were used without any changes; however for the BMDC model, the full order model was balanced, and the first two modes were used for the final state-space model.

As shown in Figure 4.1, LQR shows the structure of a state feedback controller. The purpose of LQR is to find a proper feedback by solving an optimization problem. For the cantilever problem, the tip displacement due to base excitation should reduce to zero, so the reference for this system was zero. Despite the good performance of LQR controller, it has a main flaw. Robust stability could not be ensured, so it is vulnerable to uncertainties.

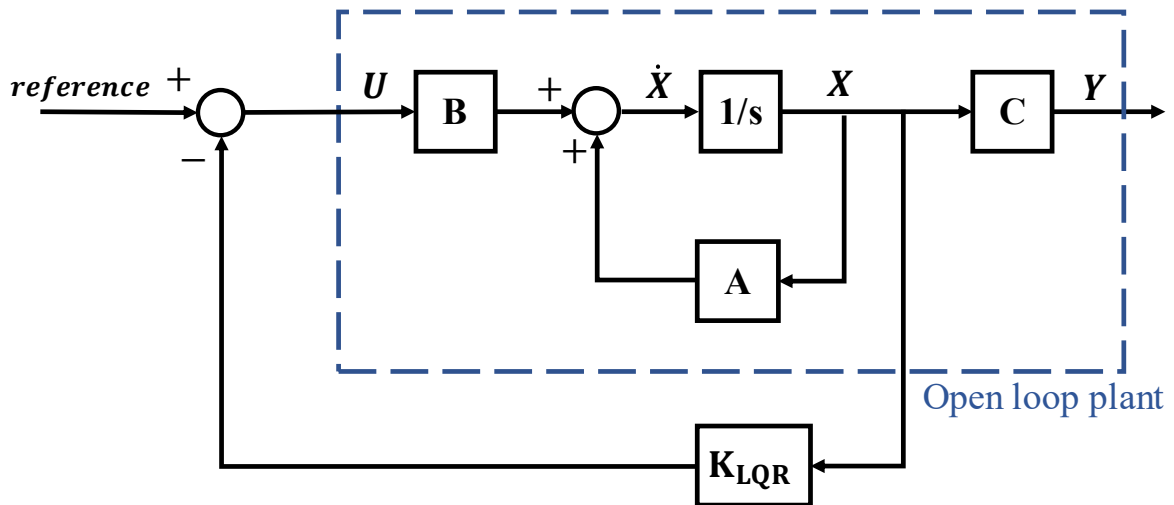


Figure 4.1. Structure of a LQR state feedback controller.

The objective is to minimize the following quadratic cost function to find the optimum K_{LQR} which is the controller gain:

$$J = \frac{1}{2} \int_0^{\infty} (X^T Q X + U^T R U) dt \quad 4-1$$

where Q and R are positive semi-definite weighting matrices and U and X is the control input and state vector, respectively.

The control force is:

$$U = -K_{LQR}X \quad 4-2$$

where K_{LQR} is the optimal controller gain. For more information on how to obtain the LQR controller gain, refer to appendix N.

4.2 Vibration controller- cantilever beam results

In this section, four different models of the cantilever beam were exposed to impulse and random vibration. The 4 models were full order open loop (FOL), full order closed loop (FCL), reduced order open loop (ROL), and reduced order closed loop (RCL). The open loop state-space systems used in this section were based on the matrices in Appendix K. For the reduced models, only BMDC was used. The closed loop model was designed based on LQR, and the weight functions were chosen by trial and error. This procedure was made in M-software using the command “lqr”. Finally, bode diagrams were depicted to compare the models over the frequency domain. Bode diagrams are used to measure the magnitude of frequency response of a system. Through this plot, the closed-loop performance, especially, over the natural frequencies was depicted. Bode diagrams were generated using the “bode” command over a desired range of frequencies in M-software. It is noteworthy that, since the system for the cantilever beam was SISO, the disturbance was exerted on the same channel as the control input.

In Figure 4.2, the impulse response of the closed loop system of the cantilever beam is shown. In theory, the impulse is infinite at $t=0$ and zero elsewhere; however, in the simulation it has a unit value for the first iteration of the differential equation solver. As discussed in section 3.8, the “impulse” command chooses the time step based on the dynamics of the system. Here, the time step for FCL, FOL, RCL, and ROL were $4e-5s$, $4e-5s$, $1e-3s$, and $1e-3s$, respectively. According to plot (a), the open loop system for both the full order model and the reduced order model had lost 80% of its tip displacement within 2 seconds. Whereas, according to plot (b), for the closed

loop systems the tip displacement has lost all its magnitude within 2 seconds. The tip displacement of the full order model and the reduced order models show some insignificant differences except at the beginning. This implies that not only does the reduction have no adverse effect on the system's response, but it also helped to reduce the computation time. Plot (c) depicts the controller efforts. It shows that the full order model has made extra effort to damp the high frequency modes of vibration; however, the reduced order model has not made any extra effort (the difference between the red and black plot in $[0,0.2]$ s), and the material damping of the beam ($\zeta = 0.02$) is in charge of attenuating high frequency modes. Since both models have the same results, it proves that the extra effort made by the full order closed loop model was unnecessary.

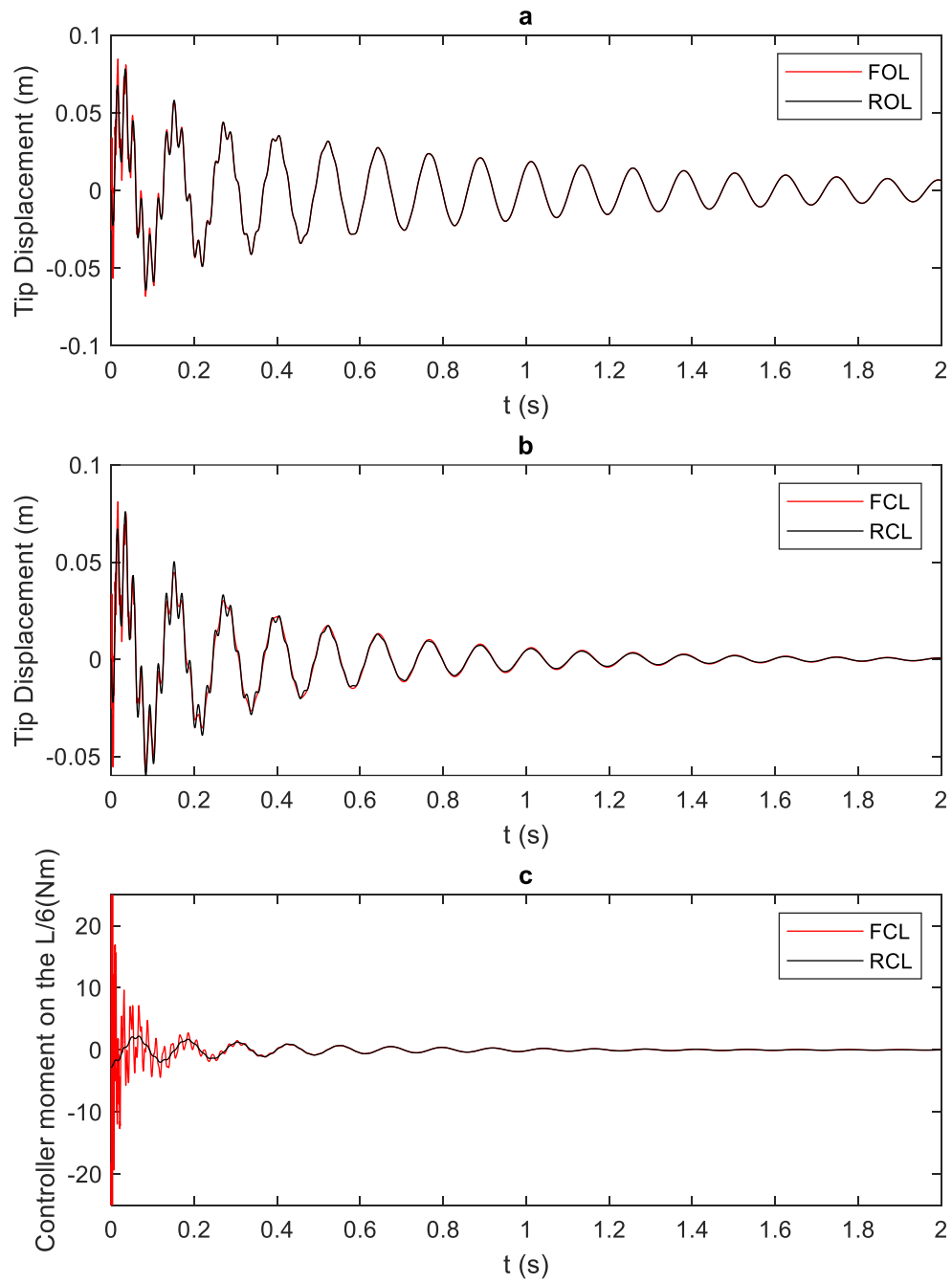


Figure 4.2. Vibration response of a cantilever beam due to an impulse moment exerted at $L/6$ from its base at zero-time, (a) tip displacement of the open loop systems, (b) tip displacement of the closed loop systems, (c) the controller effort.

Since the main purpose of this thesis was random vibration attenuation of manipulators, an arbitrary vibration was exerted on the manipulator and the responses of the 4 models were compared here. Figure 4.3 shows the overall performance of the closed loop systems for both full and reduced order models. As this figure shows, the red lines (closed loop) have an insignificant amount of vibration compared to the black lines (open loop). This implies that the closed loop systems have dampened the vibration effectively (the effectiveness index is explained in page 64). The time step for this simulation was 5×10^{-4} s for the entire duration.

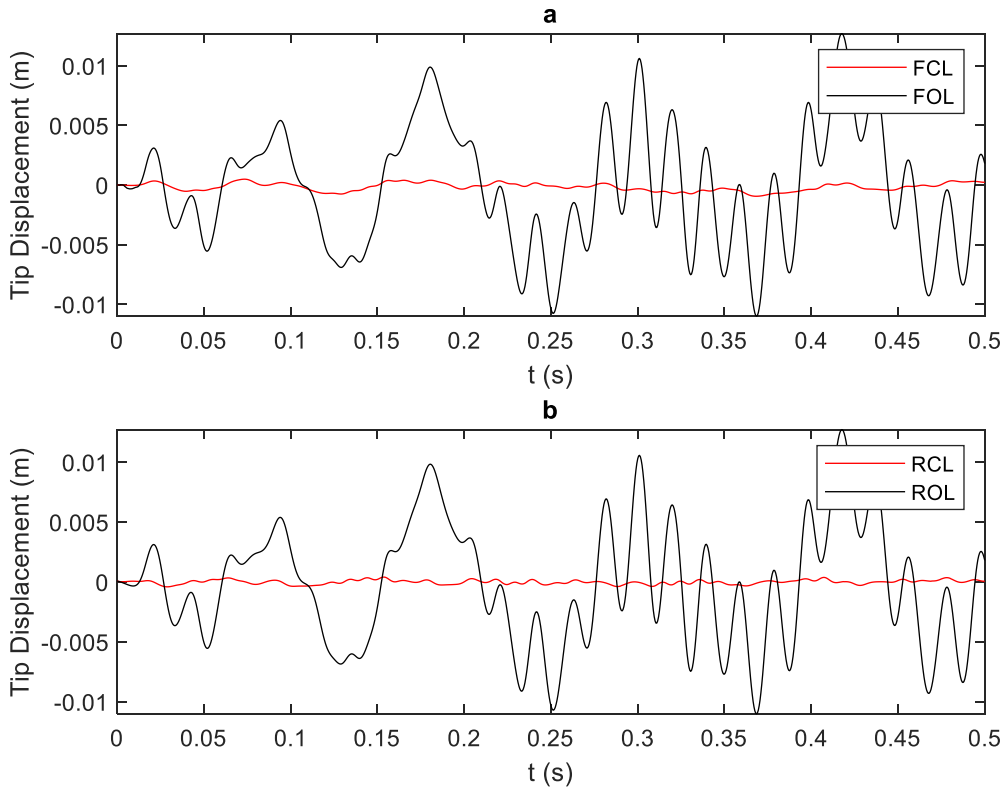


Figure 4.3. Vibration response of a cantilever beam due to an arbitrary vibration $[-10,10]$ Nm moment exerted at $L/6$ from its base. (a) tip displacement of the full order systems. (b) tip displacement of the reduced order systems.

The target performance of the controller was set to keep the displacement of the tip below 5mm. According to Figure 4.4, the tip displacements of the closed loop systems have obtained the target performance.

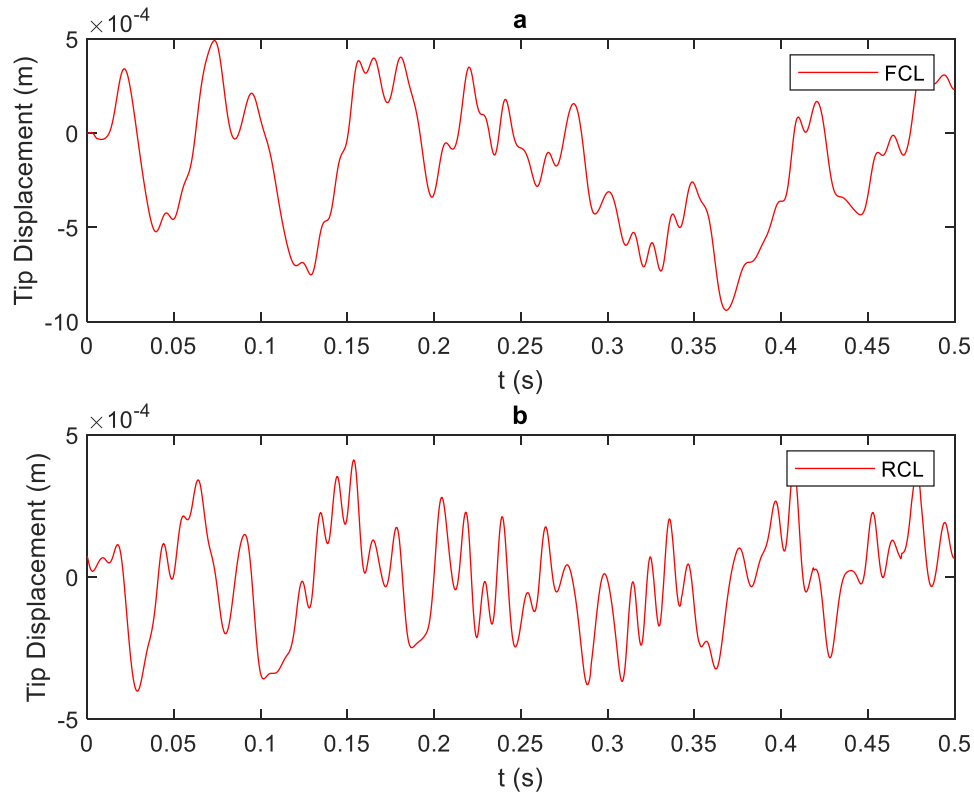


Figure 4.4. Vibration response of the closed loop cantilever beam systems due to an arbitrary vibration $[-10,10]$ Nm moment exerted at $L/6$ from its base. (a) tip displacement of the full order systems. (b) tip displacement of the reduced order system.

According to Figure 4.5, plot (a) shows that the controllers have made almost the same effort to attenuate the arbitrary excitation. This again indicates that the first 2 modes of vibration were sufficient to control the vibration of the tip of the beam. Plot (b) shows that the disturbance, which was applied as an arbitrary vibration $[-10,10]$ Nm moment at $x=L/6$.

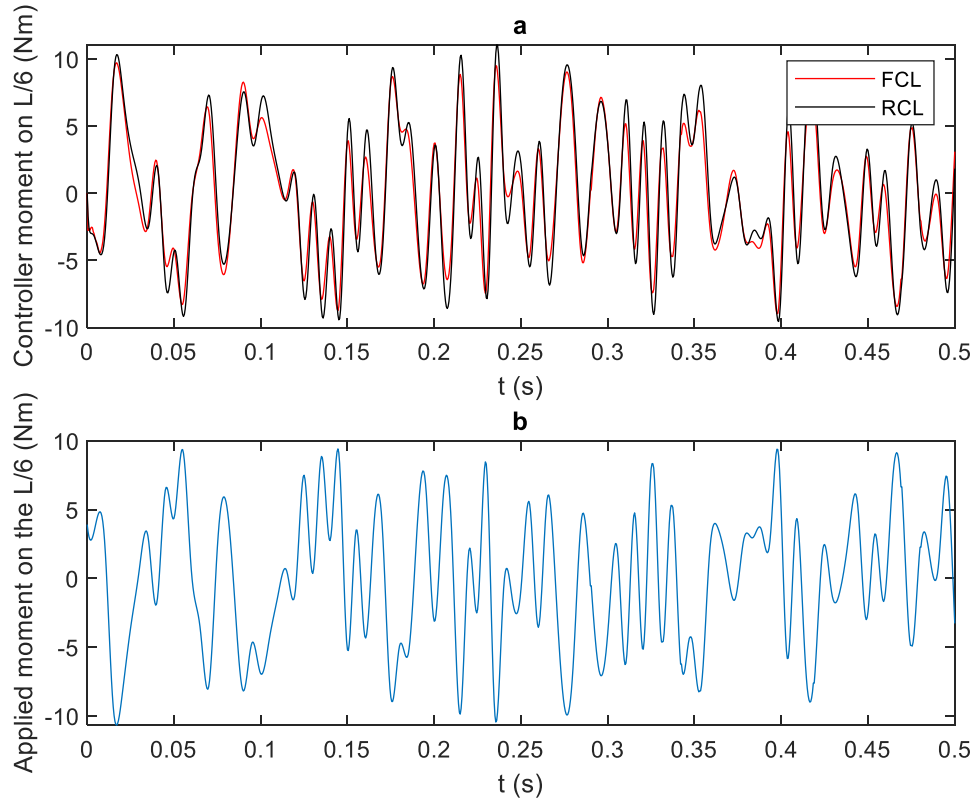


Figure 4.5. Cantilever beam results, (a) controller efforts of the full order and reduced order closed loop models (FCL and RCL), (b) disturbance as an arbitrary vibration [-10,10] Nm moment exerted at $x=L/6$.

The effectiveness index of the controller is specified by H_∞ norm of the system. Based on definition, “It describes the maximum energy gain of the system and is decided by the peak value of the largest singular value of the frequency response matrix over the whole frequency axis” [41]. It is defined as follows:

$$\|G\|_\infty = \sup_{\omega \in R} \|G(j\omega)\|_2 \quad 4-3$$

where G is the system transfer function that could be the overall closed loop system or the open loop system. In the definition of the H_∞ norm of the system in equation (4-3), $\| \cdot \|_2$ stands for the second norm, which is defined as follows:

$$\|G\|_2 = \left[\frac{1}{2\pi} \int_{-\infty}^{+\infty} |G(j\omega)|^2 d\omega \right]^{\frac{1}{2}} \quad 4-4$$

The Cantilever model is a SISO system. The H_∞ norm for a SISO system is the largest value of the frequency response magnitude. The bode diagrams are shown in Figure 4.6, part (a) shows that LQR has reduced the H_∞ norm of the system by 20 dB; *i.e.*, the controller at the first resonance (worst case scenario) has reduced the magnitude of vibration at the tip by 10 times. Figures 4-5b and 4-5c compare the closed loop of the reduced model with the full and reduced order open loop models. They imply a 30 dB reduction in the H_∞ norm of the system after using LQR; *i.e.*, the controller at the first resonance (worst case scenario) has reduced the magnitude of vibration at the tip by $10^{30/20}$ times.

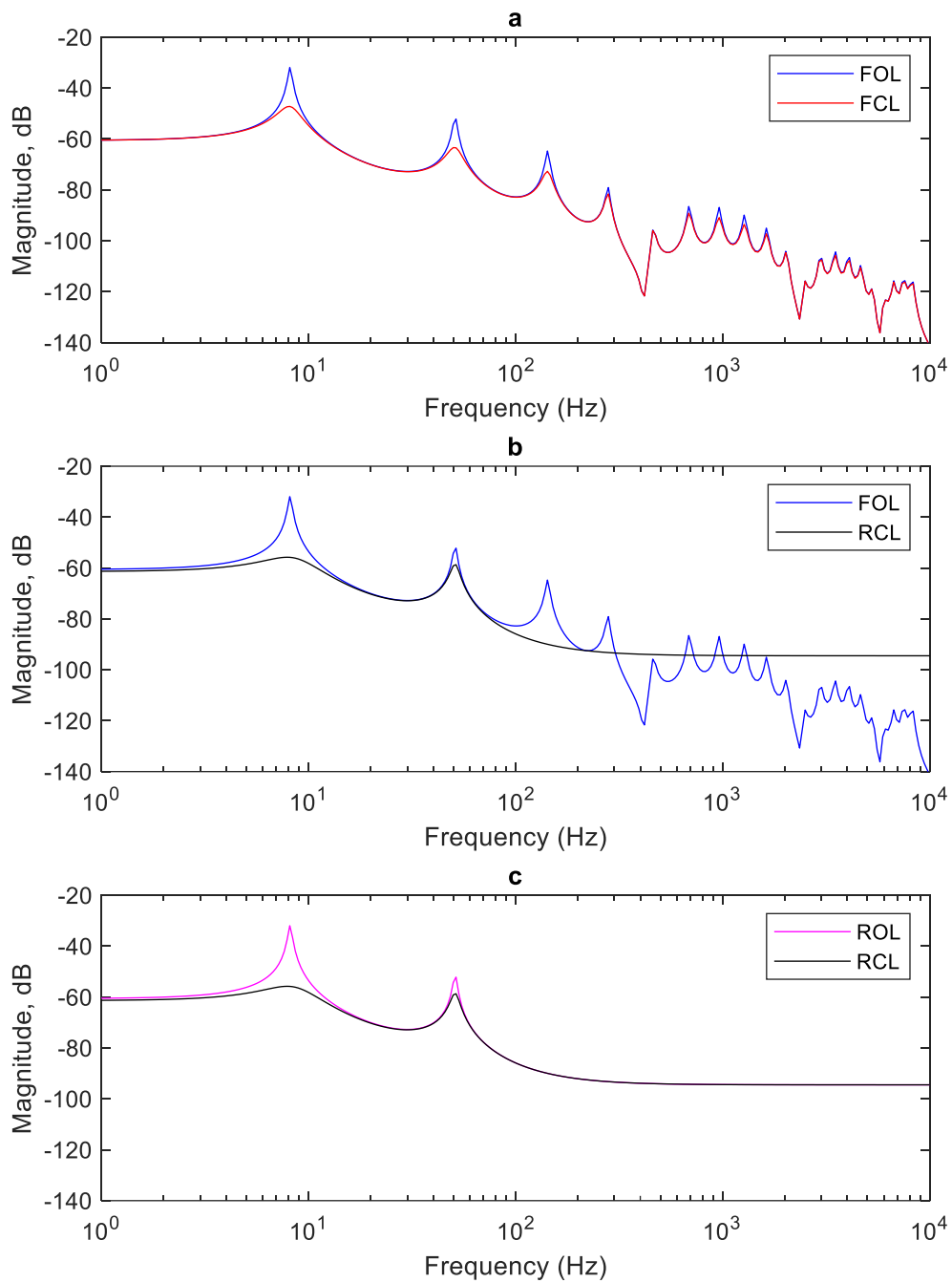


Figure 4.6. Bode diagram of the cantilever beam; (a) full order open loop and closed loop systems. (b) full order closed loop and reduced order open loop systems. (c) reduced order open loop and closed loop systems.

The results in this section showed the effectiveness of the controller for both reduced and full order models. The reduced model could achieve the same results as the full order model, but the reduced order model has less computational burden on the processor. The models in this section were based on the full order and BMDC matrices in Appendix K. The results in this section were just simulations that were not verified. The verification would be through practical test that is beyond the scope of this study.

4.3 Vibration control using H_∞ for 2L2JM and 5-DoF manipulator

The 2L2JM and 5-DOF manipulator are recognized as MIMO systems since they both have 2 inputs and one output. To deal with MIMO systems a H_∞ controller was proposed. This controller compromises between different controlling purposes of a MIMO problem by solving an optimization problem. These purposes could be reference tracking, actuator performance and disturbance and noise rejection[41].

Considering Figure O-2 in appendix O, the ability for tracking is defined by the transfer function from r to e as follows:

$$T_{er}(s) =: \frac{E(s)}{R(s)} = (I + G(s)K(s))^{-1} \quad 4-5$$

where $E(s)$ and $R(s)$, are the error and input signal in Laplace space, respectively. This transfer function is called sensitivity and it is represented by S . To have good tracking performance in a certain frequency ω , the sensitivity magnitude should be less than a small positive value:

$$|S(j\omega)| < \epsilon(\omega) \quad 4-6$$

The inequality can be normalized with a weighting function $W_s(\omega) = 1/\epsilon(\omega)$:

$$|S(j\omega)W_s(j\omega)| < 1 \quad 4-7$$

This inequality over the entire frequency domain could be shown as below:

$$\|S W_s\|_\infty < 1 \quad 4-8$$

According to the definition of infinity norm, equation (4-8) ensures that the system at any frequency would track the reference. Similarly, for efficient actuator performance (refer to equation O-4), the condition should be as follows:

$$\|K S W_u\|_\infty < 1 \quad 4-9$$

The H_∞ controller is a multi-objective controller that solves an optimization problem between different control criteria. Therefore, the inequalities (4-8, 4-9) could be written as follows:

$$\min_K \left\| \begin{matrix} S W_s \\ K S W_u \end{matrix} \right\|_\infty \quad 4-10$$

More information about this controller has been given in Appendix O. According to Figure O-2 in Appendix O, the manipulators' external input is the disturbance. In addition, control inputs are the joints torque, and measured output is the tip displacement. The manipulator controllers were designed to achieve reference tracking, actuator performance and disturbance rejection. Therefore, the outputs to be minimized are the tracking error and control input.

4.4 Vibration controller- two-link two-joint manipulator (2L2JM) results

In this section, the random vibration attenuation has been studied for the 2L2JM. The 4 models are FOL, FCL, ROL, and RCL which stand for full order open loop, full order closed loop, reduced order open loop, and reduced order closed loop, respectively. The open loop state-space systems used in this section were based on the matrices in Appendix L. For the reduced models, BMDC was only used. The closed loop model was designed based on a H_∞ controller, and the weight functions were chosen by trial and error. This controller was designed based on “hifsyn” in M- software. Finally, bode diagrams were depicted to compare the models over frequency domain. A

bode diagram is used to measure the magnitude of frequency response of a system; *i.e.*, the tip displacement magnitude over the entire frequency domain. Through this plot, the closed-loop performance, especially, over the natural frequencies was depicted. It is noteworthy that the system is MIMO, meaning, there are 3 inputs: 2 of them are the joints' moments that act as control input, and one is the disturbance which is a linear force applied on the $L/3$ of the first link. The time step for the simulations in this section was $5e-4s$ for the entire duration.

Figure 4.7, compares the open loop and closed loop full order models in presence of an arbitrary vibration. The red line in (a) shows that the tip of the manipulator fluctuates around the origin when the controller is active which proves the successful performance of the controller. The target performance of the controller was set to keep the displacement of the tip below 5mm. Plot (b) shows the zoomed closed loop performance. It shows that the controller has reduced the tip vibrations to the range of $[-4,4]$ mm. Therefore, the tip displacement of the closed loop system has obtained the target performance. Plot (c) is the disturbance time series for the duration of 0.5s. This disturbance was an arbitrary vibration intended to resemble the vibration of the rough terrain. For having an accurate pattern of the rough terrain some experimental data should be recorded.

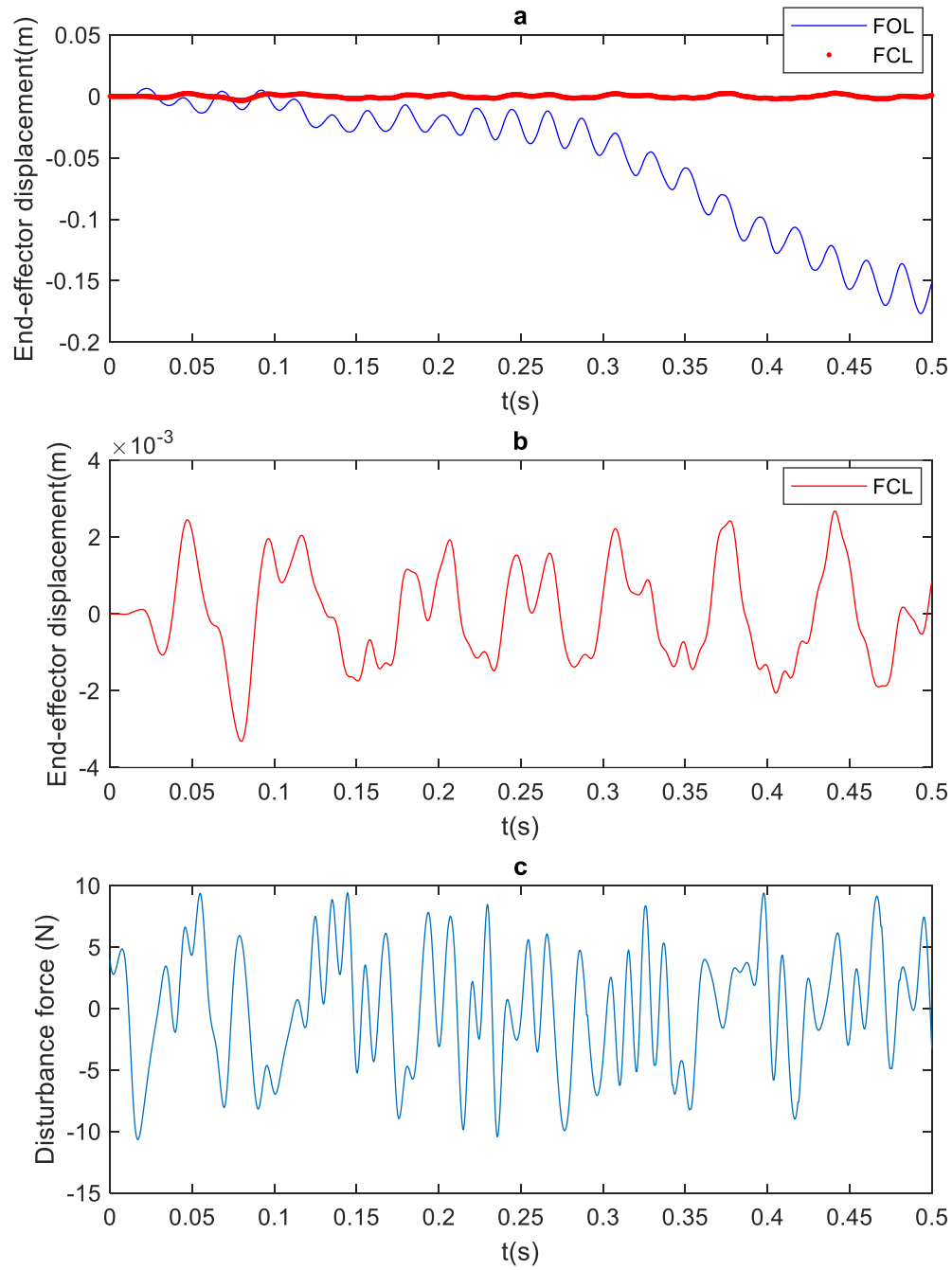


Figure 4.7. 2L2JM results, (a) tip displacement of the full order open loop and closed loop models (FOL and FCL), (b) zoomed closed loop tip displacement, (c) disturbance as an arbitrary vibration $[-10,10]$ N linear force exerted at $x=L/3$ of the first link.

Figure 4.8 shows the controller effort; *i.e.*, the amount of moment that is produced by the joints to attenuate the vibration. Controller effort shows how the controller has achieved the desired performance. In 2L2JM, the joints have made an effort within $[-2,2]$ Nm. Using this value, one could provide suitable actuators in a real experiment.

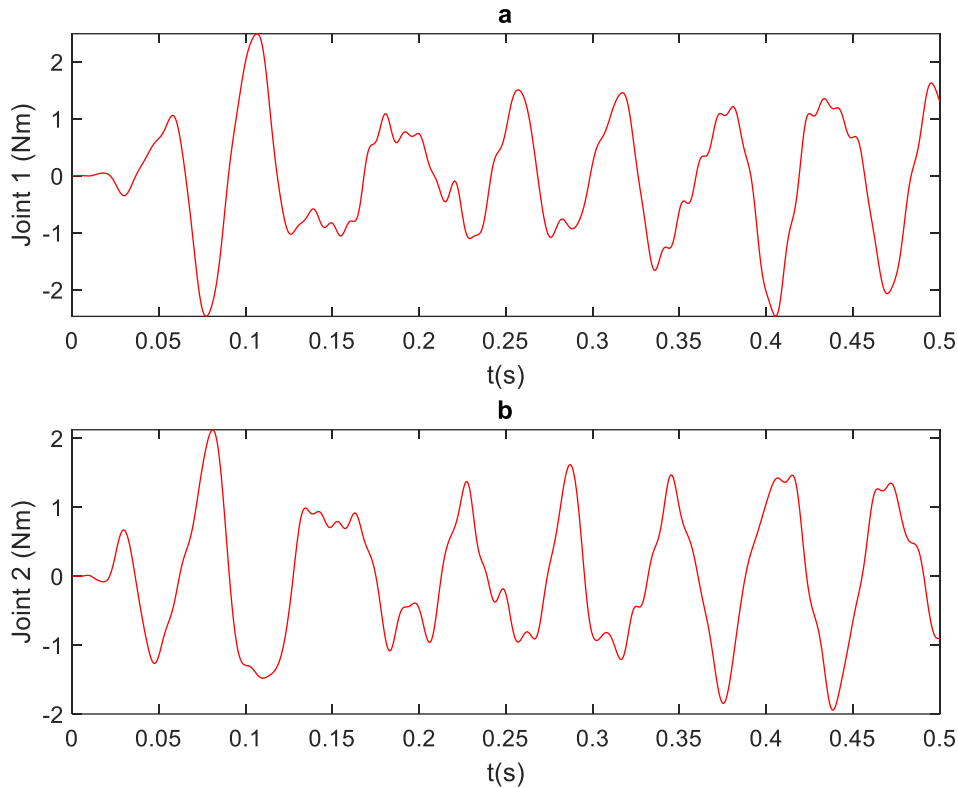


Figure 4.8. 2L2JM full order model results, (a) joint 1 controller effort, (b) joint 2 controller effort.

Figure 4.9, which is similar to Figure 4.6, but it compares the open loop and closed loop of reduced order (BMDC with 4 modes) models in the presence of the arbitrary vibration. The red line in (a) shows that the tip of the manipulator fluctuates around the origin when the controller is active which proves the successful performance of the controller. The target performance of the controller was set to keep the displacement of the tip below 5mm. Plot (b) shows the zoomed closed loop performance. It shows that the controller has reduced the tip vibrations to the range of

[-4,4] mm. Therefore, the tip displacement of the closed loop system has obtained the target performance. Plot (c) is the disturbance time series for the duration of 0.5s.

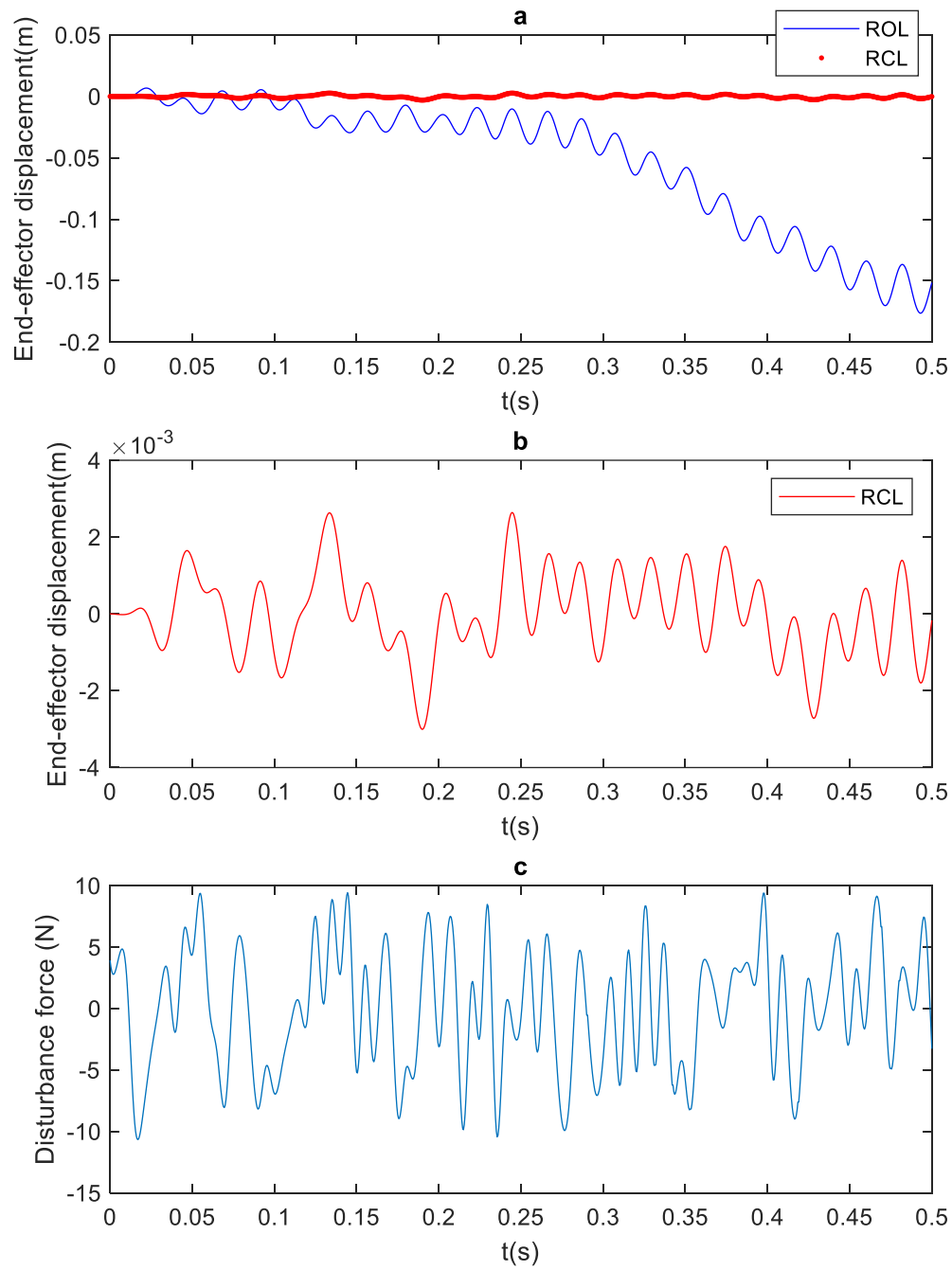


Figure 4.9. 2L2JM results, (a) tip displacement of the reduced order open loop and closed loop models (FOL and FCL), (b) zoomed closed loop tip displacement, (c) disturbance as an arbitrary vibration [-10,10]N linear force exerted at $x=L/3$ of the first link.

Figure 4.10 shows the controller effort, *i.e.*, the amount of force that is produced by the joints to attenuate the vibration. Comparing Figure 4.8 and Figure 4.10, the actuators have made an effort in the range of $[-2,2]$ Nm. This indicates that, using the reduced model, one could chose the suitable actuators for the vibration suppression of the manipulator.

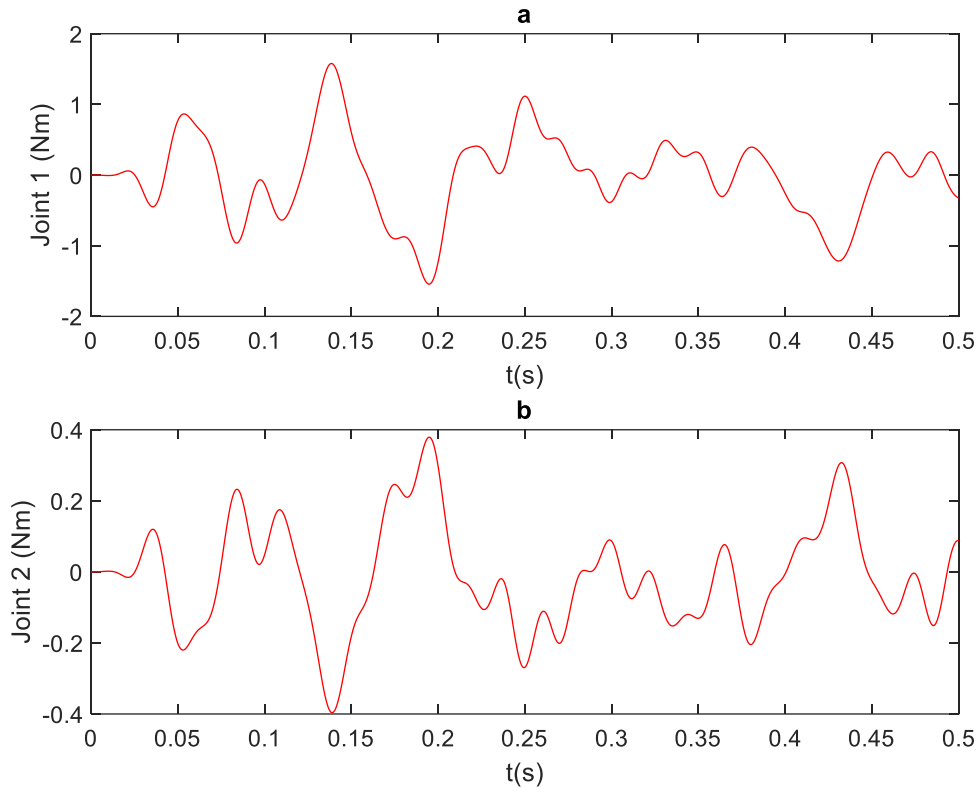


Figure 4.10. 2L2JM reduced order model results, (a) joint 1 controller effort, (b) joint 2 controller effort.

The 2L2JM model is a MIMO system. Considering equation (4-3), the H_∞ norm for a MIMO system is the largest singular value of the system (open loop or closed loop) across frequencies. The bode diagrams are shown in Figure 4.11; part (a) shows that the H_∞ controller has reduced the H_∞ norm of the full order system from infinity to -58.2dB . Besides, in part (b) the controller has reduced the H_∞ norm of the reduced order system (BMDC with 4 modes) from infinity to -54.2dB . This infinite value is due to the rigid modes of the manipulator. These modes are not shown in the figure since they occur at a frequency of zero Hz.

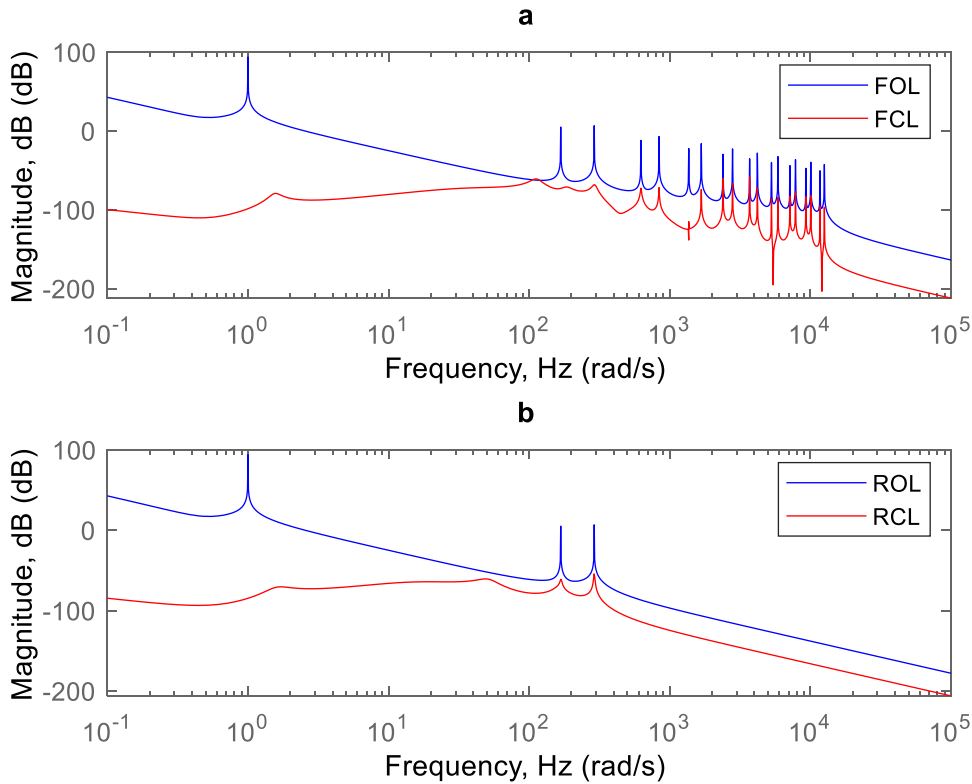


Figure 4.11. Bode diagram of the 2L2JM, (a) full order open loop and closed loop systems, (b) reduced order closed loop and open loop systems.

The results in this section showed the effectiveness of the controller for both reduced and full order models. The reduced model could achieve the same results as the full order model, but the reduced order model had less computational burden on the processor. The models in this section were based on the full order and BMDC matrices in Appendix L. The results in this section were just simulations that were not verified. The verification would be through practical test that is beyond the scope of this study.

4.5 Vibration controller- 5-DOF manipulator results

This section reports the results of simulation of random vibration (arbitrary vibration) attenuation for the 5-DOF manipulator. The 4 models used were FOL, FCL, ROL, and RCL which stand for full order open loop, full order closed loop, reduced order open loop, and reduced order

closed loop, respectively. The open loop state-space systems used in this section were based on the matrices in Appendix M. For the reduced models, only the BMDC was used. The closed loop model was designed based on a H_∞ controller, and the weight functions were chosen by trial and error. Finally, bode diagrams were depicted to compare the models over frequency domain. A bode diagram is used to measure the magnitude of frequency response of a system. Through this plot, the closed-loop performance, especially, over the natural frequencies was depicted. It is noteworthy that the system is MIMO, meaning, there are 3 inputs: 2 of them are the joints' moments that act as control input, and one is the disturbance which is a linear force applied to the base of manipulator. The time step for the simulations in this section was $5e-4s$ for the entire duration.

Figure 4.12 compares the open loop and closed loop full order models in the presence of an arbitrary vibration which in that way resembles the rough terrain of the farm field. The red line in (a) shows that the tip of the manipulator fluctuates around the origin when the controller is active which indicates the successful performance of the controller. The target performance of the controller was set to keep the displacement of the tip below 1mm. Plot (b) shows the zoomed closed loop performance which indicates the controller has made the tip vibration reduced to the range of $[-0.4,0.4]$ mm. Therefore, the tip displacement of the closed loop system has obtained the target performance. Plot (c) is the disturbance time series. The performance index of the controller is given in Figure 4.15.

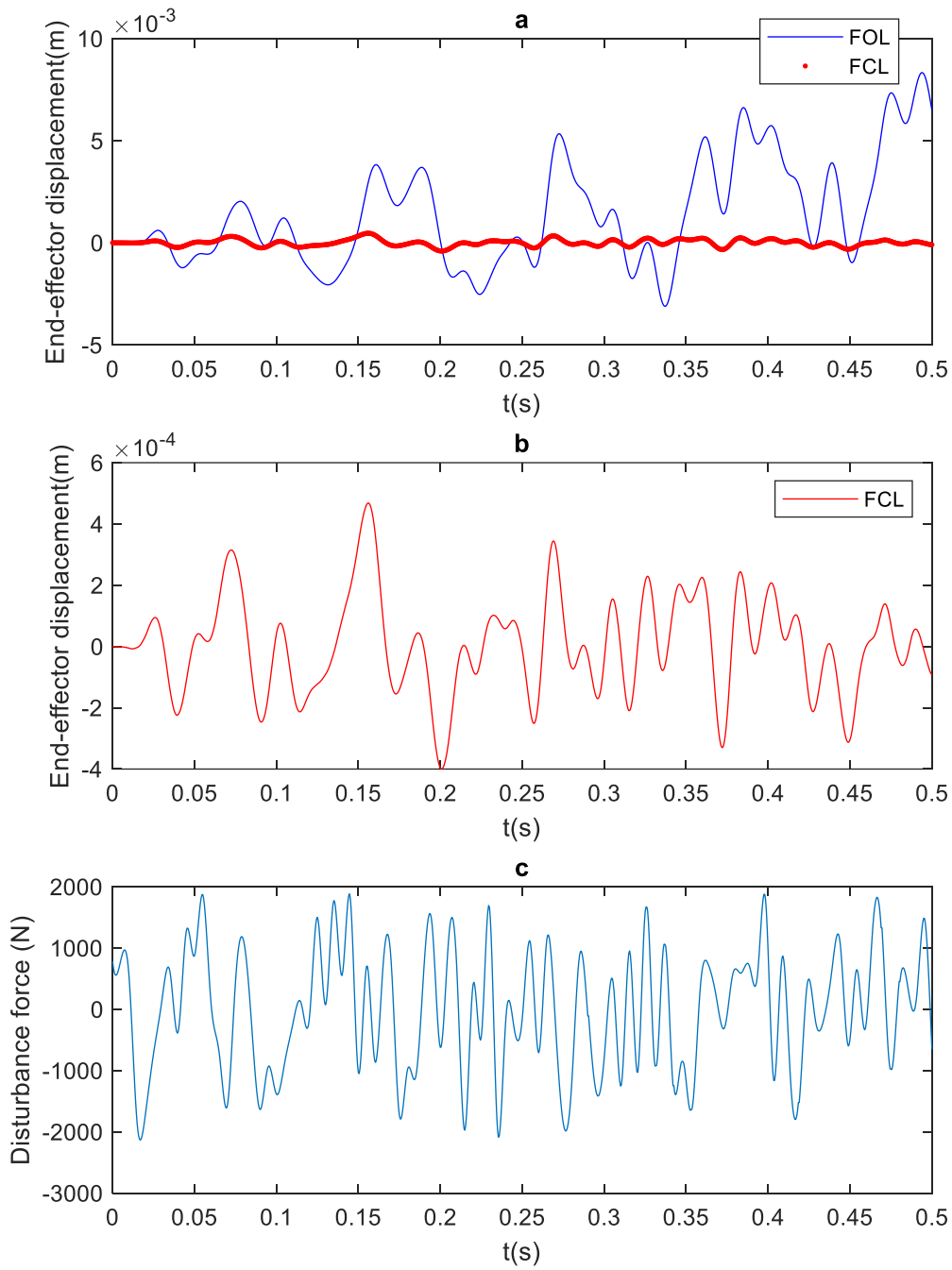


Figure 4.12. 5-DOF manipulator results, (a) tip displacement of the full order open loop and closed loop models (FOL and FCL), (b) zoomed closed loop tip displacement, (c) disturbance as an arbitrary vibration [-2000,2000]N linear force exerted at the base.

Figure 4.13 shows the controller effort, *i.e.*, the amount of moment that is produced by the joints to attenuate the vibration. The controller effort shows how the controller has achieved the desired performance (having no vibration at the EE). In this simulation the 5-DOF manipulator's joints have made an effort within $[-5,5] * 1e5$ Nm. This amount of moment is not achievable by the real stepper motors provided for the 5-DOF manipulator (Chapter 5). The stepper motor datasheet shows that the maximum possible moment is 8 Nm. To address this issue a gear ratio should be installed between the actuator and the corresponding link. The present gear ratio is 1:100 which enables the actuator to have maximum moment of 800 Nm which is not enough to damp such vibration in Figure 4.11 c. The arbitrary vibration provided here was an assumption. For more realistic result to prove whether the actuator is suitable for vibration suppression, the knowledge of terrain pattern is necessary. The focus of this simulation was to design a controller to assure the vibration damping in case of a relatively intense vibration (arbitrary vibration with 100Hz in $[-2,2]$ kN). More simulation could be done to show the feasibility of the actuators, since the H infinity controller can consider the constraints of the actuators.

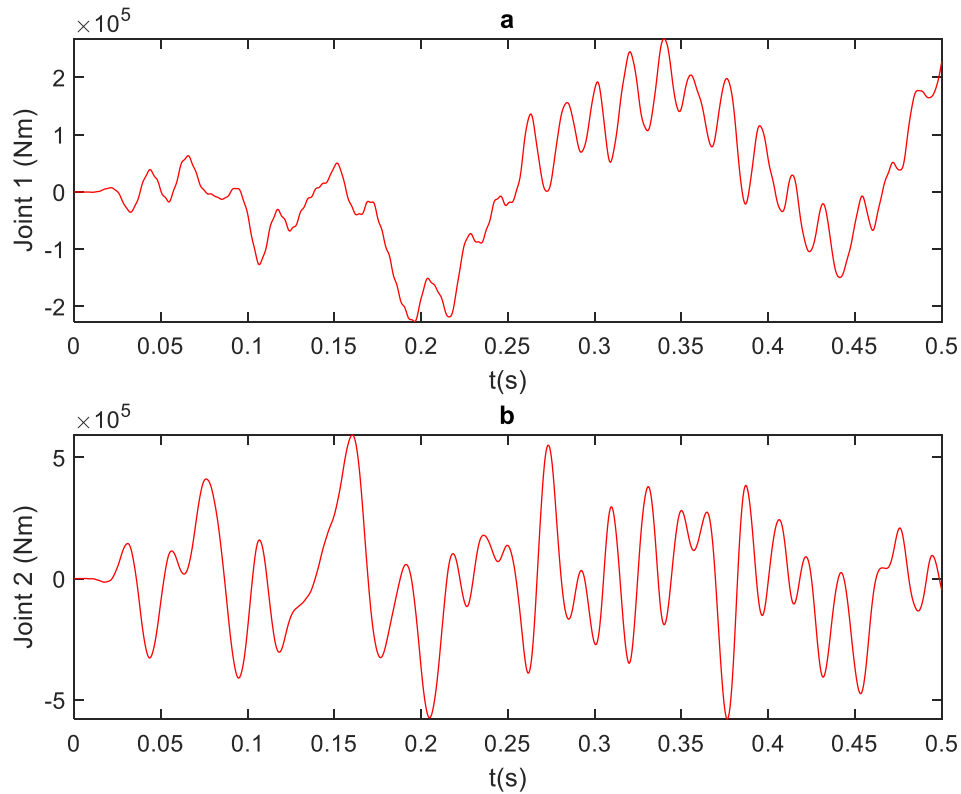


Figure 4.13. 5-DOF manipulator full order model results, (a) joint 1 controller effort, (b) joint 2 controller effort.

Figure 4.14 compares the open loop and closed loop reduced order (BMDC with 5 modes) models in presence of an arbitrary vibration. The red line in (a) shows that the tip of the manipulator fluctuates around the origin when the controller is active which indicates the successful performance of the controller. The target performance of the controller was set to keep the displacement of the tip below 1mm. Plot (b) shows the zoomed closed loop performance which indicates the controller has made the tip vibration reduced to the range of $[-0.4, 0.4]$ mm. Therefore, the tip displacement of the closed loop system has obtained the target performance. Plot (c) is the disturbance time series.

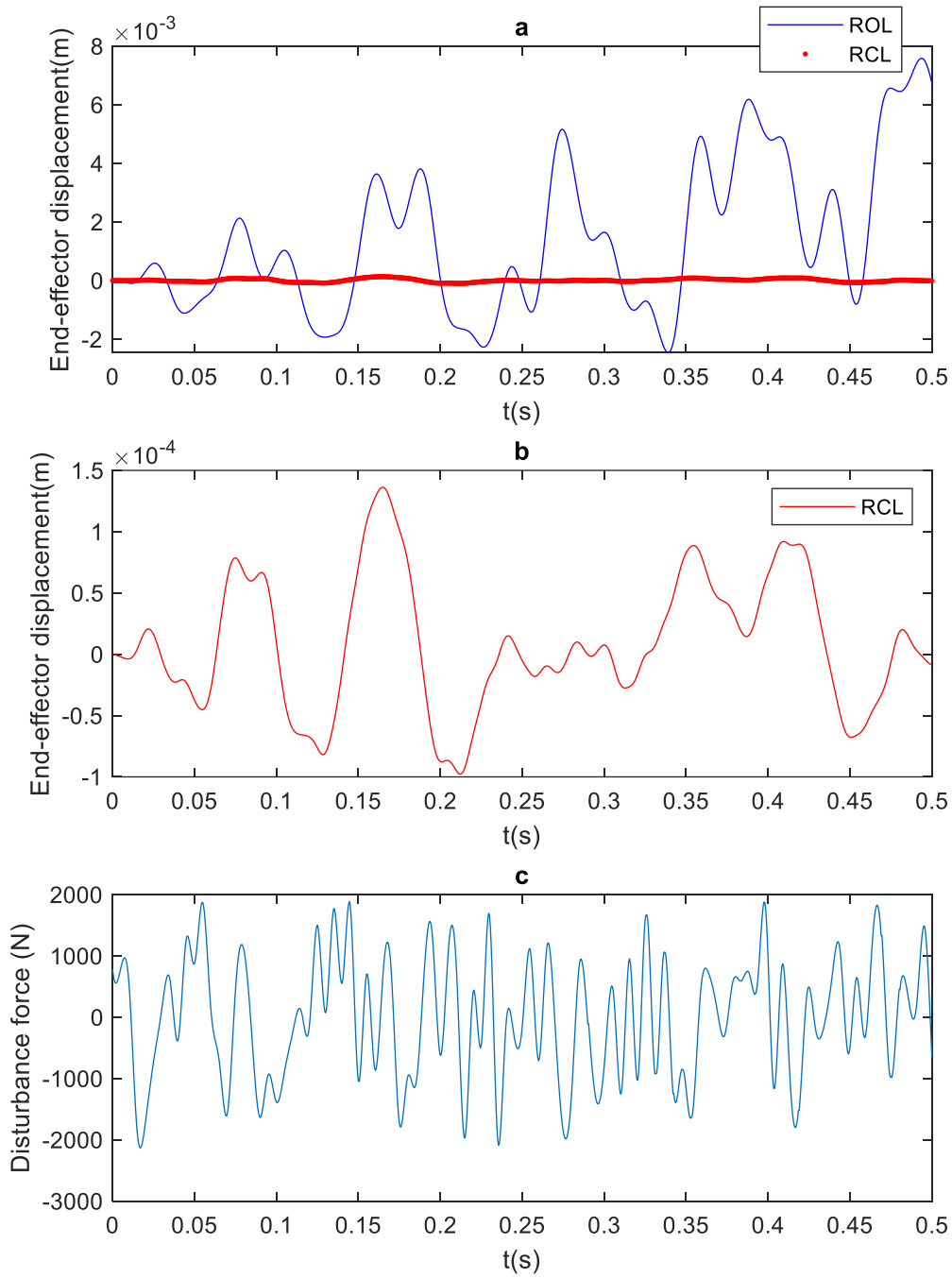


Figure 4.14. 5-DOF manipulator results, (a) tip displacement of the full order open loop and closed loop models (FOL and FCL), (b) zoomed closed loop tip displacement, (c) disturbance as an arbitrary vibration [-2000,2000]N linear force exerted at the base.

Figure 4.15 shows the controller effort, *i.e.*, the amount of moment that is produced by the joints to attenuate the vibration. Comparing Figure 4.14 and 4.12, although the controller requires less effort, it is still not achievable by the stepper motors. This again indicates the need for knowledge of the rough terrain pattern.

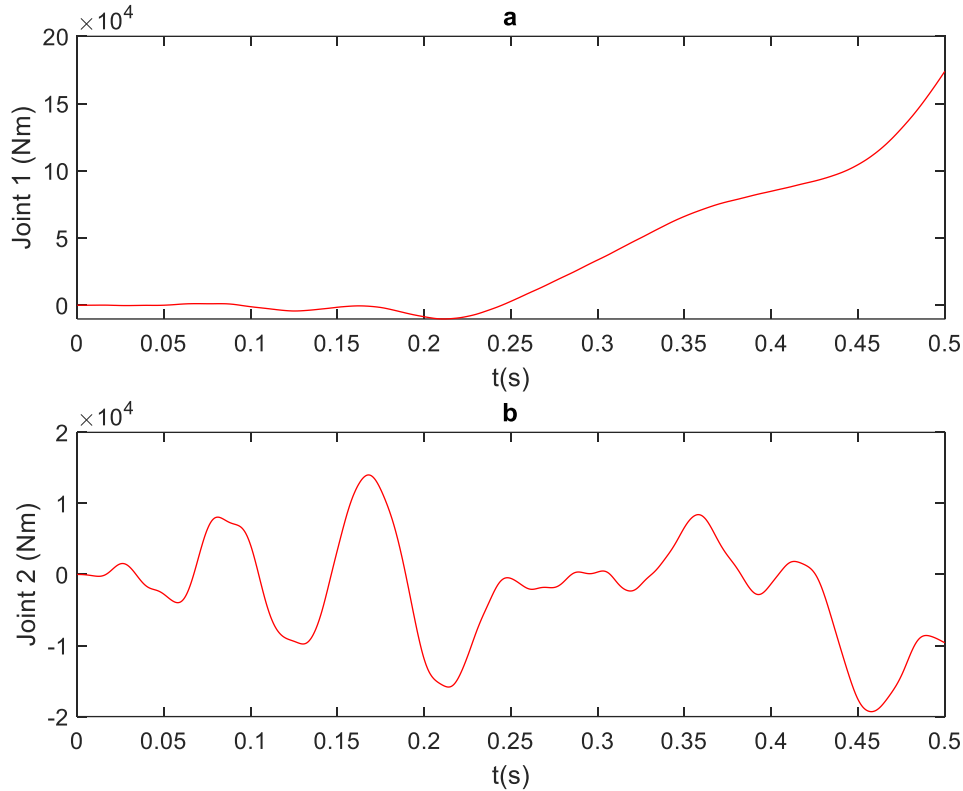


Figure 4.15. 5-DOF manipulator reduced order model results, (a) joint 1 controller effort, (b) joint 2 controller effort.

The 5-DOF model is a MIMO system. Considering equation (4-3), the H_∞ norm for a MIMO system is the largest singular value of the system (open loop or closed loop) across frequencies. The bode diagrams are shown in Figure 4.16; part (a) shows that H_∞ controller has reduced the H_∞ norm of the full order system from infinity to -128dB. Besides, in part (b) the controller has reduced the H_∞ norm of the reduced order system (BMDC with 4 modes) from infinity to -127dB. This infinite value is due to the rigid modes of the manipulator. According to Appendix B, the 5 DOF manipulator has 3 rigid modes: mode 1 is due to the fact that there is no attachment from the

manipulator to the ground, mode 2 and 4 are due to the joints 2 and 3 free rotation. The first mode of the systems is not shown in Figure 4.16 as it has a frequency close to zero Hz.

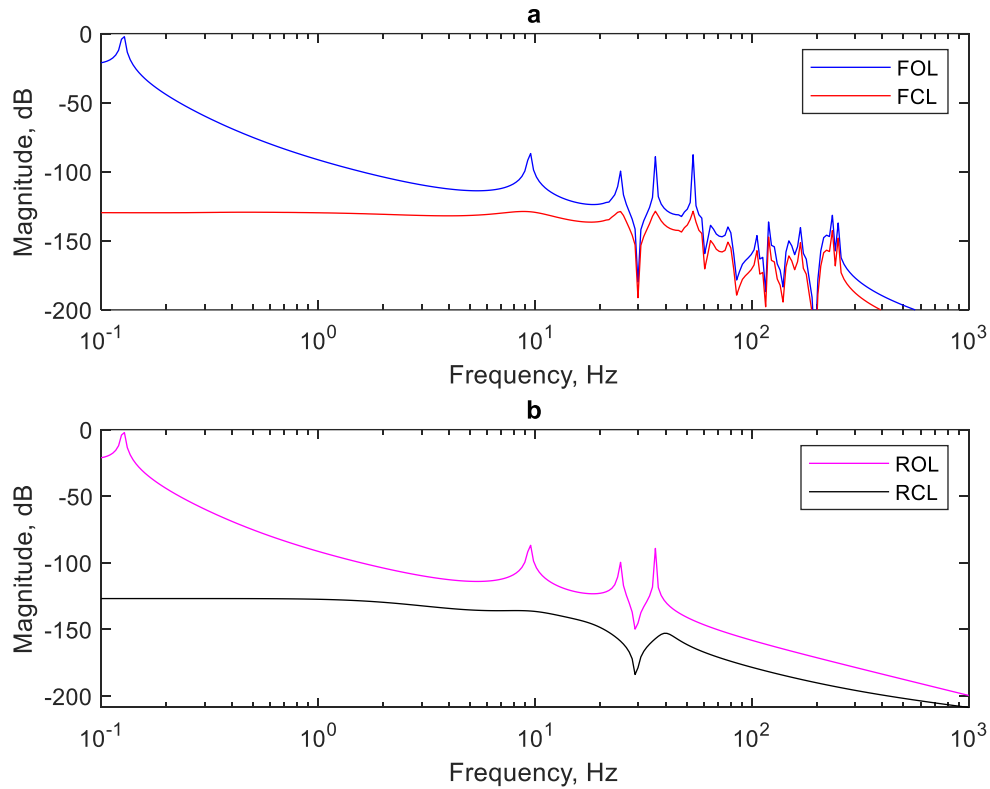


Figure 4.16. Bode diagram of the 5-DOF manipulator, (a) full order open loop and closed loop systems, (b) reduced order closed loop and open loop systems.

The results in this section show the effectiveness of the controller for both reduced and full order models. The reduced model could achieve the same results as the full order model, but the reduced order model has less computational burden on the processor. The results in this section were just simulations that were not verified. The verification would be through practical test on the real 5-DOF manipulator that is beyond the scope of this study.

4.6 Summary

This chapter was about designing the controllers for the manipulators and the effectiveness of the controllers on the vibration attenuation of the manipulators.

For the cantilever beam the LQR controller was designed for the vibration suppression of the full order and BMDC models. These models are in Appendix K. Then, impulse and random vibration (arbitrary vibration) for a SISO control task were simulated.

For the 2L2JM and the 5-DOF manipulator, the H_∞ controller was designed for the vibration suppression of the full order and BMDC models. These models are in Appendix L and M, respectively. Then impulse and random (arbitrary vibration) vibration for a MIMO control task were simulated.

Chapter 5. Implementation of Active Vibration Controller

This chapter is devoted to implementing the designed controller on the real 5-DOF manipulator. Every closed loop system requires a measurement unit which is also called the feedback unit. In addition, every closed loop system has a controller and plant. The plant includes the process system and the actuator. Chapter 3 was about the mathematical model of the process system. Chapter 4 was about the controller. In this chapter the measurement unit and the actuator of the 5-DOF are discussed. The measurement unit for the 5-DOF manipulator is an accelerometer which is used to determine the EE displacement. The actuators for the active vibration suppression are stepper motors to rotate the joints 2 and 3. The closed loop is programmed on a microcontroller such that every iteration starts with the tip displacement measured by the accelerometer. Then the controller uses the measured value to calculate the amount of moment that should be applied to the joints to compensate for the tip displacement. Due to the length of the researcher's study, which took more than 30 months, actual implementation was not accomplished. However, the researcher worked on implementation partially. In this chapter, calibration of the accelerometer for online measurement of the tip displacement, and stepper motors field of operation are reported.

5.1 Tip displacement measurement and verification

In this section, the online displacement measurement and verification are described. The vibrational displacement was produced using a shaker in Room 1B15 of the engineering building. It was measured using an accelerometer connected to an Arduino MEGA 2560, which is a microcontroller. Finally, the measured data was verified using a laser sensor for distance measurement.



Figure 5.1. Equipment for displacement measurement, (left) B&K type 4370 accelerometer, (right) B&K 2635 charging amplifier.

The accelerometer was a B&K type 4370 which was connected to a B&K 2635 charging amplifier. The amplifier was adjusted to 1 mm-1000 mV so that ∓ 5 mm gives a ∓ 5 VDC. Then this voltage was transferred to the Arduino through the analog port A0 (one of the 15 analog ports on the Arduino). However, the Arduino could only receive 0–5 VDC. Therefore, the voltage needed to be mapped so that -5 to +5 VDC converted to 0 to 5 VDC. To do so, the following three-resistor circuit was designed, as shown in Figure 5.2 [42].

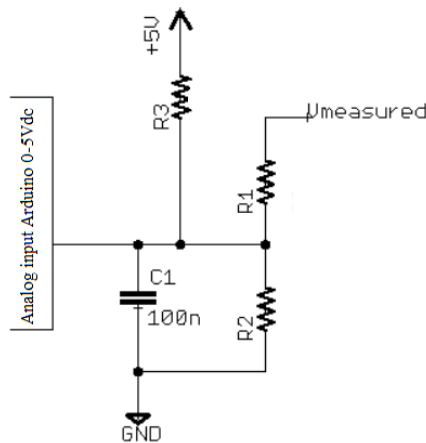


Figure 5.2. The circuit to map the -5 to +5 VDC converts to 0 to 5 VDC [36].

For the safety of the amplifier, $R1 = 50k\Omega$ so that the maximum current drawn would be 0.1 milliamp. Using Kirchoff's Current Law, $R2=3M\Omega$ and $R3=50k\Omega$. The capacitor was for noise attenuation. To verify the displacement measurement using the accelerometer, a laser sensor was used. The laser had been calibrated as 25 mm/V by the lab assistant. This sensor was connected to an oscilloscope to record the voltage.

The experiment was performed for several frequencies of the shaker but only 5 and 10 Hz were recorded by the oscilloscope. The Arduino processor had a 16 MHz clock, but since it wrote the data to the serial port, its recording frequency had fallen to 148 Hz. The oscilloscope captured 50,000 data points for 10 seconds which resulted in 5000 Hz recording frequency. After recording, the data from Arduino and oscilloscope were filtered using an FIR filter to remove the noise. The FIR filter used in here was a multiband filter to let the frequency around 5 and 10 Hz pass. This was achieved by the command “fir1” in M-software. More information about the FIR filter is in [43].

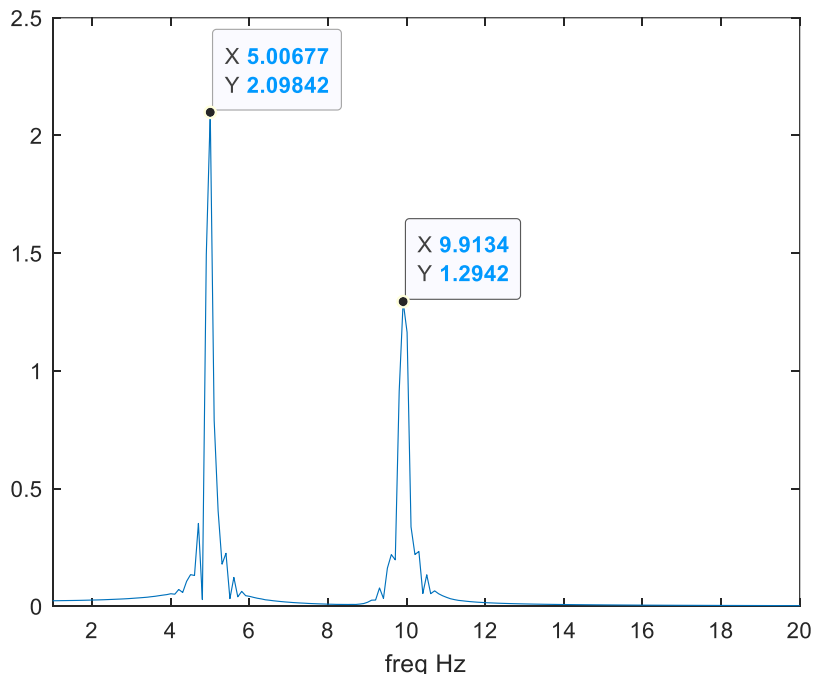


Figure 5.3. Fast Fourier transform of the Accelerometer output, when stimulated at 5 and 10 Hz.

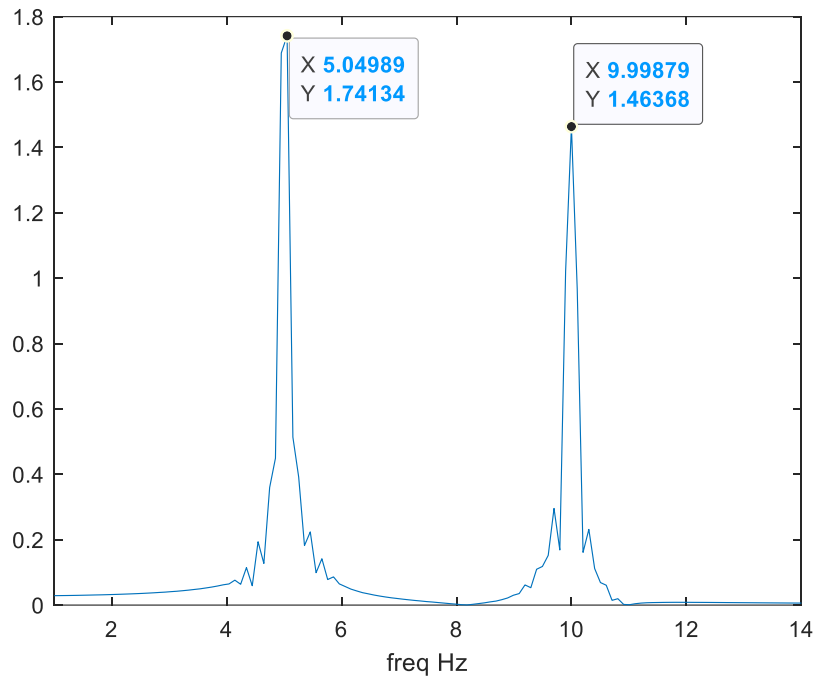


Figure 5.4. Fast Fourier transform of the Laser output, when stimulated at 5 and 10 Hz.

Figure 5.3 and Figure 5.4 show fast Fourier transform (FFT) of the sensors output when they were stimulated at 5 and 10 Hz frequencies. The purpose of these figures was to show whether the laser sensor and the accelerometer connected to the Arduino could record the excitation frequency {5,10} Hz accurately. Looking at the x coordinate of the indicated points in the figures, one could conclude that the sensors were able to record these two excitation frequencies; thus, they were well calibrated.

The laser sensor is an accurate device to measure the displacement; however, it measures the offline data. On the other hand, the accelerometer connected to the Arduino was meant to measure online (real-time) displacement. If the Figure 5.5 shows that the accelerometer has tracked the laser, one could conclude the accuracy of the accelerometer for online measurement. In other words, Figure 5.5, illustrates the reliability of the accelerometer.

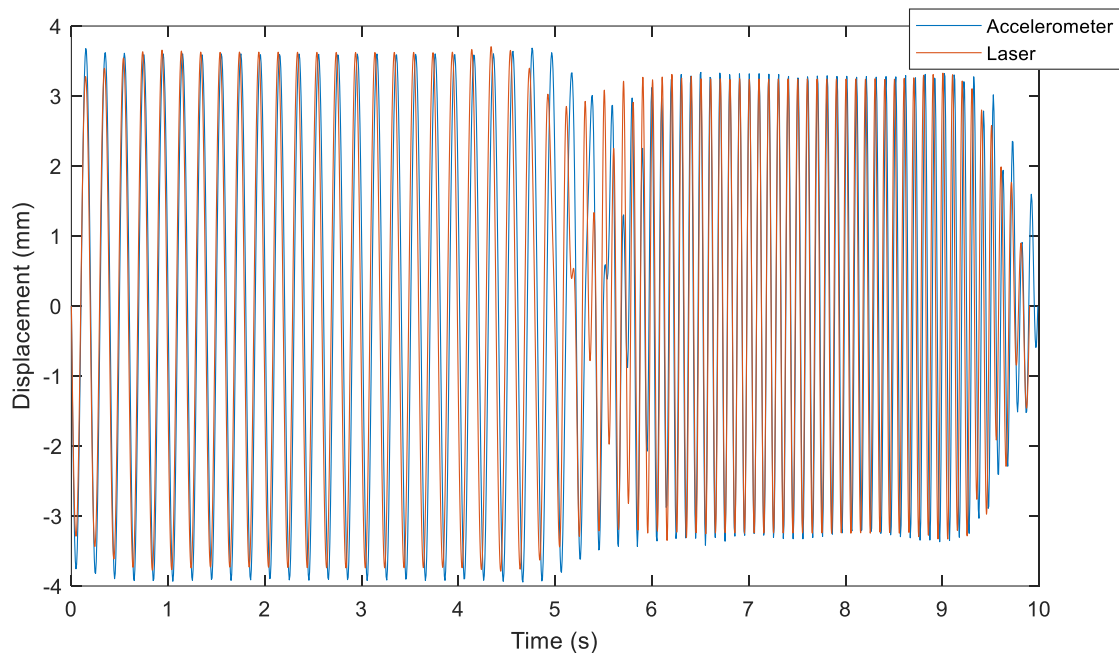


Figure 5.5. Shaker displacement measured by the accelerometer and Laser sensors.

According to Figure 5.5 the accelerometer has tracked the laser displacement measurement. The Difference index was defined based on the equation (3-47) by substituting the absolute sensor measurement instead of *variable*. The RMS for the Accelerometer was 2.4498, whereas that of the Laser was 2.3787 which was 2.98% difference. Thus, it verifies that the accelerometer has measured the displacement accurately in real-time operation. To interpret the data captured by the accelerometer, the serial monitor records the timeseries of the displacement with a constant but unknown interval. Finding this interval results in the recording frequency. Using trial and error this frequency was around 148 Hz. Therefore, the phase difference between the red and blue plots in the figure is due to the inaccuracy in finding this frequency.

5.2 Stepper motor field of operation experiment

Joints 2 and 3 of the 5-DOF manipulator have been equipped with MST342C02 stepper motors and SMD42C2 drives. The driver was set to 10 mini-steps/full-steps. These motors have been connected to the joints through a gear box with the gear ratio of 100:1. The stepper motors were

energized with a converter that provide 48 VDC and 10 amp. The micro controller was an Arduino MEGA 2560.

Accelstepper is a sophisticated library written for Arduino which makes the stepper motor move at the desired speed and acceleration. Using the Arduino code, the motor can produce a specific amount of torque at a certain speed. This value is parametrized with PWM (Pulse Width Modulation) that divides the maximum torque available to an integer between 0-255. This value is translated as voltage to the “moving current” pin of the driver. Using Arduino that has a 16 MHz processor, the stepper motor could move up to 1 rev/s. However, by changing the microcontroller to Teensy 4.1 (a faster microcontroller), the stepper motor could reach over 40 rev/s. This microcontroller has the clock speed of 600 MHz, but it could operate at 1GHz with a cooling system. It is noteworthy that there is another pin called “standby current” on the driver. This pin also works with PWM and determines the amount of holding torque (the torque to holds the stepper motor’s shaft immobilized against the external torque).

Given the weight of the arm, which is 70kg, in the fully extended configuration, the motors should provide 900Nm to hold the arm in a stationary position. This is achievable thanks to a holding torque of 9Nm (multiplied by the 100 for the gear ratio). However, for vibration suppression the situation differs. The relationship between the rotational velocity of the motor and the speed of the tip is as follows:

$$\omega_{link} = \omega_{motor} * N_{gear} \quad 5-1$$

$$V_{tip} = \omega_{link} * L_{link}$$

where ω_{link} , and ω_{motor} are the rotational velocity of the link and motor, respectively. N_{gear} and L_{link} are the gear ratio and approximate length of the manipulator, respectively. Considering the gear ratio of 1:100, and 3m for the length of the manipulator, if the tip requires to move at a speed of 1 m/s, the motor needs to move 33 rad/s or around 300 RPM.

At this speed, the motor torque drops significantly. According to the stepper motor torque-velocity profile provided by the company in Figure 5.6 [44], the green line corresponds to the 5-

DOF motor and driver and the three other graphs are not related to this research. This figure gives a little information about the dynamic performance of the motor. In other words, this figure has no detail on the acceleration of the motor, and it assumes that the motor operates at constant speed. However, the 5-DOF manipulator requires that different accelerations, speeds and torques be provided at different instances to suppress the vibration of the EE.

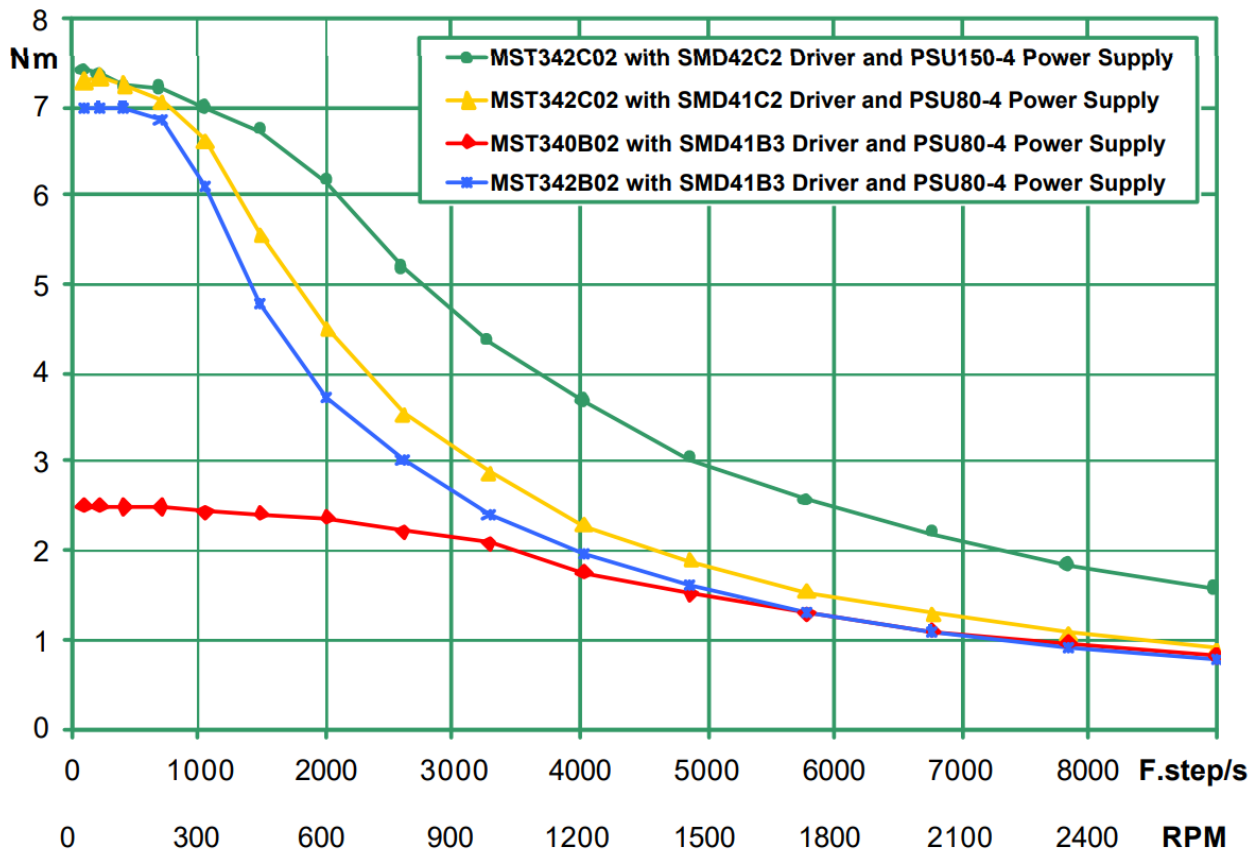


Figure 5.6. Torque-velocity profile from stepper motor datasheet [44].

Therefore, to specify the exact amount of torque produced by the motor at different speeds and accelerations, a dynamic torque measurement is necessary. To measure the dynamic torque of the motor, one way is to attach the shaft to an electric brake. The setup for dynamic torque measurement is shown in Figure 5.7. The brake is magnetic particle CLUTCH KC-2.5 which gives a brake torque between 0.3-20 Nm by adjusting the current between 0-1.3 amps. The motor shaft diameter is 14 mm and that of the brake is 20 mm. Therefore, flexible shaft couplings connect the motor and brake shafts together. The coupling is made up of Iron Hubs and Buna-N Rubber Spider.

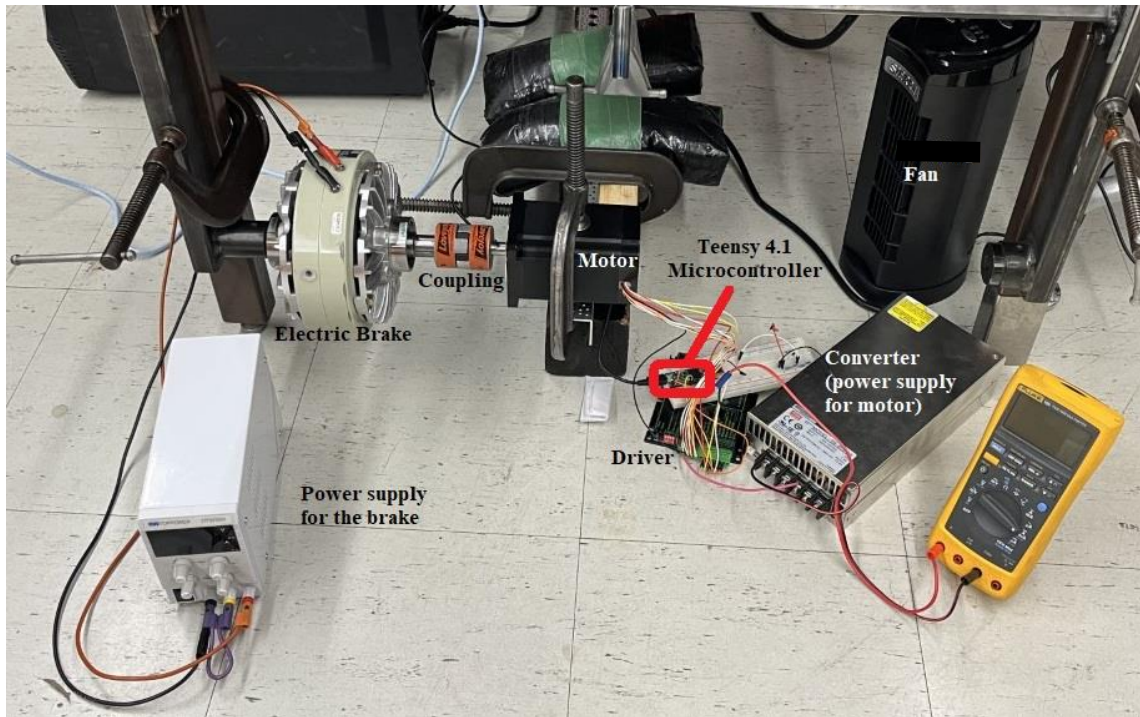


Figure 5.7. Torque measurement setup for stepper motor field of operation experiment.

During the test it was noted that:

1. The driver chose the optimal torque for each certain speed. Therefore, there was no need to use PWM for adjusting the torque.
2. To avoid weak performance, a cooling fan was needed for both motor and brake.
3. The motor could operate at higher speeds with relatively low acceleration; however, increasing the acceleration results in motor stall for high speeds.

To find the motor's torque vs. speed, two sets of tests were established. Each test was performed several times to ensure the recorded value. The purpose of the first test was to establish a look-up table to give the maximum amount of the motor torque as a function of speed and acceleration. The approach taken was changing the motor speed from zero to a certain speed with a constant acceleration and bringing back the speed to zero with the same negative acceleration value. During the test, an electric damper applied a constant load to the motor. The measured values of torque are shown in Table 5.1. In this test, the measured torque for a certain velocity and acceleration was measured many times to ensure that the motor would never stall.

Table 5.1. Torque (Nm) measured based on specific acceleration and speed of the motor (test1).

		Acceleration (rev/s ²)						
		5.0	10	15	20	25	30	35
Speed (rev/s)	0.5	7.00	6.83	6.67	6.50	6.33	6.17	6.00
	1.0	6.71	6.55	6.38	6.21	6.05	5.88	5.71
	1.5	6.43	6.26	6.10	5.93	5.76	5.60	5.43
	2.0	6.14	5.98	5.81	5.64	5.48	5.31	5.14
	2.5	5.86	5.69	5.52	5.36	5.19	5.02	4.86
	3.0	5.57	5.40	5.24	5.07	4.90	4.74	4.57
	3.5	5.29	5.12	4.95	4.79	4.62	4.45	4.29
	4.0	5.00	4.83	4.67	4.50	4.33	4.17	4.00
	4.5	4.83	4.67	4.50	4.33	4.17	4.00	3.83
	5.0	4.67	4.50	4.33	4.17	4.00	3.83	3.67
	5.5	4.50	4.33	4.17	4.00	3.83	3.67	3.50
	6.0	4.00	3.83	3.67	3.50	3.33	3.17	3.00
	6.5	3.50	3.33	3.17	3.00	2.83	2.67	2.50
	7.0	3.25	3.08	2.92	2.75	2.58	2.42	2.25
	7.5	3.00	2.83	2.67	2.50	2.33	2.17	2.00
	8.0	2.80	2.63	2.47	2.30	2.13	1.97	1.80
	8.5	2.60	2.43	2.27	2.10	1.93	1.77	1.60
9.0	2.40	2.23	2.07	1.90	1.73	1.57	1.40	
9.5	2.20	2.03	1.87	1.70	1.53	1.37	1.20	
10.0	2.00	1.83	1.67	1.50	1.33	1.17	1.00	

Table 5.1 shows a look-up table, which represents dynamic torque values. In other words, this table represents a maximum amount of torque generated by the motor at a certain speed and acceleration of the motor. The designed controller in the previous chapter takes advantage of this table. Given the required controller torques used in Chapter 4, the library (look-up table above) uses the corresponding speed and acceleration to reach the required motor torque.

The second test results were represented in Table 5.2. The purpose of this test was to obtain a relationship between the torque and current so that the required torque can be achieved by the

supplied current. Since the stepper motor is a synchronous electric motor, it has a torque constant which is as follows [40]:

$$\text{torque constant} = \frac{\text{Motor torque}}{\text{supply current}} \quad 5-2$$

However, this relationship is not accurate for stepper motors used in the 5-DOF manipulator. To find actual relationship between the torque and current, a second test was established. This test was performed by constant speed values. The procedure was as follows: while the motor was running at a certain speed the load was increased until the motor stalled. Then the current at the last moment was recorded.

Table 5.2. Max torque of the motor and the current at a certain speed (test 2).

Speed (rev/s)	0.5	1.0	1.5	2.0	2.5	3.0	3.5	4.0	4.5	5.0
Max Brake Torque (Nm)	8.0	8.0	8.0	8.0	8.0	8.0	7.8	7.2	7.0	6.2
Current (amps)	2.5	3.2	3.8	4.7	5.2	5.8	6.0	6.0	6.0	6.0
Torque/current	3.2	2.5	2.1	1.7	1.5	1.4	1.3	1.2	1.2	1.0
Speed (rev/s)	5.5	6.0	6.5	7.0	7.5	8.0	8.5	9.0	9.5	10.0
Max Brake Torque (Nm)	5.8	5.7	5.0	4.9	4.3	4.0	3.8	3.5	3.4	3.3
Current (amps)	5.8	6.0	6.0	6.0	5.8	6.0	5.8	5.8	5.9	5.9
Torque/current	1.0	0.9	0.8	0.8	0.7	0.7	0.7	0.6	0.6	0.6

Table 5.2 represents relationship between the motor's torque and its supplied current at a certain motor speed. This table shows that the torque constant value for the motor changes as the speed changes.

After establishing the input and output of the closed loop system for the vibration suppression of the 5-DOF manipulator, the designed controllers needed to be programmed on the micro-controller with a communication with the I/O. However, the closed loop implementation was beyond the scope of this study.

5.3 Summary

In this chapter the tip measurement unit was calibrated for online displacement measurement. It was also verified using an accurate laser sensor. In the second part of this chapter the actuators' stepper motor was tested. The test was intended to find a look up table for the stepper motor field of operation. This table showed the torque as a variable of the speed and acceleration of the motor. This test did not verify the graph provided by the company as it did not have any information regarding acceleration. In another test it was shown that the stepper motor's torque does not have a linear relationship with the current.

Chapter 6. Conclusion and Future Work

6.1 Conclusions

The 5-DOF manipulator is a flexible structure which was designed to be installed on a mobile base to monitor crops in farm fields. When the manipulator which is installed on a mobile base move along the farm field, the manipulator (especially its EE) undergoes vibration which may result in inaccurate data collection. Objectives for this thesis were vibration evaluation of the manipulator, controlling vibration of the manipulator, and trying to implement the controllers on the manipulator. Chapter 2 covered vibration evaluation of the manipulator. Modal parameters of the manipulator were obtained, and the force vibration transmitted to the EE of the manipulator was obtained. In Chapter 3 using manual FEM, the equation of motion for a cantilever beam and a 2L2JM were derived. The eigenvectors obtained from FEA-A were used to build full order and reduced order state-space models of the cantilever beam, 2L2JM and the 5-DOF manipulator. These models were verified with FEA-A. In Chapter 4, the state-space models from chapter 3 were used by the employed controllers. For the cantilever beam a LQR controller was used, which for the 2L2JM and the 5-DOF manipulator a H_∞ controller was employed. In Chapter 6, a real-time unit for measuring displacement of the EE was calibrated. In addition, a look-up table was developed to give the joint torque as a function of speed and acceleration of the motors.

The focus of this thesis was obtaining and verifying the model of the 5-DOF flexible manipulator which led to designing an active vibration controller for its end-effector. The 5-DOF manipulator has a complex structure, and its modeling is useful for other similar structures. This modeling was verified with FEA-A with a small error. Moreover, the model is proposed for online controlling. The modeling approach reduced the size of matrices from a very large order (about 100,000) to a small order (about 10). The reduced model was verified by FEA-A to show the accuracy of behavior of the reduced system. The controller was both optimal and robust. The controllers employed can be used for achieving several targets, such as disturbance rejection and optimal performance. The controller caused the H_∞ norm of an unstable system with an initial value of infinity be reduced -128 dB. For the closed loop system the feedback and actuator units were established.

6.2 Future work

The research project was limited by the master's period of study, however there are future tasks to be done.

1. The designed controllers are needed to be programmed on the microcontroller. This program should be developed to allow communication between the controller, accelerometer, and the stepper motors. The first step is making an Arduino program with a numerical integrator to calculate the states from given measured displacement. Then it would use the designed closed loop matrices to calculate the desired actuator torque at each iteration. The second step is to make a serial communication between the real time measurement unit, which is the accelerometer, and the integrator and the actuator. The open loop system that has already been implemented on the real system has 1s delay. This amount was set by another lab member to ensure that the serial communication was available between the computer, microcontroller and the motors. However, this amount is not optimal and can be considered excessive for the fast response of active vibration suppression system. Therefore, the optimal time-delays should be compatible with different response rates of the units and provide the fast response for the entire active vibration suppression system. The possible solution to find the optimal time delays, would be through trial and error. In other words, the implemented program should be tested under different frequencies and amplitudes of base excitation with suitable time-delays. To make sure the corresponding time-delay is enough and fast to provide proper response for each frequency and amplitude. This results in the third step which is tuning the controller.
2. The model reduction effectiveness should be shown in a real-time control system. Therefore, a comparison could be made between the performance of the controllers that run with the full order model compared to the reduced order models. This task needs the full implementation of the closed loop on the 5-DOF manipulator. Then the performance of the full order and reduced order closed loops could be compared.
3. Also, there is a need to define additional control targets for the H_∞ controller. As a robust controller, it can deal with uncertainties apart from the disturbance that is transmitted to the

manipulator. Moreover, some other control targets could be defined, such as accelerometer noise rejection, and actuator optimum performance. The controller can compromise between these targets.

4. The passive vibration attenuation could be applied to the arm. There are some adhesive tapes which provide the links with extra damping. Then, the passive and active vibration controls could be compared.

References

- [1] M. Khak Pour, “Improvement of a mobile platform for plant phenotyping.” University of Saskatchewan, 2020.
- [2] M. Burnette *et al.*, “TERRA-REF data processing infrastructure,” in *Proceedings of the Practice and Experience on Advanced Research Computing*, 2018, pp. 1–7.
- [3] A. S. Phung, J. Malzahn, F. Hoffmann, and T. Bertram, “Data based kinematic model of a multi-flexible-link robot arm for varying payloads,” in *2011 IEEE International Conference on Robotics and Biomimetics*, 2011, pp. 1255–1260.
- [4] J. Malzahn, “Modeling and control of multi-elastic-link robots under gravity: from oscillation damping and position control to physical interaction.” Dissertation, Dortmund, Technische Universität, 2014, 2014.
- [5] W. Njeri, M. Sasaki, and K. Matsushita, “Gain tuning for high-speed vibration control of a multilink flexible manipulator using artificial neural network,” *J. Vib. Acoust.*, vol. 141, no. 4, 2019.
- [6] T. Meng and W. He, “ILC for a Flexible Single-Link Manipulator,” in *Iterative Learning Control for Flexible Structures*, Springer, 2020, pp. 109–128.
- [7] T. Meng and W. He, “Iterative learning control of a robotic arm experiment platform with input constraint,” *IEEE Trans. Ind. Electron.*, vol. 65, no. 1, pp. 664–672, 2017.
- [8] A. Jamali, I. Z. Mat Darus, P. P. Mohd Samin, and M. O. Tokhi, “Intelligent modeling of double link flexible robotic manipulator using artificial neural network,” *J. Vibroengineering*, vol. 20, no. 2, pp. 1021–1034, 2018.
- [9] A. Jamali, I. Z. M. Darus, M. O. Tokhi, and A. S. Z. Abidin, “Utilizing P-type ILA in tuning hybrid PID controller for double link flexible robotic manipulator,” in *2018 2nd International Conference on Smart Sensors and Application (ICSSA)*, 2018, pp. 141–146.
- [10] M. Benosman, “Model-based vs data-driven adaptive control: an overview,” *Int. J. Adapt. Control Signal Process.*, vol. 32, no. 5, pp. 753–776, 2018.
- [11] E. Pereira, S. S. Aphale, V. Feliu, and S. O. R. Moheimani, “Integral resonant control for

- vibration damping and precise tip-positioning of a single-link flexible manipulator,” *IEEE/ASME Trans. Mechatronics*, vol. 16, no. 2, pp. 232–240, 2010.
- [12] L. Qingsheng and L. Xiang, “Research of the active vibration suppression of flexible manipulator with one degree-of-freedom,” in *International Conference on Intelligent Robotics and Applications*, 2017, pp. 624–636.
- [13] R. Fareh, “Sliding mode fractional order control for a single flexible link manipulator,” *Int. J. Mech. Eng. Rob. Res.*, vol. 8, no. 2, 2019.
- [14] M. P. P. Reddy and J. Jacob, “Vibration control of flexible link manipulator using SDRE controller and Kalman filtering,” *Stud. Inform. Control*, vol. 26, no. 2, pp. 143–150, 2017.
- [15] Z. Qiu, J. Han, and J. Liu, “Experiments on fuzzy sliding mode variable structure control for vibration suppression of a rotating flexible beam,” *J. Vib. Control*, vol. 21, no. 2, pp. 343–358, 2015.
- [16] T. Nestorović, N. Durrani, and M. Trajkov, “Experimental model identification and vibration control of a smart cantilever beam using piezoelectric actuators and sensors,” *J. Electroceramics*, vol. 29, no. 1, pp. 42–55, 2012.
- [17] X. Shen, Y. Dai, M. Chen, L. Zhang, and L. Yu, “Active vibration control of the sting used in wind tunnel: comparison of three control algorithms,” *Shock Vib.*, vol. 2018, 2018.
- [18] R. J. Theodore and A. Ghosal, “Comparison of the assumed modes and finite element models for flexible multilink manipulators,” *Int. J. Rob. Res.*, vol. 14, no. 2, pp. 91–111, 1995.
- [19] H. Karagülle, L. Malgaca, M. Dirilmiş, M. Akdağ, and Ş. Yavuz, “Vibration control of a two-link flexible manipulator,” *J. Vib. Control*, vol. 23, no. 12, pp. 2023–2034, 2017.
- [20] R. Dubay, M. Hassan, C. Li, and M. Charest, “Finite element based model predictive control for active vibration suppression of a one-link flexible manipulator,” *ISA Trans.*, vol. 53, no. 5, pp. 1609–1619, 2014.
- [21] M. Shao, Y. Huang, and V. V Silberschmidt, “Intelligent manipulator with flexible link and joint: modeling and vibration control,” *Shock Vib.*, vol. 2020, 2020.

- [22] S. M. Khot and Y. Khan, "Simulation of active vibration control of a cantilever beam using LQR, LQG and $H-\infty$ optimal controllers," *J Vibr Anal Meas Control*, vol. 3, no. 2, pp. 134–151, 2015.
- [23] A. A. Ali, R. A. R. Lateef, and M. W. Saeed, "Intelligent tuning of vibration mitigation process for single link manipulator using fuzzy logic," *Eng. Sci. Technol. an Int. J.*, vol. 20, no. 4, pp. 1233–1241, 2017.
- [24] M. A. Kamel, K. Ibrahim, and A. E.-M. Ahmed, "Vibration control of smart cantilever beam using finite element method," *Alexandria Eng. J.*, vol. 58, no. 2, pp. 591–601, 2019.
- [25] A. Ebrahimi-Tirtashi, S. Mohajerin, M. R. Zakerzadeh, and M. A. Nojoomian, "Vibration control of a piezoelectric cantilever smart beam by $\mathcal{L}1$ adaptive control system," *Syst. Sci. Control Eng.*, vol. 9, no. 1, pp. 542–555, 2021.
- [26] M. R. Hatch, *Vibration simulation using MATLAB and ANSYS*. CRC press, 2000.
- [27] H. Badkoobehhezaveh, "Control and Vibration of a 5-DOF Long-reach Robotic Arm." University of Saskatchewan, 2022.
- [28] S. R. Singiresu, *Mechanical vibrations*. Addison Wesley Boston, MA, 1995.
- [29] T. J. R. Hughes, *The finite element method: linear static and dynamic finite element analysis*. Courier Corporation, 2012.
- [30] R. S. Li, "A methodology for fatigue prediction of electronic components under random vibration load," *J. Electron. Packag.*, vol. 123, no. 4, pp. 394–400, 2001.
- [31] Y. Zhu, J. Qiu, and J. Tani, "Simultaneous optimization of a two-link flexible robot arm," *J. Robot. Syst.*, vol. 18, no. 1, pp. 29–38, 2001.
- [32] H. Wang, Y. Xing, Y. Li, and Z. Li, "Dynamic modeling of five-bar manipulator with structurally flexible linkages," in *2010 8th World Congress on Intelligent Control and Automation*, 2010, pp. 5774–5779.
- [33] V. Adams and A. Askenazi, *Building better products with finite element analysis*. Cengage Learning, 1999.
- [34] J. M. A. Scherpen, "Balanced Realizations, Model Order Reduction, and the Hankel

- Operator,” in *The Control Handbook. Control System Advanced Methods*, 2011, pp. 1–4.
- [35] S. L. Brunton and J. N. Kutz, *Data-driven science and engineering: Machine learning, dynamical systems, and control*. Cambridge University Press, 2022.
- [36] Y. Reddy and S. Hur, “Comparison of Optimal Control Designs for a 5 MW Wind Turbine,” *Appl. Sci.*, vol. 11, no. 18, p. 8774, 2021.
- [37] K. Tsakalis, “Stability/Controllability/Observability”, [Online]. Available: <https://tsakalis.faculty.asu.edu/notes/sco.pdf>
- [38] K. J. Åström and B. Wittenmark, *Computer-controlled systems: theory and design*. Courier Corporation, 2013.
- [39] W. K. Gawronski, *Dynamics and control of structures: A modal approach*. Springer Science & Business Media, 2004.
- [40] N. S. Nise, *Control systems engineering*. John Wiley & Sons, 2020.
- [41] D.-W. Gu, P. Petkov, and M. M. Konstantinov, *Robust control design with MATLAB®*. Springer Science & Business Media, 2005.
- [42] J. Westhues, “Measure a DC Voltage Between -15 V and 15 V.” <https://cq.cx/interface.pl#6> (accessed Aug. 14, 2022).
- [43] V. K. Ingle and J. G. Proakis, *Digital signal processing using matlab: a problem solving companion*. Cengage Learning, 2016.
- [44] JVL, “High Quality, High Torque Step Motors MST340, 341 and 342,” *LD0042-06GB datasheet*, 2008. https://www.jvl.dk/files/_2011clean/pdf/ld042gb.pdf
- [45] C. Tirupathi R and B. Ashok D, “Introduction to finite elements in engineering.” 2016.
- [46] A. G. De Souza and L. C. G. De Souza, “H infinity controller design to a rigid-flexible satellite with two vibration modes,” in *Journal of Physics: Conference Series*, 2015, vol. 641, no. 1, p. 12030.

Appendixes

A. The 5-DOF manipulator modal analysis, section 2.1 (fixed base and joints)

The mode shapes in this part are from modal analysis of the 5-DOF manipulator with fixed base and fixed joints. Therefore, all the modes are oscillatory. Below are the 10 mode shapes of the manipulator, Figures A.2 to A.11.

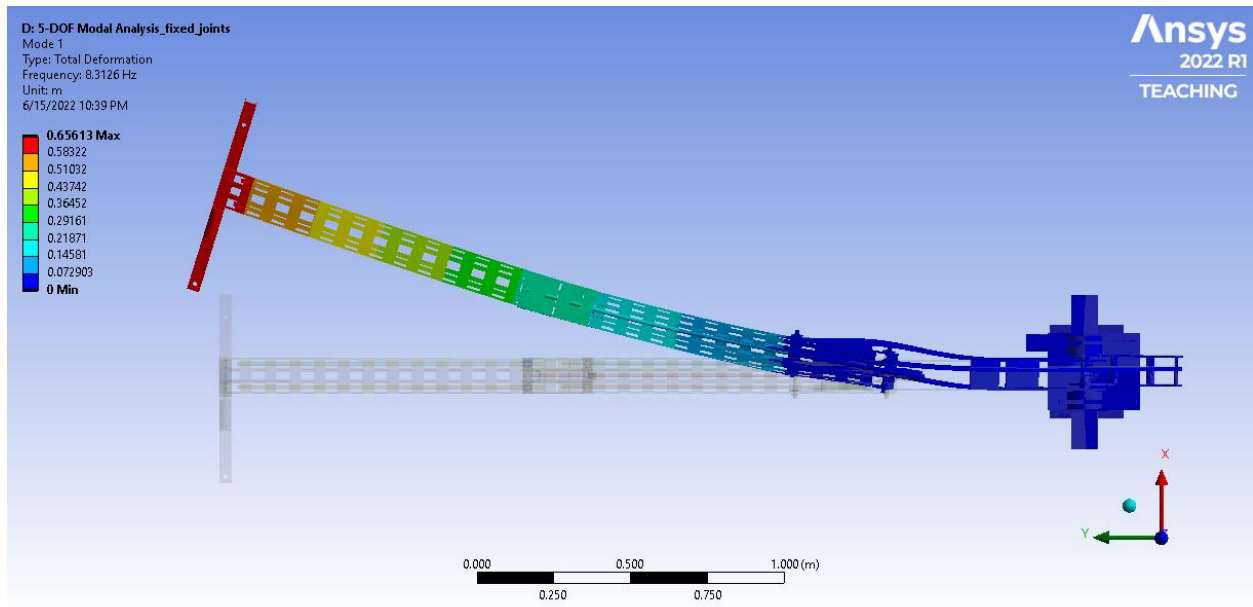


Figure A.1. First mode of the 5-DOF manipulator with fixed base and joints (1st lateral)

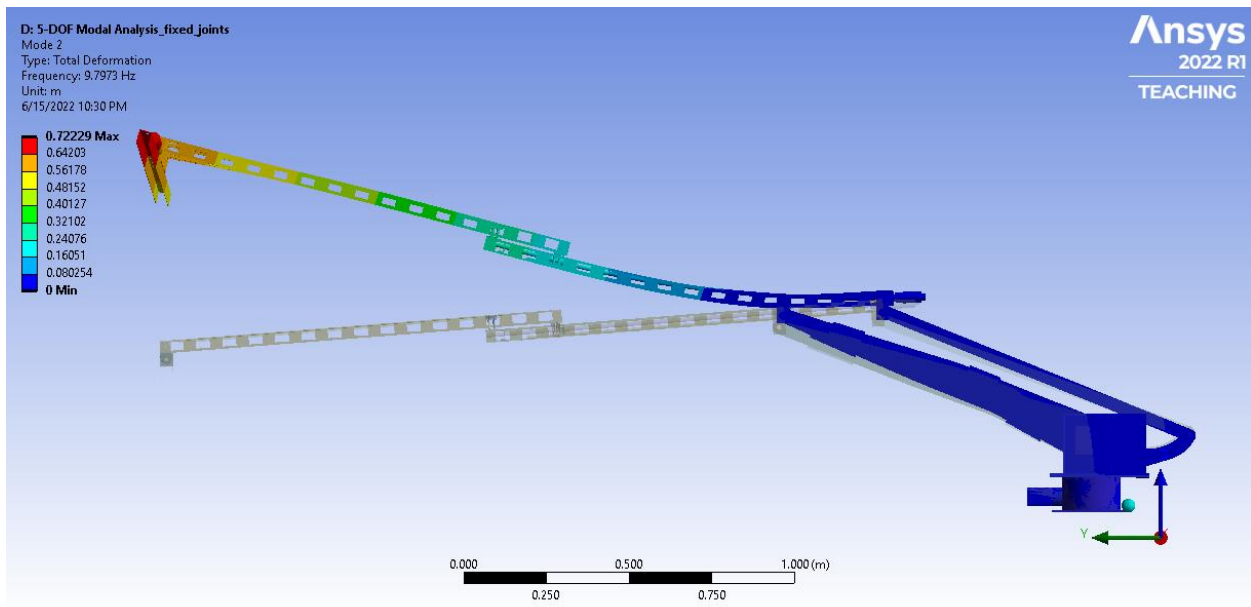


Figure A.2. Second mode of the 5-DOF manipulator with fixed base and joints (1st vertical)

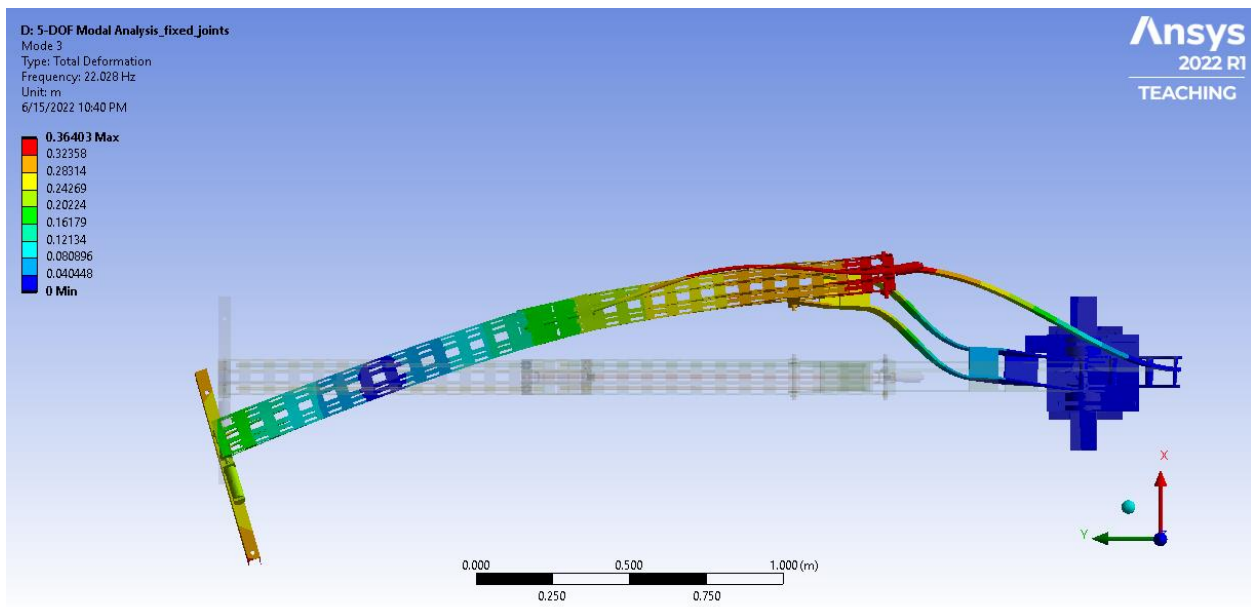


Figure A.3. Third mode of the 5-DOF manipulator with fixed base and joints (2nd lateral)

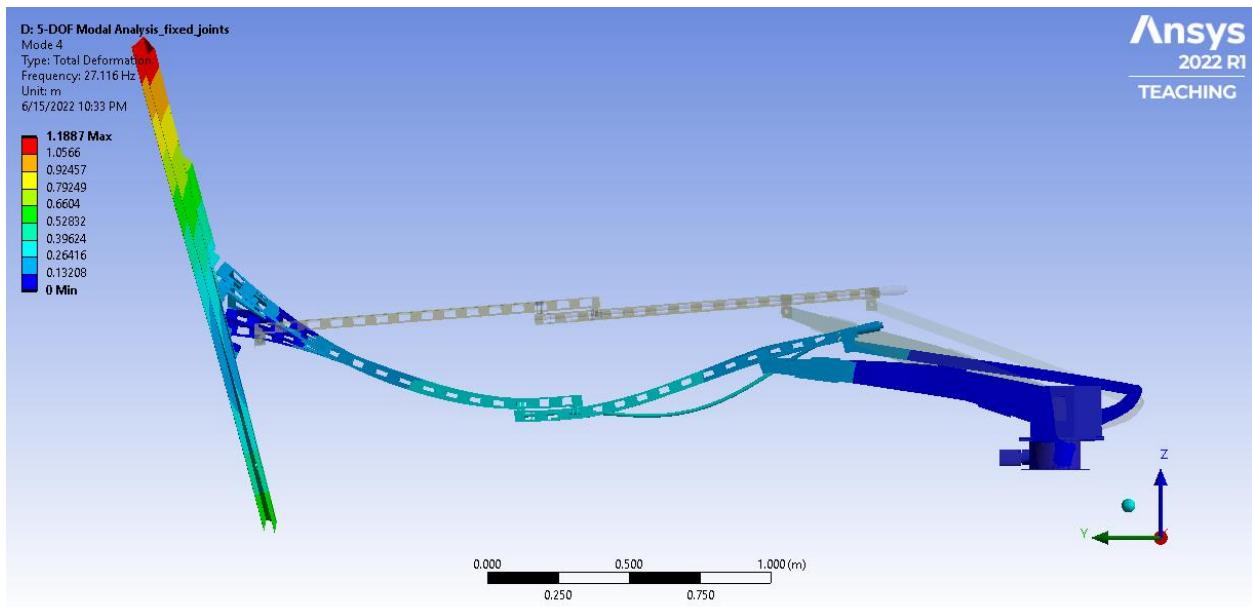


Figure A.4. Forth mode of the 5-DOF manipulator with fixed base and joints (2nd vertical)

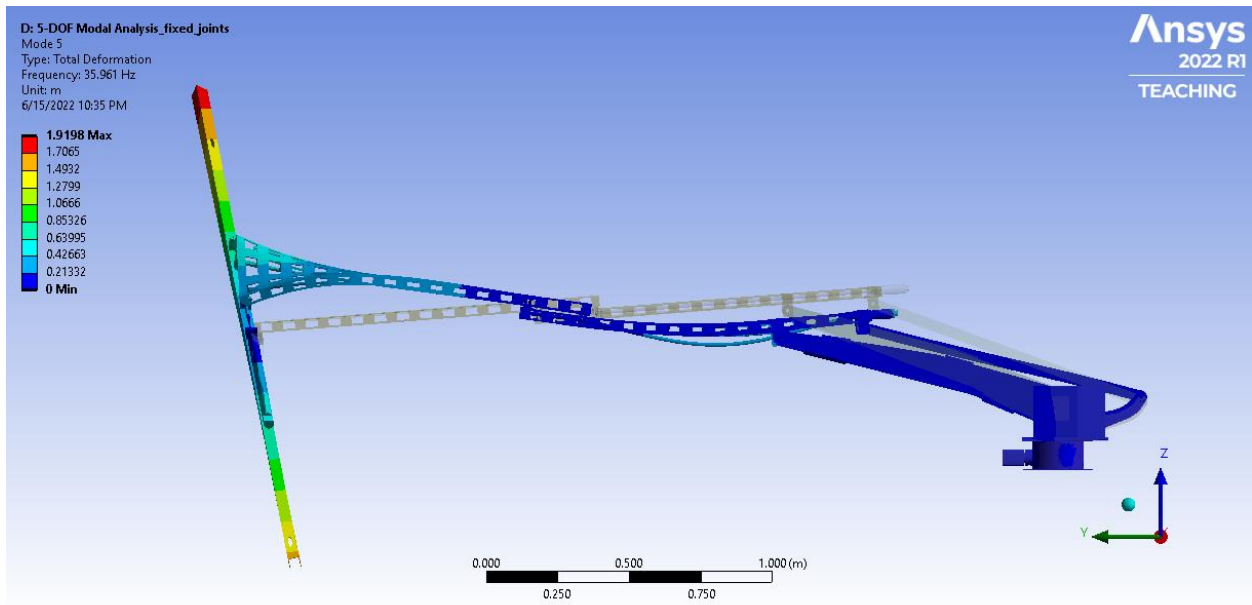


Figure A.5. Fifth mode of the 5-DOF manipulator with fixed base and joints (3rd vertical)

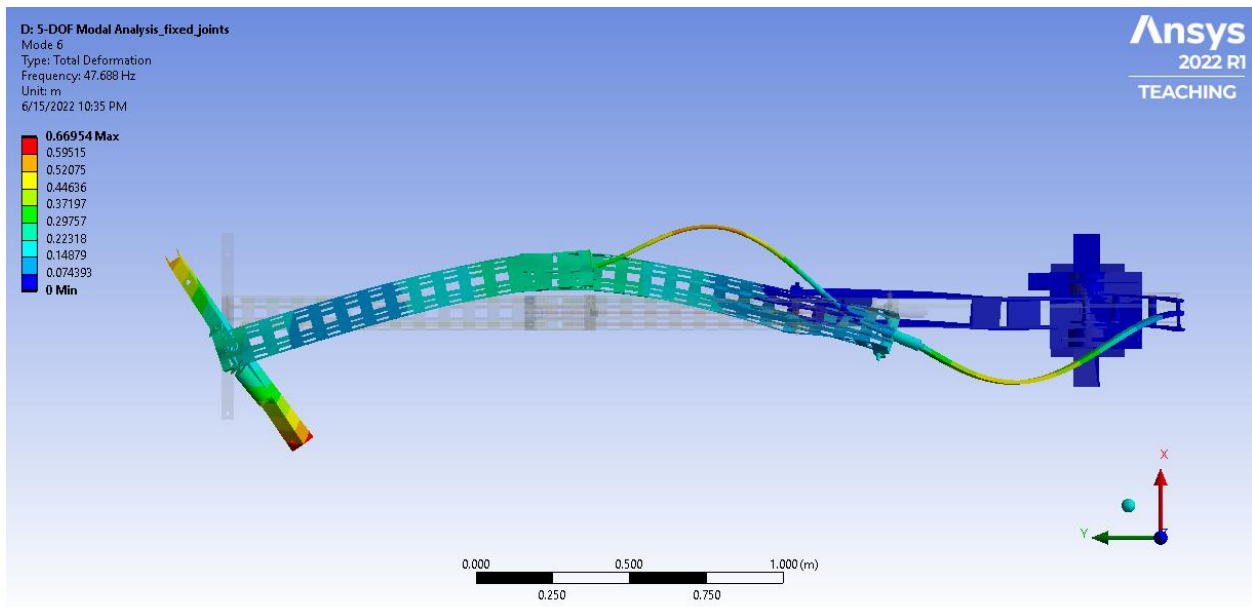


Figure A.6. Sixth mode of the 5-DOF manipulator with fixed base and joints (3rd lateral)

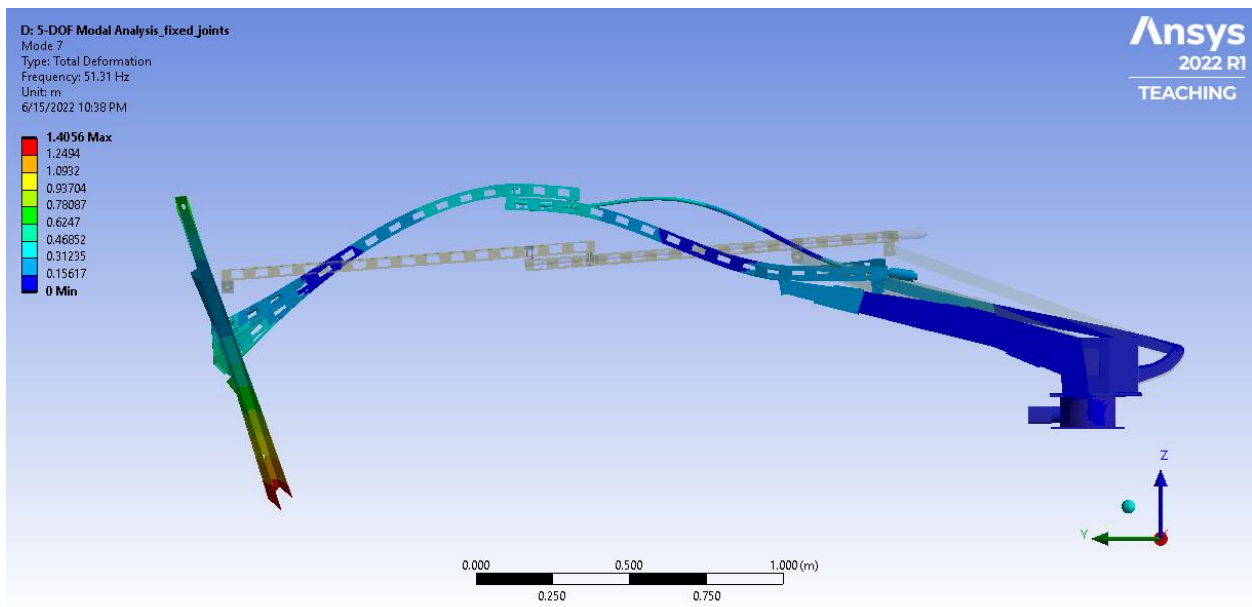


Figure A.7. Seventh mode of the 5-DOF manipulator with fixed base and joints (4th vertical)

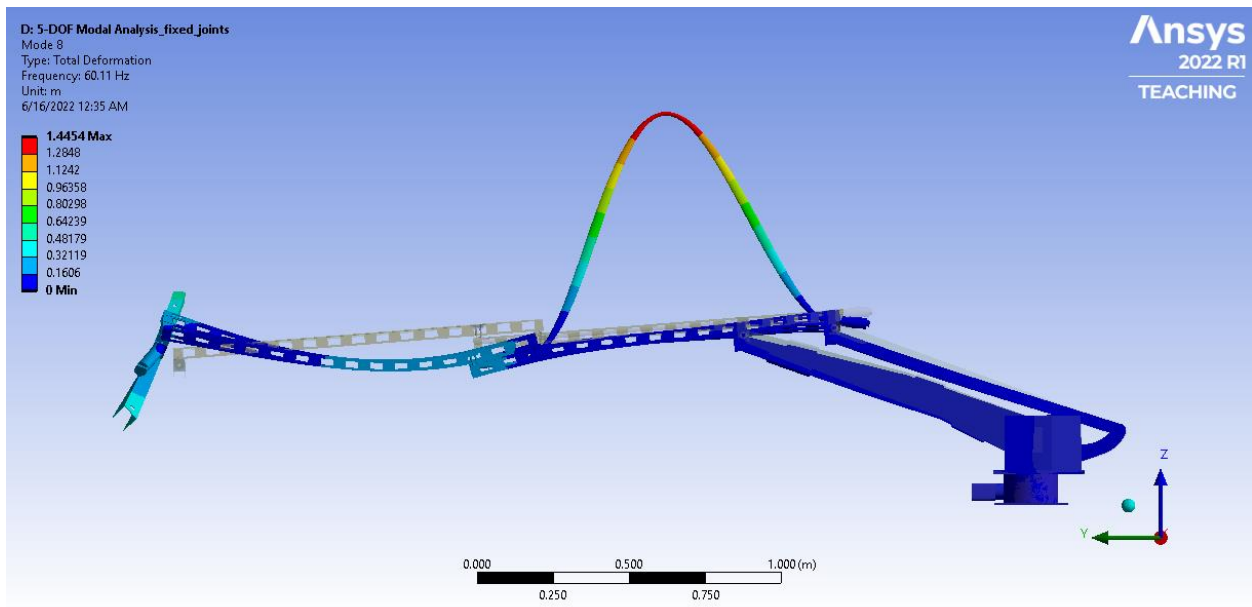


Figure A.8. Eighth mode of the 5-DOF manipulator with fixed base and joints (ball screw vertical)

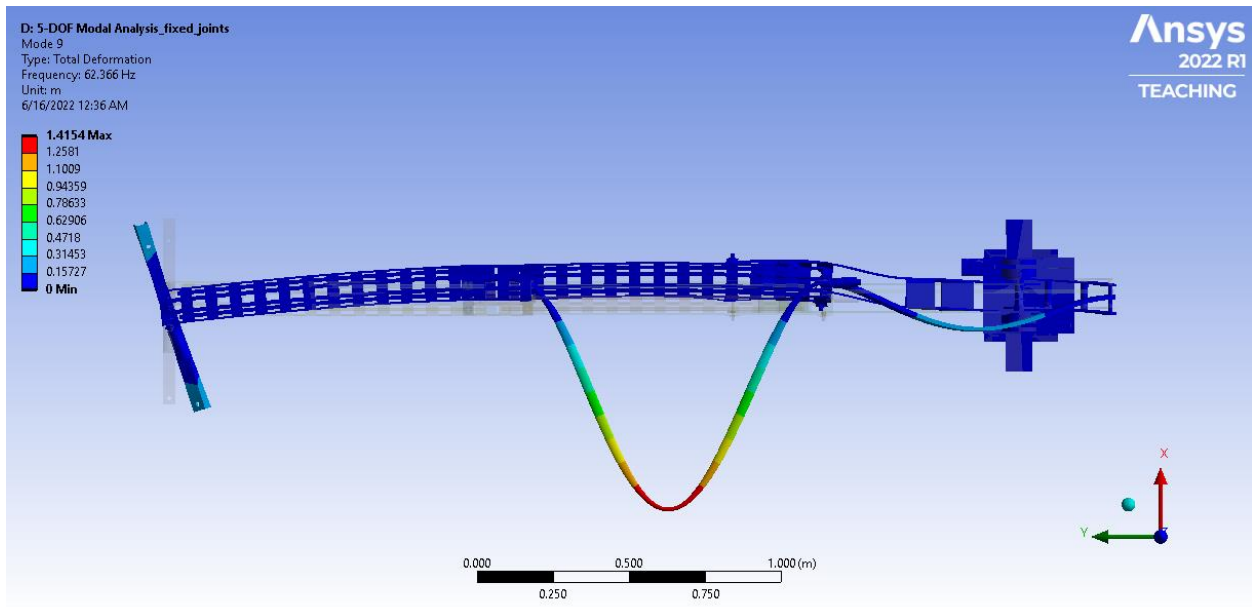


Figure A.9. Ninth mode of the 5-DOF manipulator with fixed base and joints (ball screw lateral)

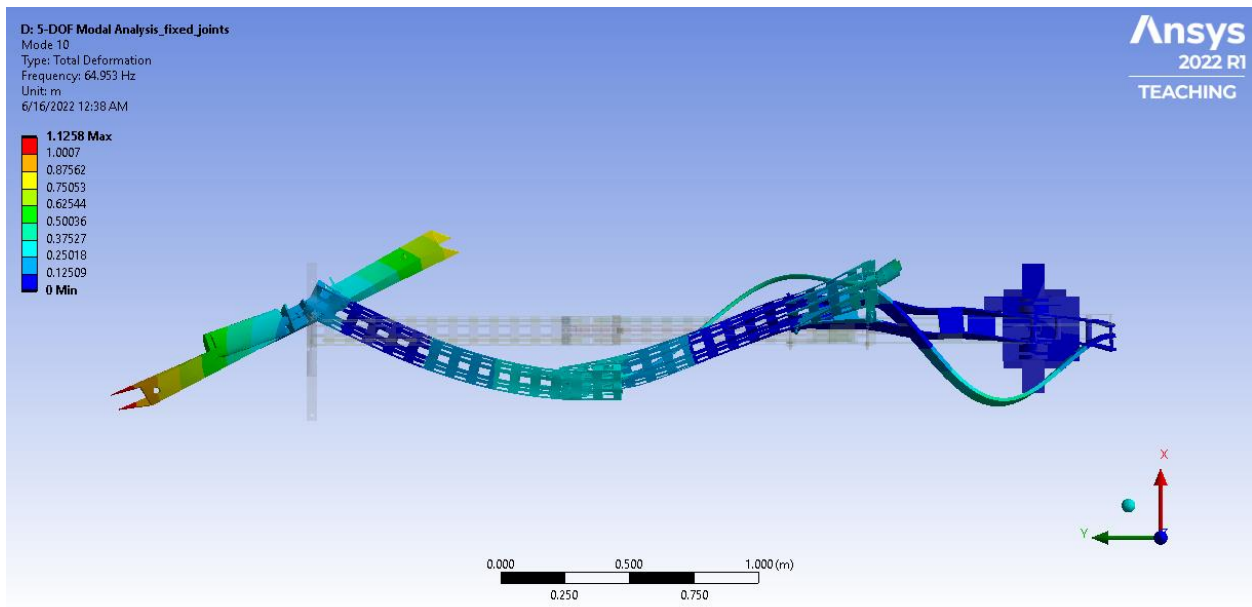


Figure A.10. Tenth mode of the 5-DOF manipulator with fixed base and joints (4th lateral)

B. 5-DOF manipulator modal analysis, section 3.5, 3.8 and 4.5 (free base and joints)

The mode shapes in this part are from modal analysis of the 5-DOF manipulator with free base and joints, *i.e.*, the base can have vertical motion and the 2nd and the 3rd joints are free to rotate. Therefore, all the modes are oscillatory.

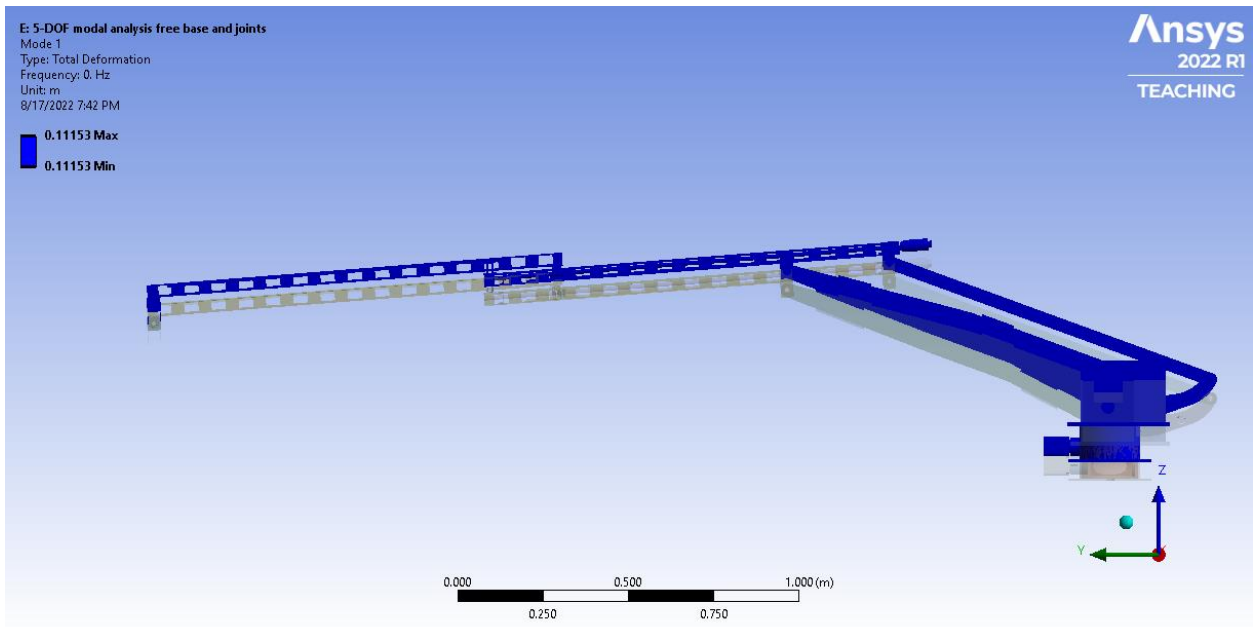


Figure B.1. First mode of the 5-DOF manipulator with free base and joints (1st rigid mode)

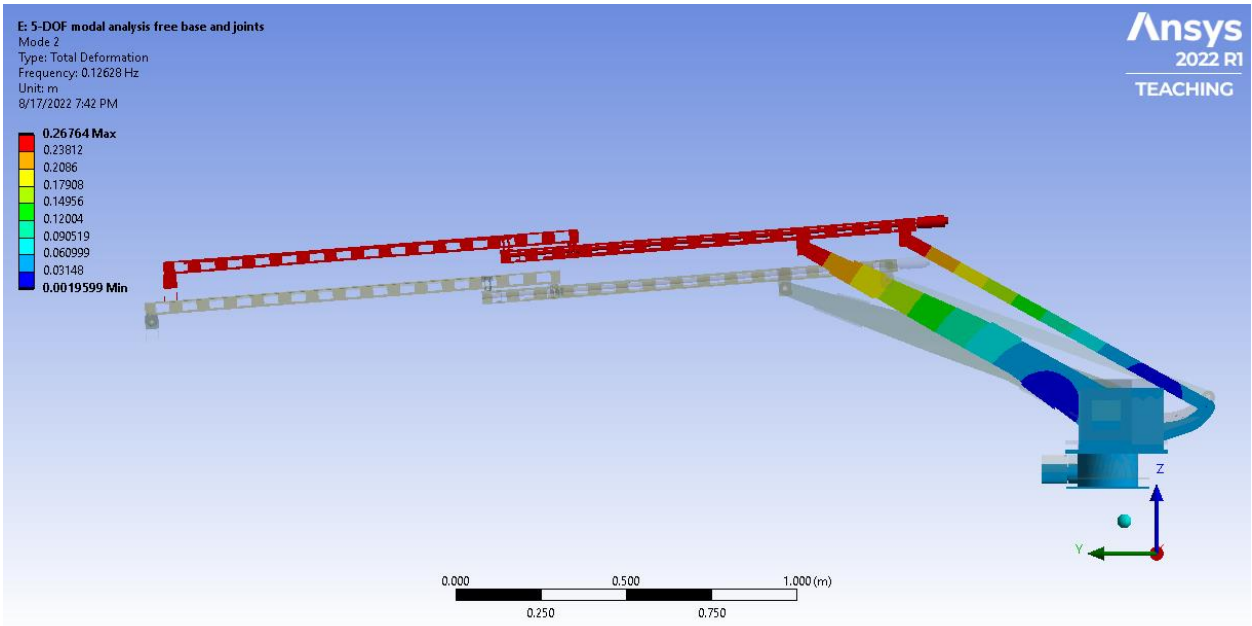


Figure B.2. Second mode of the 5-DOF manipulator with free base and joints (2nd rigid mode)

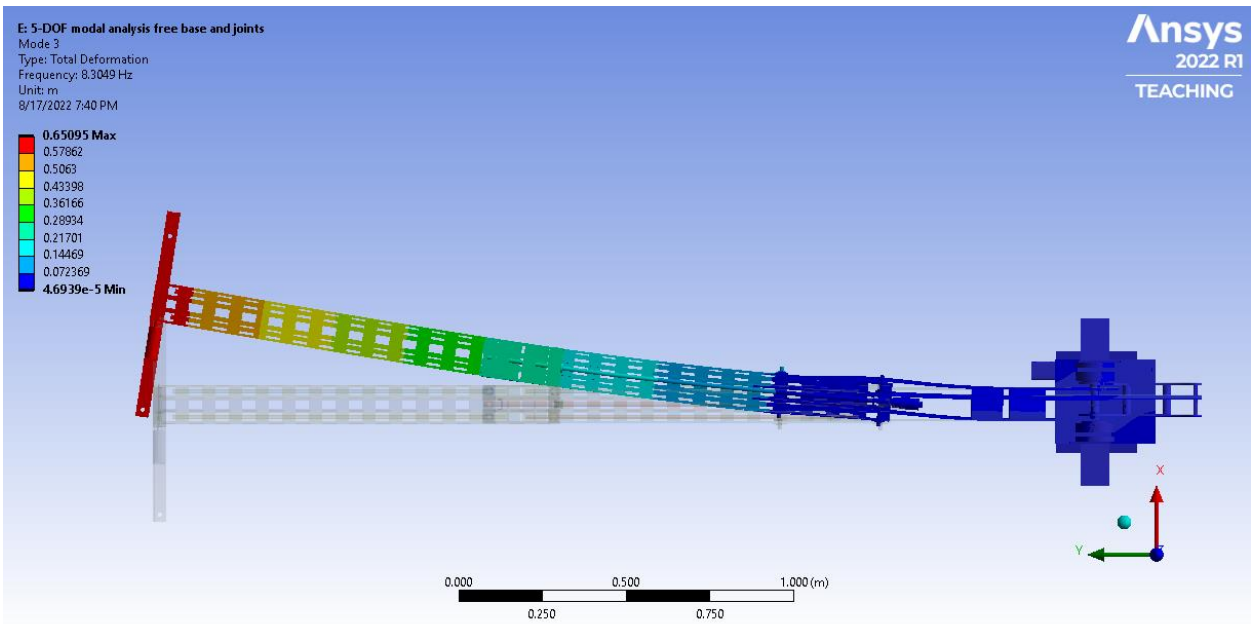


Figure B.3. Third mode of the 5-DOF manipulator with free base and joints

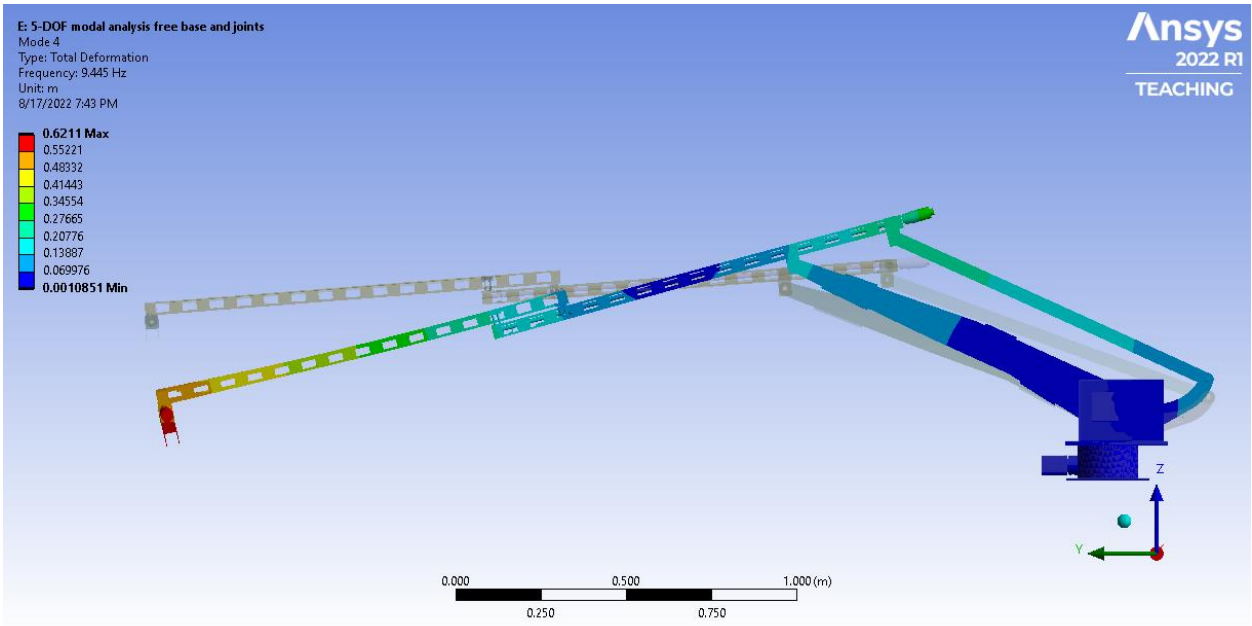


Figure B.4. Forth mode of the 5-DOF manipulator with free base and joints (3rd rigid mode)

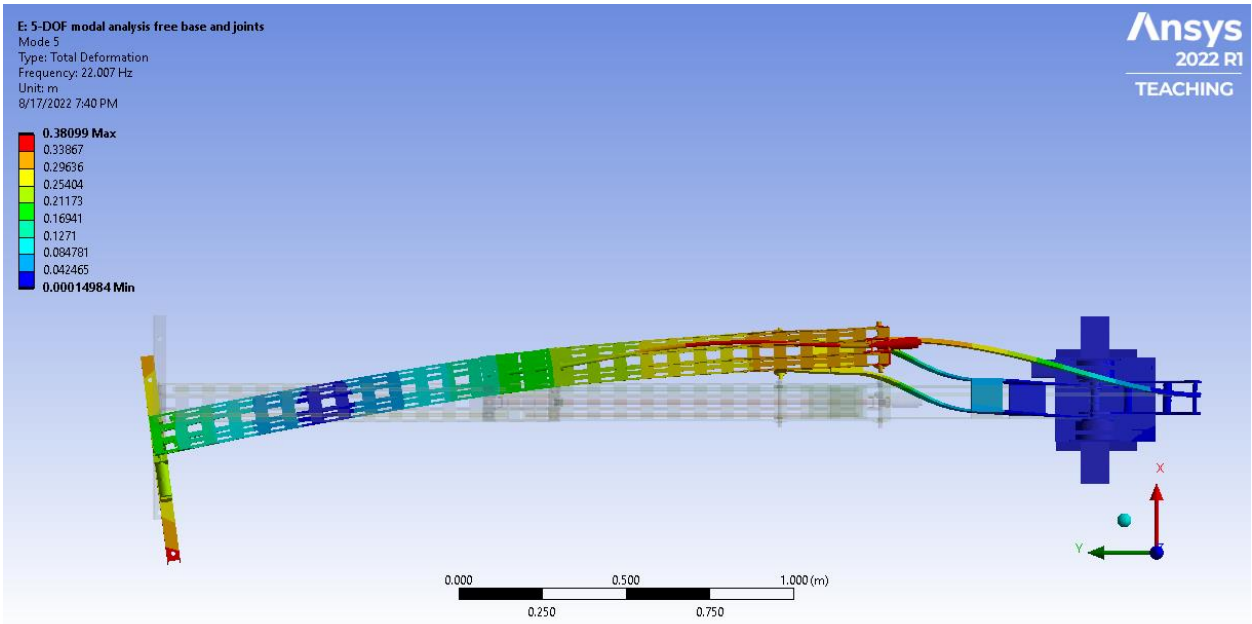


Figure B.5. Fifth mode of the 5-DOF manipulator with free base and joints

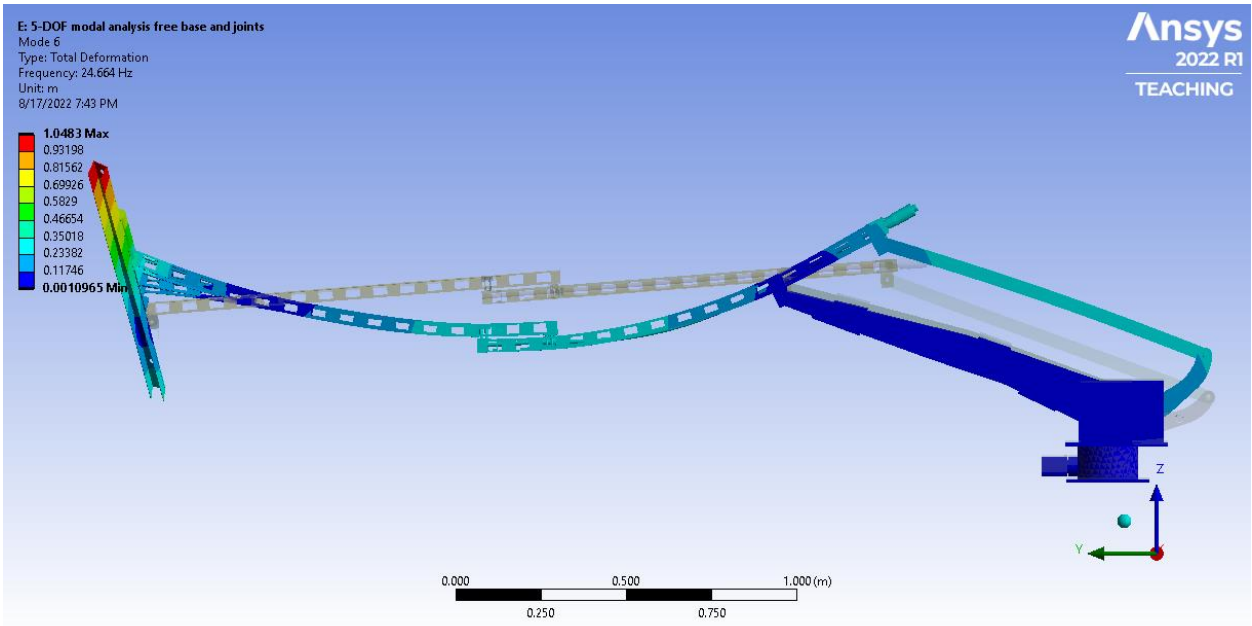


Figure B.6. Sixth mode of the 5-DOF manipulator with free base and joints

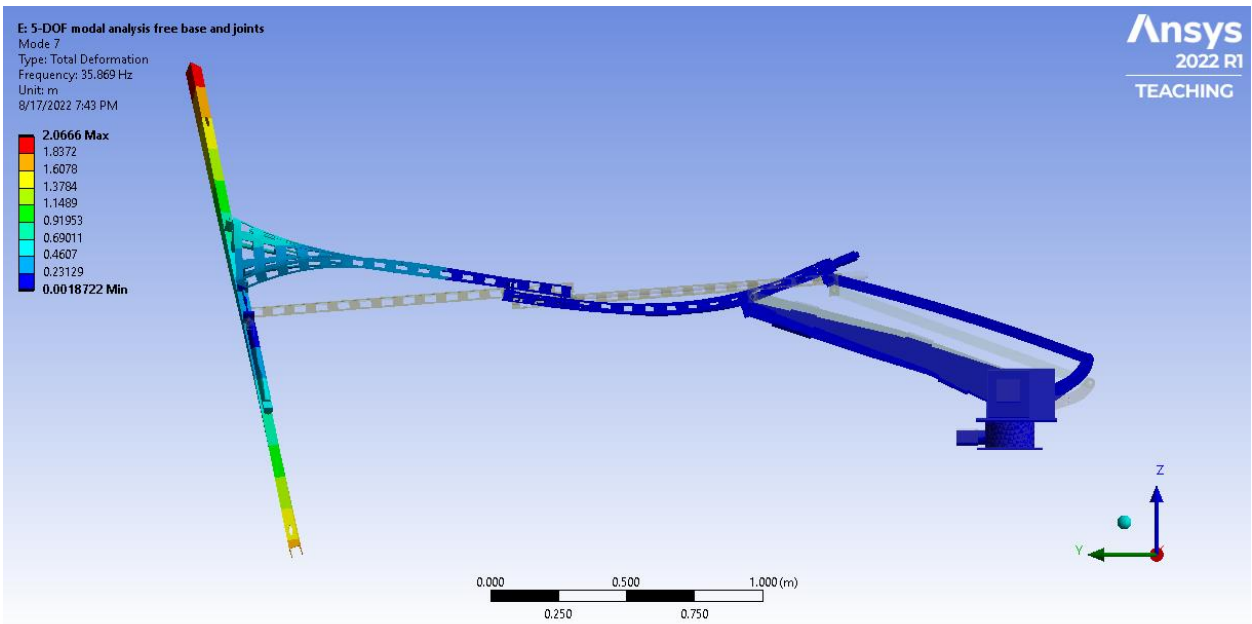


Figure B.7. Seventh mode of the 5-DOF manipulator with free base and joints

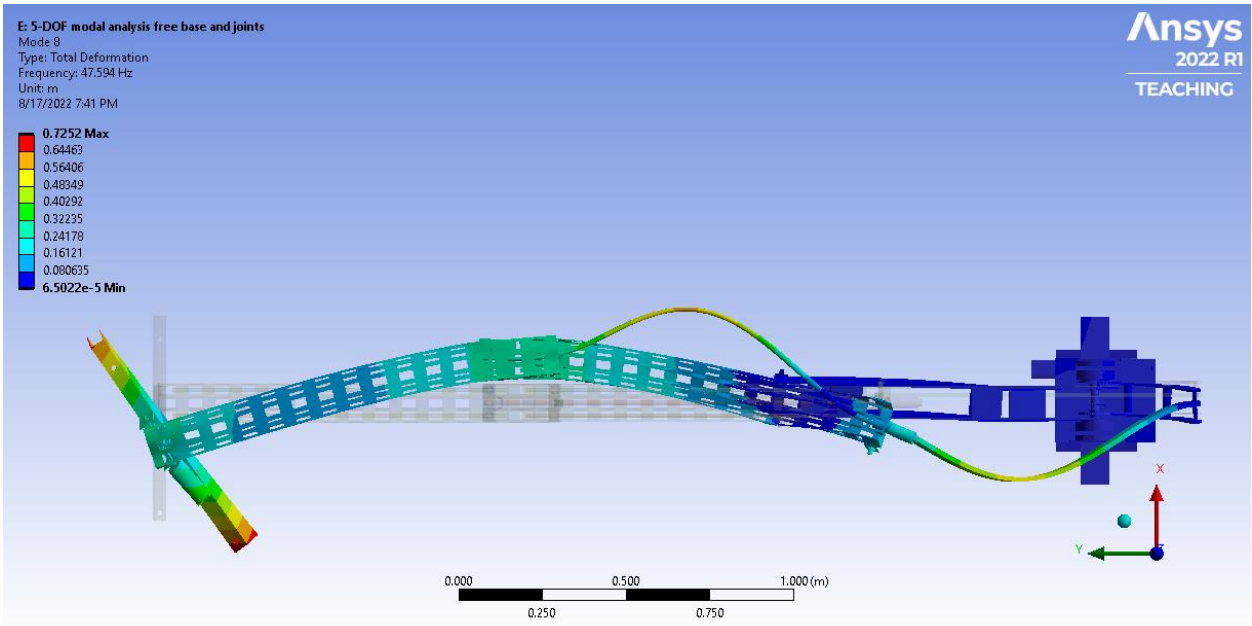


Figure B.8. Eighth mode of the 5-DOF manipulator with free base and joints

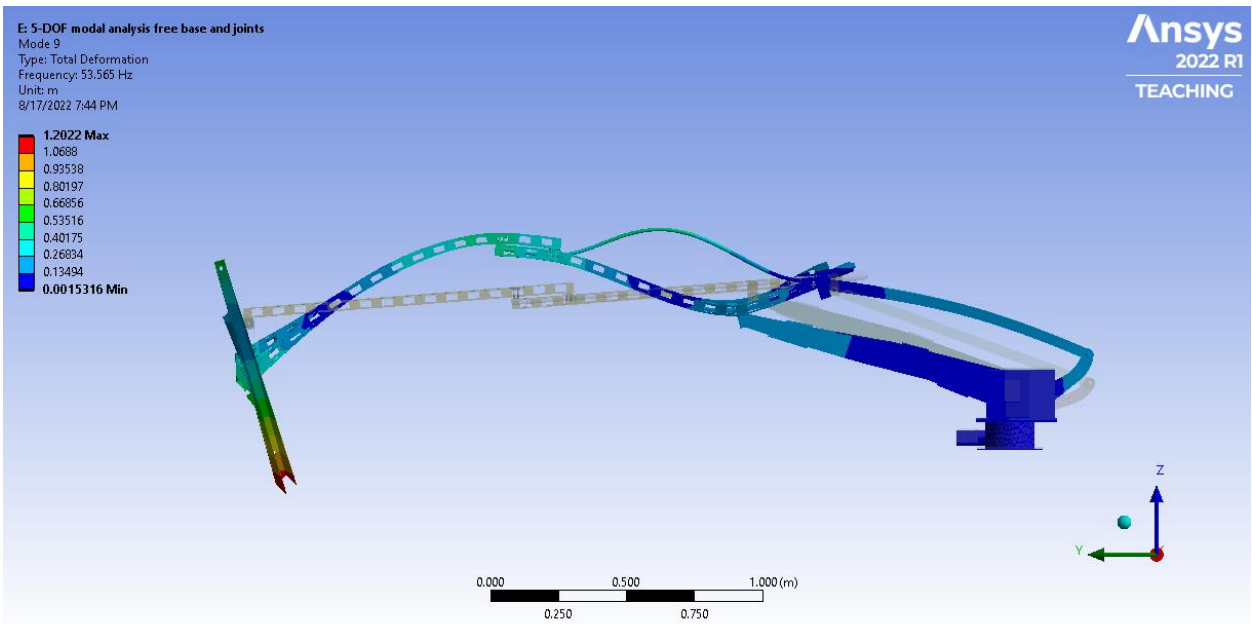


Figure B.9. Ninth mode of the 5-DOF manipulator with free base and joints

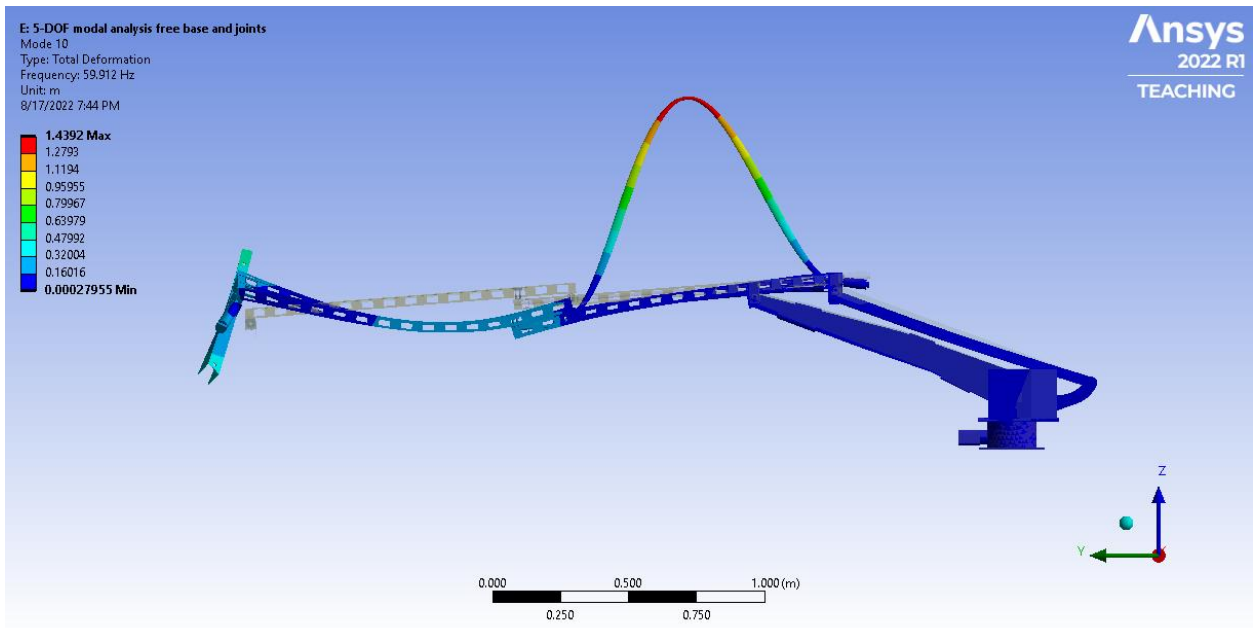


Figure B.10. Tenth mode of the 5-DOF manipulator with free base and joints

C. Cantilever beam modal analysis, section 3.5 and 3.6

Below are the 6 modes of vibration for the cantilever beam, Figures C.1 to C.6.

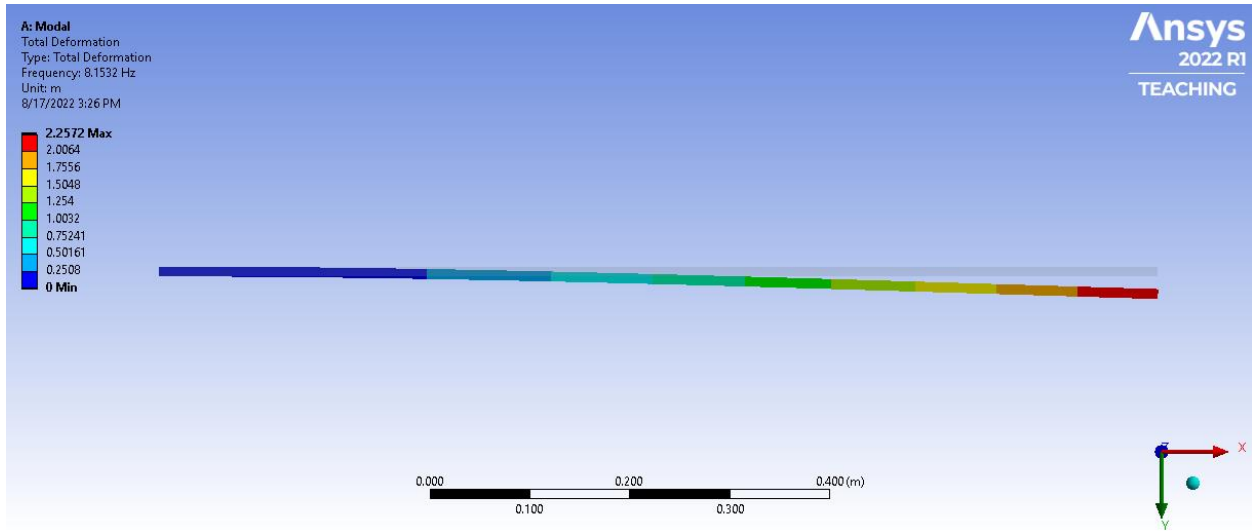


Figure C.1. First mode of the cantilever beam

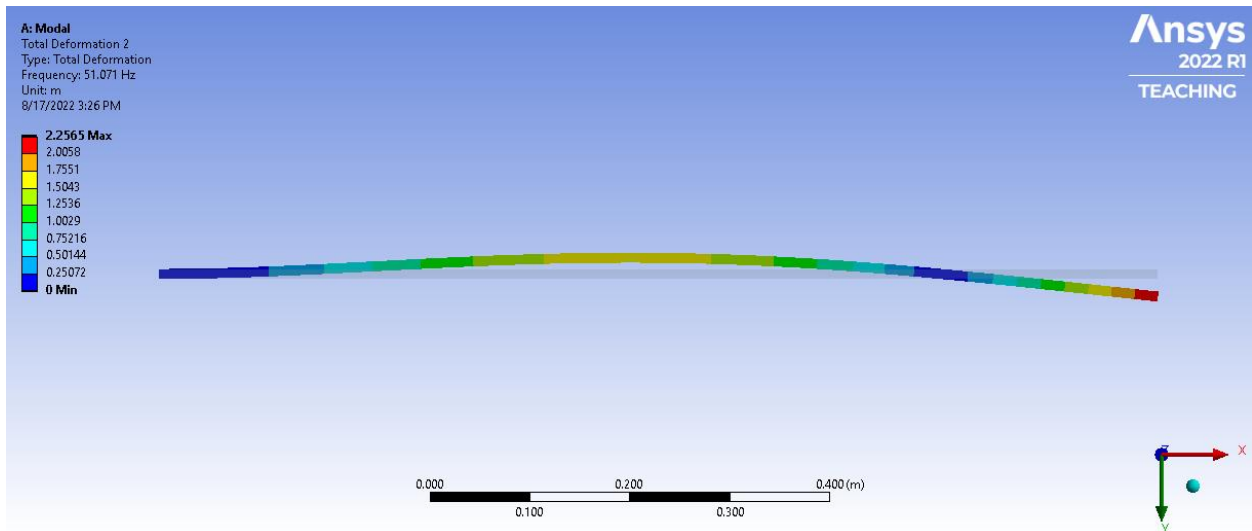


Figure C.2. Second mode of the cantilever beam

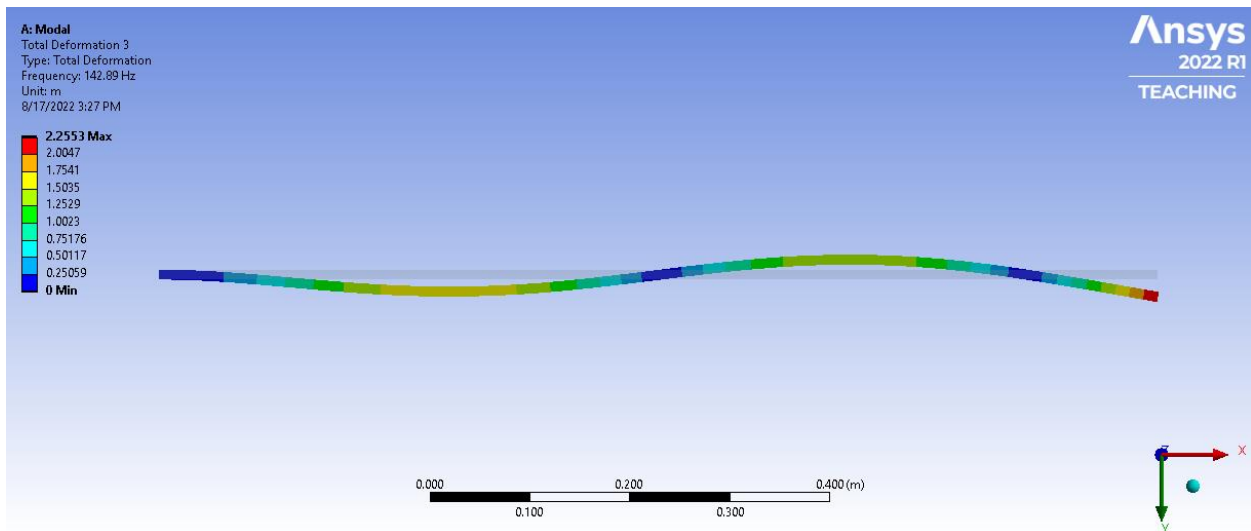


Figure C.3. Third mode of the cantilever beam

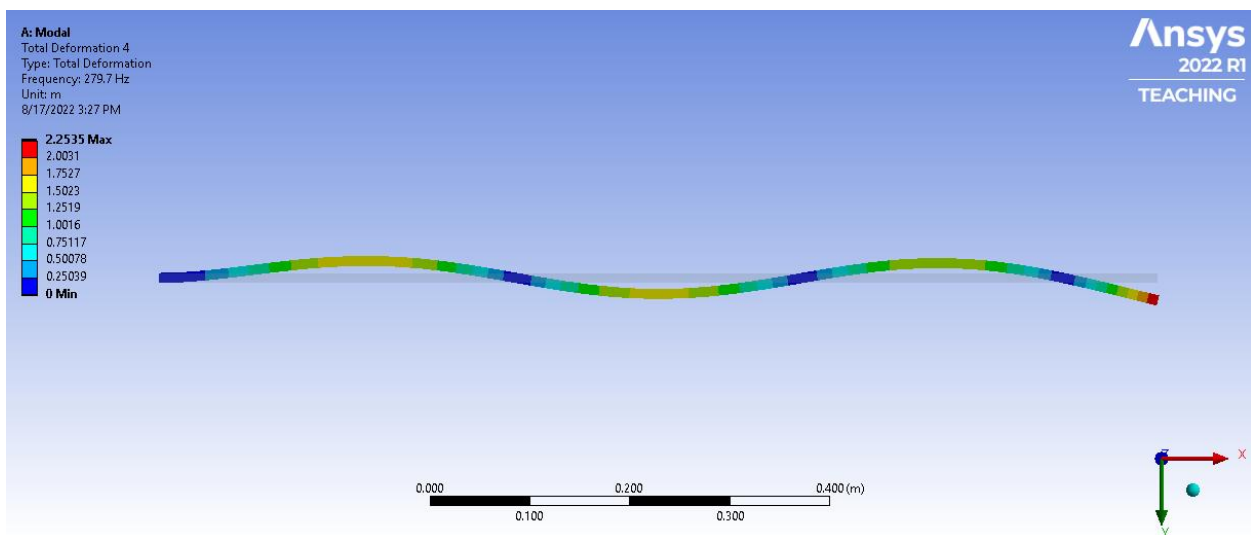


Figure C.4. Fourth mode of the cantilever beam

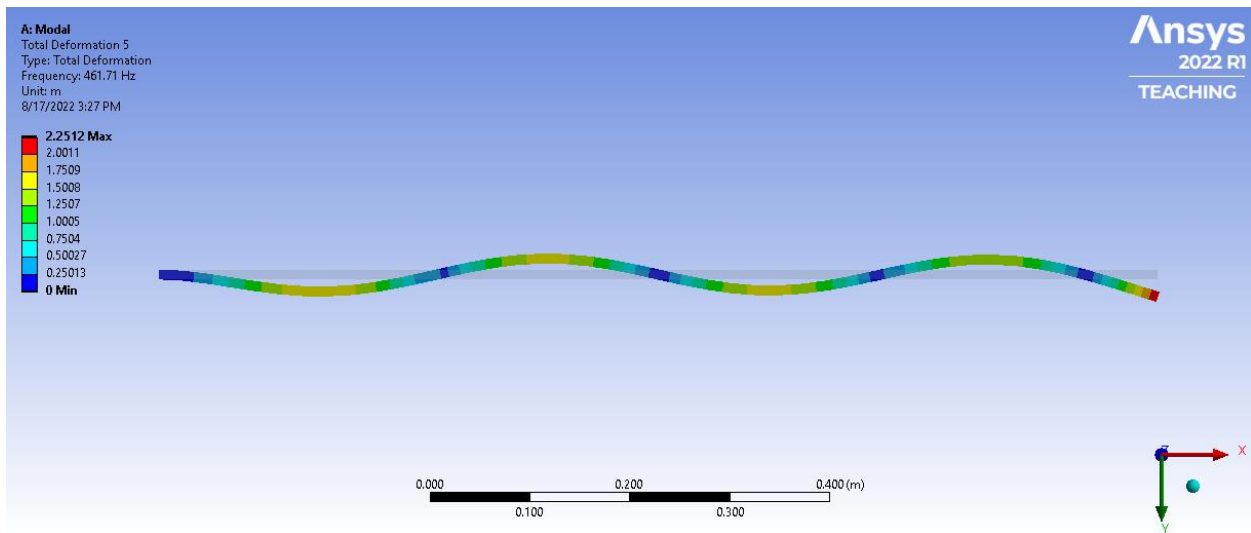


Figure C.5. Fifth mode of the cantilever beam

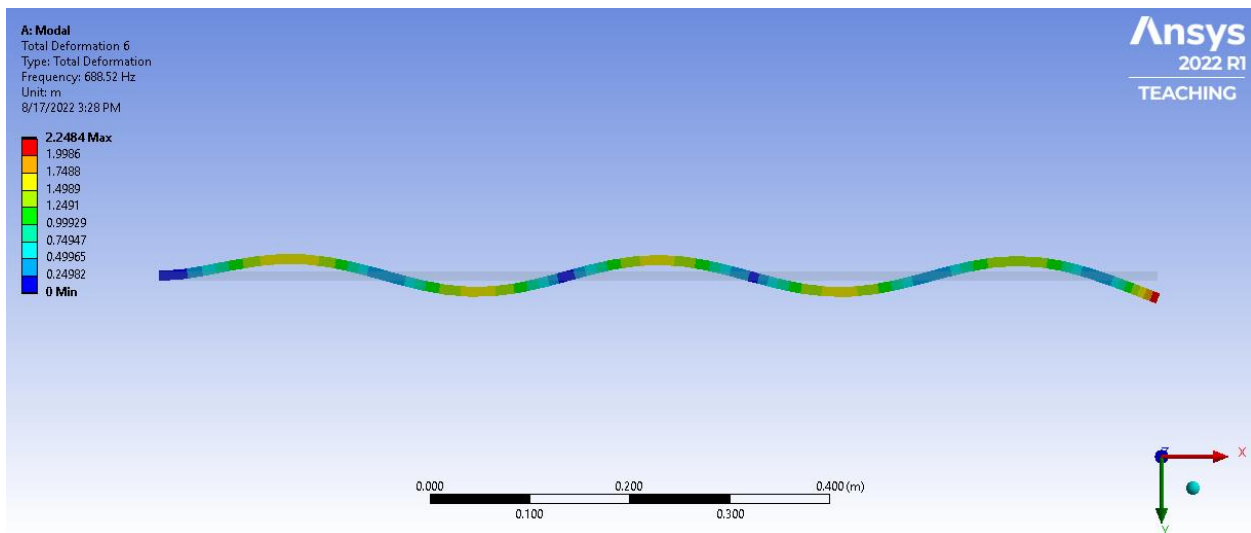


Figure C.6. Sixth mode of the cantilever beam

D. 2L2JM modal analysis section 3.5 and 3.7

Below are the 6 modes of vibration for the 2L2JM, Figures D.1 to D.6.

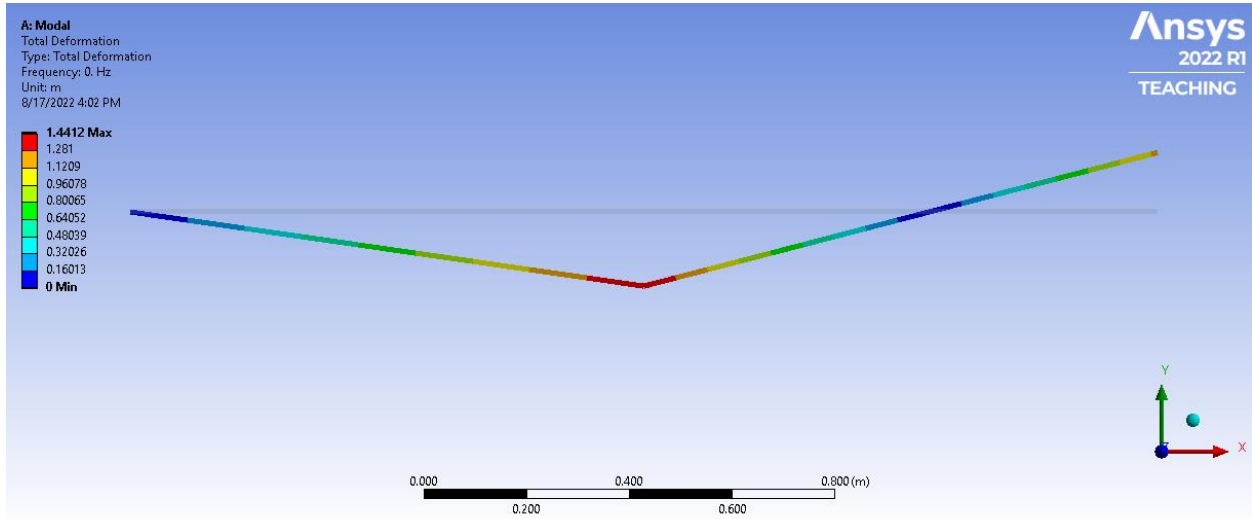


Figure D.1. First mode of vibration for the 2L2JM (1st rigid mode)

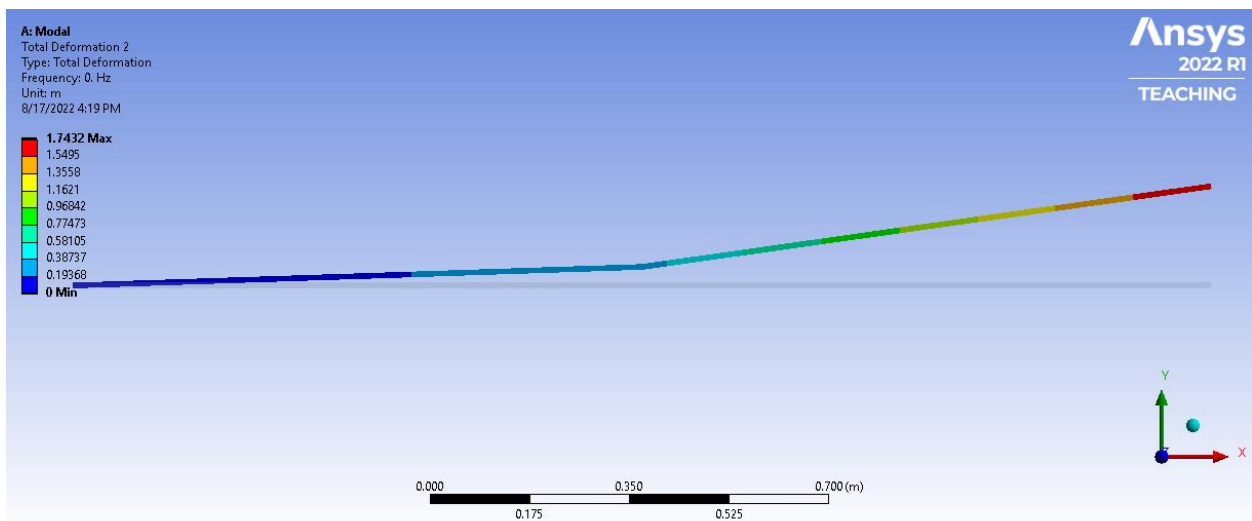


Figure D.2. Second mode of vibration for the 2L2JM (2nd rigid mode)

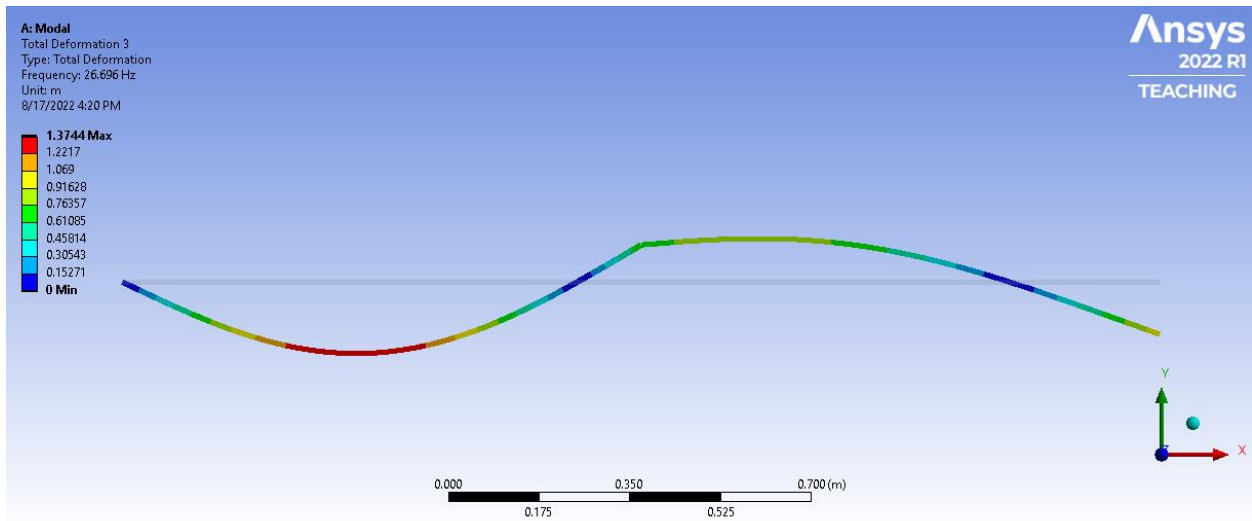


Figure D.3. Third mode of vibration for the 2L2JM

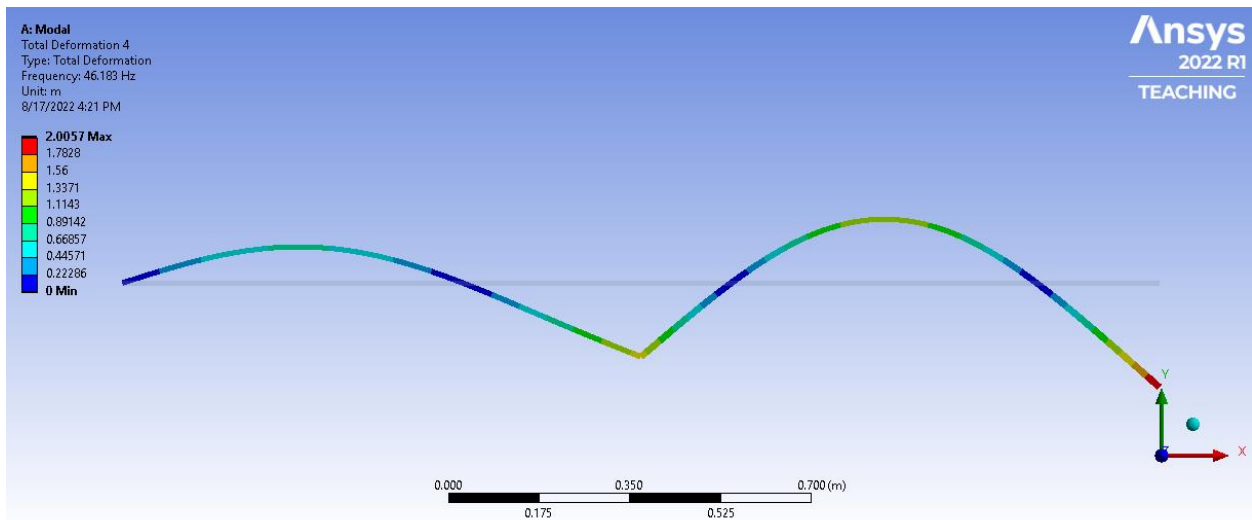


Figure D.4. Fourth mode of vibration for the 2L2JM

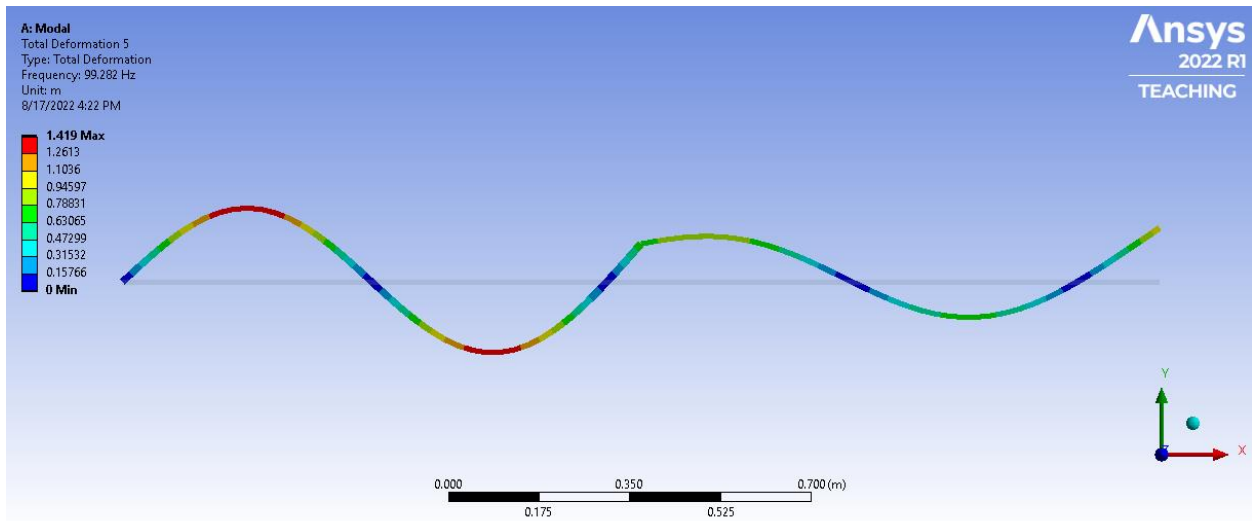


Figure D.5. Fifth mode of vibration for the 2L2JM

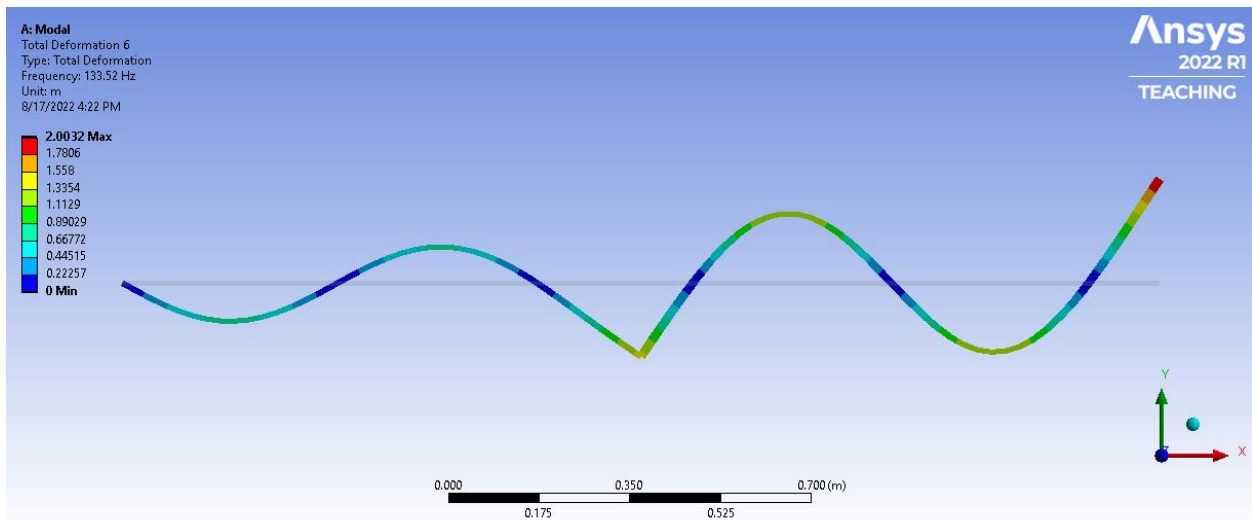


Figure D.6. Sixth mode of vibration for the 2L2JM

E. Removing natural coordinate from Hermit shape function, section 3.1

In some textbooks such as [45], the Hermit shape function for the beam is defined with the natural coordinate ϵ as follows:

$$\left\{ \begin{array}{l} H_1 = \frac{1}{4}(2 - 3\epsilon + \epsilon^3) \\ H_2 = \frac{1}{4}(1 - \epsilon - \epsilon^2 + \epsilon^3) \\ H_3 = \frac{1}{4}(2 + 3\epsilon - \epsilon^3) \\ H_4 = \frac{1}{4}(-1 - \epsilon + \epsilon^2 + \epsilon^3) \end{array} \right. \quad E - 1$$

According to Figure E-1, $\epsilon = \frac{x-l/2}{l/2}$, where x is the physical coordinate and l is the length of the beam.

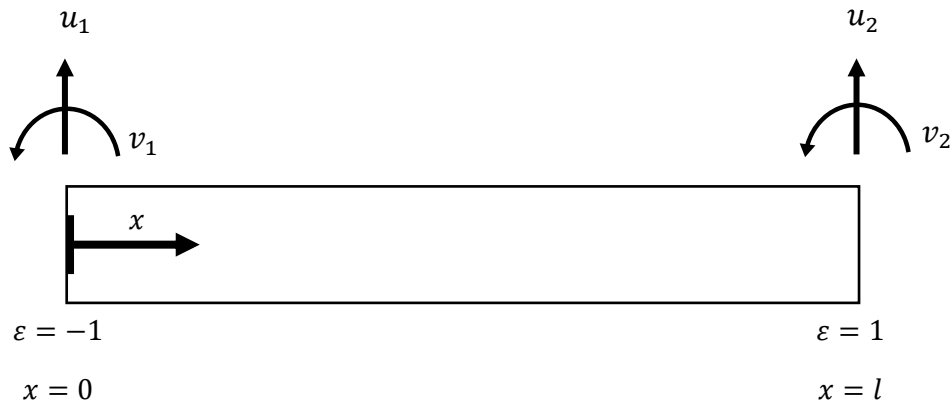


Figure E.1. Beam element and the physical and natural coordinates

By substituting $\epsilon = \frac{2x}{l} - 1$ into equation (E - 1), the shape function becomes equation (3.3).

F. Random vibration generation MATLAB code, section 2.2, 3.6

In this section, the random vibration has been generated with “rand” and then the PSD has been obtained using “pwelch”. The generated random vibration was based on the sample rate of 100Hz; however, when the data was applied to FEA-A, the sample rate should be higher than this number. Therefore, the time interval for the FEA-A was chosen 0.005s which results in the sample rate of $F_s=200$ Hz.

```
t=0:0.01:10; % time with sample rate of 100 Hz
x=(-1+2.*rand(1,length(t)))*1e-2; %white noise in the range
of [-1,1]cm
```

```
Fs=200;
%%EE
Z= EE - mean(EE);
L=length(EE);
[psd_EE_Z,f]=pwelch(Z,[],[],[],Fs);

%% Base
Zb=(base)-mean(base);
L=length(base);
[psd_b_Z,f]=pwelch(Zb,[],[],[],Fs);

%%Displacement Transmissibility
Td=sqrt(psd_EE_Z./psd_b_Z);
```

G. Mass and stiffness matrices, two-link two-joint manipulator(2L2JM), section 3.2 and 3.5

The code represented here is based on symbolic toolbox of MATLAB for the 2L2JM with each link having 3 elements. The result of this code was used for verification in section 3.5.

```

clear
clc

syms t ro A E I
i=2; % #links
j=3; % #elements on each link

syms x11 x12 x13
syms x21 x22 x23
syms l11 l12 l13
syms l21 l22 l23

l=[l11 l12 l13; l21 l22 l23];
x=[x11 x12 x13; x21 x22 x23];

z=sym(zeros(18,1,I,j));
q=sym(zeros(18,1));

syms theta1(t) theta2(t)
syms u11(t) v11(t) u12(t) v12(t) u13(t) v13(t) u14(t) v14(t)
syms u21(t) v21(t) u22(t) v22(t) u23(t) v23(t) u24(t) v24(t)

theta=[theta1(t) theta2(t)];
u=[u11(t) u12(t) u13(t) u14(t); u21(t) u22(t) u23(t) u24(t)];
v=[v11(t) v12(t) v13(t) v14(t); v21(t) v22(t) v23(t) v24(t)];

fi=sym(zeros(1,18,I,j));
y=sym(zeros(I,j));
r=sym(zeros(2,1,I,j));
C=sym(zeros(2,1));

dr_dz=sym(zeros(2,18,I,j));
dr_dz2=sym(zeros(18,18,I,j));
T=sym(zeros(2,2,i));
m=sym(zeros(18,18,I,j));
M=sym(zeros(18,18));
ks=sym(zeros(4,4,I,j));
K=sym(zeros(18,18));

%% States for each element
z(:,1,1,1)=[theta(1);sym(zeros(1,1));u(1,1);v(1,1);u(1,2);v(1,2); ...
sym(zeros(12,1))]; % [5,6,7,8] are active
z(:,1,1,2)=[theta(1);sym(zeros(3,1));u(1,2);v(1,2);u(1,3);v(1,3); ...
sym(zeros(10,1))]; % [7,8,9,10] are active
z(:,1,1,3)=[theta(1);sym(zeros(5,1));u(1,3);v(1,3);u(1,4);v(1,4); ...
sym(zeros(8,1))];

```

```

z(:,1,2,1)=[theta(1);theta(2);sym(zeros(6,1));u(1,4);v(1,4);u(2,1); ...
v(2,1);u(2,2);v(2,2);sym(zeros(4,1))]; %[13,14,15,16] are active
z(:,1,2,2)=[theta(1);theta(2);sym(zeros(6,1));u(1,4);v(1,4); ...
sym(zeros(2,1));u(2,2);v(2,2);u(2,3);v(2,3); ...
sym(zeros(2,1))]; %[15,16,17,18] are active
z(:,1,2,3)=[theta(1);theta(2);sym(zeros(6,1));u(1,4);v(1,4); ...
sym(zeros(4,1));u(2,3);v(2,3);u(2,4);v(2,4)];
%% Generalized Coordinates
c=1;
q(1:2,1)=theta(:);
for i=1:2
    for j=1:4
        q(c+2:c+3,1)=[u(I,j);v(I,j)];
        c=c+2;
    end
end

%% Shape Functions for each element

fi(1,:,1,1)=[sym(zeros(1,2)), 1-3*x(1,1)^2/1(1,1)^2+2*x(1,1)^3/1(1,1)^3, ...
x(1,1)-2*x(1,1)^2/1(1,1)+x(1,1)^3/1(1,1)^2, ...
3*x(1,1)^2/1(1,1)^2-2*x(1,1)^3/1(1,1)^3, ...
-x(1,1)^2/1(1,1)+x(1,1)^3/1(1,1)^2,sym(zeros(1,12))];

fi(1,:,1,2)=[sym(zeros(1,4)), 1-3*x(1,2)^2/1(1,2)^2+2*x(1,2)^3/1(1,2)^3, ...
x(1,2)-2*x(1,2)^2/1(1,2)+x(1,2)^3/1(1,2)^2, ...
3*x(1,2)^2/1(1,2)^2-2*x(1,2)^3/1(1,2)^3, ...
-x(1,2)^2/1(1,2)+x(1,2)^3/1(1,2)^2,sym(zeros(1,10))];

fi(1,:,1,3)=[sym(zeros(1,6)), 1-3*x(1,3)^2/1(1,3)^2+2*x(1,3)^3/1(1,3)^3, ...
x(1,3)-2*x(1,3)^2/1(1,3)+x(1,3)^3/1(1,3)^2, ...
3*x(1,3)^2/1(1,3)^2-2*x(1,3)^3/1(1,3)^3, ...
-x(1,3)^2/1(1,3)+x(1,3)^3/1(1,3)^2,sym(zeros(1,8))];

fi(1,:,2,1)=[sym(zeros(1,10)), 1-3*x(2,1)^2/1(2,1)^2+2*x(2,1)^3/1(2,1)^3, ...
x(2,1)-2*x(2,1)^2/1(2,1)+x(2,1)^3/1(2,1)^2, ...
3*x(2,1)^2/1(2,1)^2-2*x(2,1)^3/1(2,1)^3, ...
-x(2,1)^2/1(2,1)+x(2,1)^3/1(2,1)^2,sym(zeros(1,4))];

fi(1,:,2,2)=[sym(zeros(1,12)), 1-3*x(2,2)^2/1(2,2)^2+2*x(2,2)^3/1(2,2)^3, ...
x(2,2)-2*x(2,2)^2/1(2,2)+x(2,2)^3/1(2,2)^2, ...
3*x(2,2)^2/1(2,2)^2-2*x(2,2)^3/1(2,2)^3, ...
-x(2,2)^2/1(2,2)+x(2,2)^3/1(2,2)^2,sym(zeros(1,2))];

fi(1,:,2,3)=[sym(zeros(1,14)), 1-3*x(2,3)^2/1(2,3)^2+2*x(2,3)^3/1(2,3)^3, ...
x(2,3)-2*x(2,3)^2/1(2,3)+x(2,3)^3/1(2,3)^2, ...
3*x(2,3)^2/1(2,3)^2-2*x(2,3)^3/1(2,3)^3, ...
-x(2,3)^2/1(2,3)+x(2,3)^3/1(2,3)^2];

%% Vertical 128columns128s of points of elements
for i=1:2
    for j=1:3
        y(I,j)=fi(1,:,I,j)*z(:,1,I,j);
    end
end

%% Rotation Matrices

```

```

a=[theta(1), theta(2)+v(1,4)];
for i=1:2
    T(:, :, i)=[cos(a(i)), -sin(a(i)); sin(a(i)), cos(a(i))];
end

%% r: Positions of points for each element
for i=1:2

    for j=1:3

        if i==1

            if j==1
                l1=sym(0);
            else
                l1=l1+1(I, j-1);
            end

            r(:, :, I, j)=T(:, :, i)*[l1+x(I, j); y(I, j)];

        elseif i==2

            if j==1
                l2=sym(0);
            else
                l2=l2+1(I, j-1);
            end

            r(:, :, I, j)=T(:, :, i-1)*([l1; u(1,4)]+T(:, :, i)*[l2+x(I, j); ...
                y(I, j)]); %u(1,4)=u(1,end)

        end

    end

end

%% dr/dz

for i=1:2
    for j=1:3
        for c=1:18
            if z(c,1,I,j)~=0
                dr_dz(:, c, I, j)=diff(r(:, 1, I, j), z(c,1,I,j));
            else
                dr_dz(:, c, I, j)=0;
            end
        end
    end
end

%% dr_dz transpose and its quadratic form
dr_dz_trans=permute(dr_dz, [2,1,3,4]);
for i=1:2
    for j=1:3
        dr_dz2(:, :, I, j)=dr_dz_trans(:, :, I, j)*dr_dz(:, :, I, j);
    end
end
% (4*2)*(2*4)=>4*4

```

```

        end
    end

    %% Trapezoid integration for Mass matrix
    for i=1:2
        for j=1:3
            for i1=1:18
                for i2=1:18
                    m(i1,i2,I,j)=ro*A*(int(dr_dz2(i1,i2,I,j),x(I,j),0,l(I,j)));
                end
            end
        end
    end

    %% Assemble Mass Matrices

    for i=1:2
        for j=1:3
            M(:, :) = M(:, :) + m(:, :, I, j);
        end
    end

    %% Stiffness Matrix and its assemble
    d=3;
    for i=1:2
        for j=1:3
            ks(:, :, I, j) = E*I*[12/l(I, j)^3,    6/l(I, j)^2, -12/l(I, j)^3,
6/l(I, j)^2; ...
                                6/l(I, j)^2,    4/l(I, j),    -6/l(I, j)^2,  2/l(I, j); ...
                                -12/l(I, j)^3,   -6/l(I, j)^2,   12/l(I, j)^3,  -
6/l(I, j)^2; ...
                                6/l(I, j)^2,    2/l(I, j),    -6/l(I, j)^2,  4/l(I, j)];

            K(d:d+3, d:d+3) = K(d:d+3, d:d+3) + ks(:, :, I, j);
            d=d+2;
        end
    end
    d=d+2;

    %% Eliminating rows and columns for u,v=0
    q([3,4,11,12], :) = [];

    qd(:, :) = diff(q(:, :), t);
    qdd(:, :) = diff(qd(:, :), t);
    M([3,4,11,12], :) = [];
    M(:, [3,4,11,12]) = [];
    K([3,4,11,12], :) = [];
    K(:, [3,4,11,12]) = [];

```

The resulting global stiffness matrices are given below (zero matrix elements are not mentioned):

Considering $q = [\theta_1, \theta_2, u_{12}, v_{12}, u_{13}, v_{13}, u_{14}, v_{14}, u_{22}, v_{22}, u_{23}, v_{23}, u_{24}, v_{24}]$

$$K_{3,3}, K_{3,4}, K_{3,5}, K_{3,6} = \frac{12 * E * I * (l_{11}^3 + l_{12}^3)}{l_{11}^3 * l_{12}^3}, \frac{6 * E * I * (l_{11}^2 - l_{12}^2)}{l_{11}^2 * l_{12}^2}, -\frac{12 * E * I}{l_{12}^3}, \frac{6 * E * I}{l_{12}^2}$$

$$K_{4,3}, K_{4,4}, K_{4,5}, K_{4,6} = \frac{6 * E * I * (l_{11}^2 - l_{12}^2)}{l_{11}^2 * l_{12}^2}, \frac{4 * E * I * (l_{11} + l_{12})}{l_{11} * l_{12}}, -\frac{6 * E * I}{l_{12}^2}, \frac{2 * E * I}{l_{12}}$$

$$K_{5,3}, K_{5,4}, K_{5,5}, K_{5,6}, K_{5,5}, K_{5,6} \\ = -\frac{12 * E * I}{l_{12}^3}, -\frac{6 * E * I}{l_{12}^2}, \frac{12 * E * I * (l_{12}^3 + l_{13}^3)}{l_{12}^3 * l_{13}^3}, \frac{6 * E * I * (l_{12}^2 - l_{13}^2)}{l_{12}^2 * l_{13}^2}, -\frac{12 * E * I}{l_{13}^3}, \frac{6 * E * I}{l_{13}^2}$$

$$K_{6,3}, K_{6,4}, K_{6,5}, K_{6,6}, K_{6,5}, K_{6,6} = \frac{6 * E * I}{l_{12}^2}, \frac{2 * E * I}{l_{12}}, \frac{6 * E * I * (l_{12}^2 - l_{13}^2)}{l_{12}^2 * l_{13}^2}, \\ \frac{4 * E * I * (l_{12} + l_{13})}{l_{12} * l_{13}}, -\frac{6 * E * I}{l_{13}^2}, \frac{2 * E * I}{l_{13}}$$

$$K_{7,7}, K_{7,8}, K_{7,9}, K_{7,10} = -\frac{12 * E * I}{l_{13}^3}, -\frac{6 * E * I}{l_{13}^2}, \frac{12 * E * I}{l_{13}^3}, -\frac{6 * E * I}{l_{13}^2}$$

$$K_{8,9}, K_{8,10}, K_{8,11}, K_{8,12} = \frac{6 * E * I}{l_{13}^2}, \frac{2 * E * I}{l_{13}}, -\frac{6 * E * I}{l_{13}^2}, \frac{4 * E * I}{l_{13}}$$

$$K_{9,9}, K_{9,10}, K_{9,11}, K_{9,12} \\ = \frac{12 * E * I * (l_{21}^3 + l_{22}^3)}{l_{21}^3 * l_{22}^3}, \frac{6 * E * I * (l_{21}^2 - l_{22}^2)}{l_{21}^2 * l_{22}^2}, -\frac{12 * E * I}{l_{22}^3}, \frac{6 * E * I}{l_{22}^2}$$

$$K_{10,9}, K_{10,10}, K_{10,11}, K_{10,12} \\ = \frac{6 * E * I * (l_{21}^2 - l_{22}^2)}{l_{21}^2 * l_{22}^2}, \frac{4 * E * I * (l_{21} + l_{22})}{l_{21} * l_{22}}, -\frac{6 * E * I}{l_{22}^2}, \frac{2 * E * I}{l_{22}}$$

$$K_{11,9}, K_{11,10}, K_{11,11}, K_{11,12}, K_{11,13}, K_{11,14} \\ = -\frac{12 * E * I}{l_{22}^3}, -\frac{6 * E * I}{l_{22}^2}, \frac{12 * E * I * (l_{22}^3 + l_{23}^3)}{l_{22}^3 * l_{23}^3}, \frac{6 * E * I * (l_{22}^2 - l_{23}^2)}{l_{22}^2 * l_{23}^2}, -\frac{12 * E * I}{l_{23}^3}, \frac{6 * E * I}{l_{23}^2}$$

$$K_{12,9}, K_{12,10}, K_{12,11}, K_{12,12}, K_{12,13}, K_{12,14} \\ = \frac{6 * E * I}{l_{22}^2}, \frac{2 * E * I}{l_{22}}, \frac{6 * E * I * (l_{22}^2 - l_{23}^2)}{l_{22}^2 * l_{23}^2}, \frac{4 * E * I * (l_{22} + l_{23})}{l_{22} * l_{23}}, -\frac{6 * E * I}{l_{23}^2}, \frac{2 * E * I}{l_{23}}$$

$$K_{13,11}, K_{13,12}, K_{13,13}, K_{13,14} = -\frac{12 * E * I}{l_{23}^3}, -\frac{6 * E * I}{l_{23}^2}, \frac{12 * E * I}{l_{23}^3}, -\frac{6 * E * I}{l_{23}^2}$$

$$K_{14,11}, K_{14,12}, K_{14,13}, K_{14,14} = \frac{6 * E * I}{l_{23}^2}, \frac{2 * E * I}{l_{23}}, -\frac{6 * E * I}{l_{23}^2}, \frac{4 * E * I}{l_{23}}$$

The Global mass matrices are too big to be given here, however the reader can simply obtain it by the provided code.

H. Mass and stiffness matrices, 5-DOF manipulator, section 3.2

The code represented here is based on symbolic toolbox for a parallelogram with each link having 3 elements. This code is with the help of [32]. Since the main objective of this thesis was modeling the real 5-DOF manipulator and not a parallelogram, the result of the code here was not used for any verification. As stated in Chapter 3, the state-space model of the 5-DOF manipulator is just based on the eigenvectors extracted from FEA-A.

```
clear
clc

syms t ro A E I
i=4; % #links
j=3; % #elements on each link

syms x11 x12 x13
syms x21 x22 x23
syms x31 x32 x33
syms x41 x42 x43

syms l11 l12 l13
syms l21 l22 l23
syms l31 l32 l33
syms l41 l42 l43

l=[l11 l12 l13; l21 l22 l23; l31 l32 l33; l41 l42 l43];
x=[x11 x12 x13; x21 x22 x23; x31 x32 x33; x41 x42 x43];

l13=sym(0);
l23=sym(0);
l33=sym(0);

x13=sym(0);
x23=sym(0);
x33=sym(0);

z=sym(zeros(36,1,i,j));
q=sym(zeros(36,1));
F=sym(zeros(22,1));
B=sym(zeros(36,2));
Bd=sym(zeros(36,2));

syms theta1(t) theta2(t) theta3(t) theta4(t)
syms u11(t) v11(t) u12(t) v12(t) u13(t) v13(t) u14(t) v14(t)
syms u21(t) v21(t) u22(t) v22(t) u23(t) v23(t) u24(t) v24(t)
syms u31(t) v31(t) u32(t) v32(t) u33(t) v33(t) u34(t) v34(t)
syms u41(t) v41(t) u42(t) v42(t) u43(t) v43(t) u44(t) v44(t)
```

```

theta=[theta1(t) theta2(t) theta3(t) theta4(t)];
u=[u11(t) u12(t) u13(t) u14(t); u21(t) u22(t) u23(t) u24(t); u31(t) ...
   u32(t) u33(t) u34(t); u41(t) u42(t) u43(t) u44(t)];
v=[v11(t) v12(t) v13(t) v14(t); v21(t) v22(t) v23(t) v24(t); v31(t) ...
   v32(t) v33(t) v34(t); v41(t) v42(t) v43(t) v44(t)];

fi=sym(zeros(1,36,i,j));
y=sym(zeros(i,j));
r=sym(zeros(2,1,i,j));
C=sym(zeros(2,1));
bd=sym(zeros(2,1));

dr_dz=sym(zeros(2,36,i,j));
dr_dz2=sym(zeros(36,36,i,j));
T=sym(zeros(2,2,i));
m=sym(zeros(36,36,i,j));
M=sym(zeros(36,36));
ks=sym(zeros(4,4,i,j));
K=sym(zeros(36,36));

Cqd=sym(zeros(22,1));
CC=sym(zeros(22,22));

%% States for each element
z(:,1,1,1)=[theta(1);sym(zeros(3,1));u(1,1);v(1,1);u(1,2);v(1,2); ...
   sym(zeros(28,1))]; % [5,6,7,8] are active
z(:,1,1,2)=[theta(1);sym(zeros(5,1));u(1,2);v(1,2);u(1,3);v(1,3); ...
   sym(zeros(26,1))]; % [7,8,9,10] are active
z(:,1,1,3)=sym(zeros(36,1));
z(:,1,2,1)=[sym(0);theta(2);sym(zeros(10,1));u(2,1);v(2,1);u(2,2); ...
   v(2,2);sym(zeros(20,1))]; % [13,14,15,16] are active
z(:,1,2,2)=[sym(0);theta(2);sym(zeros(12,1));u(2,2);v(2,2);u(2,3); ...
   v(2,3);sym(zeros(18,1))]; % [15,16,17,18] are active
z(:,1,2,3)=sym(zeros(36,1));
z(:,1,3,1)=[sym(0);theta(2);theta(3);sym(zeros(13,1));u(2,3);v(2,3); ...
   sym(0);sym(0);u(3,1);v(3,1);u(3,2);v(3,2); ...
   sym(zeros(12,1))]; % [21,22,23,24] are active
z(:,1,3,2)=[sym(0);theta(2);theta(3);sym(zeros(13,1));u(2,3); ...
   v(2,3);sym(zeros(4,1));u(3,2);v(3,2);u(3,3);v(3,3); ...
   sym(zeros(10,1))]; % [23,24,25,26] are active
z(:,1,3,3)=sym(zeros(36,1));
z(:,1,4,1)=[sym(0);theta(2);theta(3);theta(4);sym(zeros(12,1)); ...
   u(2,3);v(2,3);sym(zeros(6,1));u(3,3);v(3,3);sym(0);sym(0); ...
   u(4,1);v(4,1);u(4,2);v(4,2);sym(zeros(4,1))]; % [29,30,31,32] are active
z(:,1,4,2)=[sym(0);theta(2);theta(3);theta(4);sym(zeros(12,1)); ...
   u(2,3);v(2,3);sym(zeros(6,1));u(3,3);v(3,3);sym(zeros(4,1)); ...
   u(4,2);v(4,2);u(4,3);v(4,3);sym(zeros(2,1))]; % [31,32,33,34] are active
z(:,1,4,3)=[sym(0);theta(2);theta(3);theta(4);sym(zeros(12,1)); ...
   u(2,3);v(2,3);sym(zeros(6,1));u(3,3);v(3,3);sym(zeros(6,1)); ...
   u(4,3);v(4,3);u(4,4);v(4,4)]; % [32,33,34,35] are active

%% Generalized Coordinates
c=1;
q(1:4,1)=theta(:);
for i=1:4
    for j=1:4

```

```

        q(c+4:c+5,1)=[u(i,j);v(i,j)];
        c=c+2;
    end
end

%% Shape Functions for each element

fi(1,:,1,1)=[sym(zeros(1,4)), 1-3*x(1,1)^2/l(1,1)^2+2*x(1,1)^3/l(1,1)^3,...
             x(1,1)-2*x(1,1)^2/l(1,1)+x(1,1)^3/l(1,1)^2,...
             3*x(1,1)^2/l(1,1)^2-2*x(1,1)^3/l(1,1)^3,...
             -x(1,1)^2/l(1,1)+x(1,1)^3/l(1,1)^2,sym(zeros(1,28))];

fi(1,:,1,2)=[sym(zeros(1,6)), 1-3*x(1,2)^2/l(1,2)^2+2*x(1,2)^3/l(1,2)^3,...
             x(1,2)-2*x(1,2)^2/l(1,2)+x(1,2)^3/l(1,2)^2,...
             3*x(1,2)^2/l(1,2)^2-2*x(1,2)^3/l(1,2)^3,...
             -x(1,2)^2/l(1,2)+x(1,2)^3/l(1,2)^2,sym(zeros(1,26))];

fi(1,:,2,1)=[sym(zeros(1,12)), 1-3*x(2,1)^2/l(2,1)^2+2*x(2,1)^3/l(2,1)^3,...
             x(2,1)-2*x(2,1)^2/l(2,1)+x(2,1)^3/l(2,1)^2,...
             3*x(2,1)^2/l(2,1)^2-2*x(2,1)^3/l(2,1)^3,...
             -x(2,1)^2/l(2,1)+x(2,1)^3/l(2,1)^2,sym(zeros(1,20))];

fi(1,:,2,2)=[sym(zeros(1,14)), 1-3*x(2,2)^2/l(2,2)^2+2*x(2,2)^3/l(2,2)^3,...
             x(2,2)-2*x(2,2)^2/l(2,2)+x(2,2)^3/l(2,2)^2,...
             3*x(2,2)^2/l(2,2)^2-2*x(2,2)^3/l(2,2)^3,...
             -x(2,2)^2/l(2,2)+x(2,2)^3/l(2,2)^2,sym(zeros(1,18))];

fi(1,:,3,1)=[sym(zeros(1,20)), 1-3*x(3,1)^2/l(3,1)^2+2*x(3,1)^3/l(3,1)^3,...
             x(3,1)-2*x(3,1)^2/l(3,1)+x(3,1)^3/l(3,1)^2,...
             3*x(3,1)^2/l(3,1)^2-2*x(3,1)^3/l(3,1)^3,...
             -x(3,1)^2/l(3,1)+x(3,1)^3/l(3,1)^2,sym(zeros(1,12))];

fi(1,:,3,2)=[sym(zeros(1,22)), 1-3*x(3,2)^2/l(3,2)^2+2*x(3,2)^3/l(3,2)^3,...
             x(3,2)-2*x(3,2)^2/l(3,2)+x(3,2)^3/l(3,2)^2,...
             3*x(3,2)^2/l(3,2)^2-2*x(3,2)^3/l(3,2)^3,...
             -x(3,2)^2/l(3,2)+x(3,2)^3/l(3,2)^2,sym(zeros(1,10))];

fi(1,:,4,1)=[sym(zeros(1,28)), 1-3*x(4,1)^2/l(4,1)^2+2*x(4,1)^3/l(4,1)^3,...
             x(4,1)-2*x(4,1)^2/l(4,1)+x(4,1)^3/l(4,1)^2,...
             3*x(4,1)^2/l(4,1)^2-2*x(4,1)^3/l(4,1)^3,...
             -x(4,1)^2/l(4,1)+x(4,1)^3/l(4,1)^2,sym(zeros(1,4))];

fi(1,:,4,2)=[sym(zeros(1,30)), 1-3*x(4,2)^2/l(4,2)^2+2*x(4,2)^3/l(4,2)^3,...
             x(4,2)-2*x(4,2)^2/l(4,2)+x(4,2)^3/l(4,2)^2,...
             3*x(4,2)^2/l(4,2)^2-2*x(4,2)^3/l(4,2)^3,...
             -x(4,2)^2/l(4,2)+x(4,2)^3/l(4,2)^2,sym(zeros(1,2))];

fi(1,:,4,3)=[sym(zeros(1,32)), 1-3*x(4,3)^2/l(4,3)^2+2*x(4,3)^3/l(4,3)^3,...
             x(4,3)-2*x(4,3)^2/l(4,3)+x(4,3)^3/l(4,3)^2,...
             3*x(4,3)^2/l(4,3)^2-2*x(4,3)^3/l(4,3)^3,...
             -x(4,3)^2/l(4,3)+x(4,3)^3/l(4,3)^2];

fi(1,:,1,3)=sym(zeros(1,36));
fi(1,:,2,3)=sym(zeros(1,36));
fi(1,:,3,3)=sym(zeros(1,36));

```

```

%% Vertical postions of points of elements
for i=1:4
    for j=1:3
        y(i,j)=fi(1, :, i, j)*z(:, 1, i, j);
    end
end

%% Rotation Matrices (?)
a=[theta(1), theta(2), theta(3)+v(2,3), theta(4)+v(3,3)];
for i=1:4
    T(:, :, i)=[cos(a(i)), -sin(a(i)); sin(a(i)), cos(a(i))];
end

%% r: Positions of points for each element
for i=1:4

    for j=1:3

        if i==1

            if j==1
                l1=sym(0);
            else
                l1=l1+1(i, j-1);
            end

            r(:, :, i, j)=T(:, :, i)*[l1+x(i, j); y(i, j)];

        elseif i==2

            if j==1
                l2=sym(0);
            else
                l2=l2+1(i, j-1);
            end

            r(:, :, i, j)=T(:, :, i)*[l2+x(i, j); y(i, j)];

        elseif i==3

            if j==1
                l3=sym(0);
            else
                l3=l3+1(i, j-1);
            end

            r(:, :, i, j)=T(:, :, i-1)*([l2; u(2,3)]+T(:, :, i)*[l3+x(i, j); ...
                y(i, j)]); %u(2,3)=u(2,end)

        elseif i==4

            if j==1
                l4=sym(0);
            else
                l4=l4+1(i, j-1);
            end
        end
    end
end

```

```

                r(:, :, i, j) = T(:, :, i-2) * ([12; u(2,3)] + T(:, :, i-1) * ([13; u(3,3)]
...
                + T(:, :, i) * [14+x(i,j); y(i,j)])); %u(3,3)=u(3,end)
            end
        end
    end
end
%% Constraint
C(:, 1) = subs(r(:, :, 1, 2), x(1, 2), l(1, 2)) - subs(r(:, :, 4, 1), x(4, 1), l(4, 1));
%% Jacobian for Constraint

for c=1:36
    B(c, :) = diff(C(:, 1), q(c, 1)); %36*2
end

Bd(:, :) = diff(B(:, :), t);
bd(:, 1) = diff(C(:, 1), t);

%% dr/dz

for i=1:4
    for j=1:3
        for c=1:36
            if z(c, 1, i, j) ~ 0
                dr_dz(:, c, i, j) = diff(r(:, 1, i, j), z(c, 1, i, j));
            else
                dr_dz(:, c, i, j) = 0;
            end
        end
    end
end

%% dr_dz transpose and its quadratic form
dr_dz_trans = permute(dr_dz, [2, 1, 3, 4]);
for i=1:4
    for j=1:3
        dr_dz2(:, :, i, j) = dr_dz_trans(:, :, i, j) * dr_dz(:, :, i, j);
    end
end
%% (4*2) * (2*4) => 4*4

%% Trapezoid integration for Mass matrix
for i=1:4
    for j=1:3
        for i1=1:36
            for i2=1:36
                m(i1, i2, i, j) = ro * A * (int(dr_dz2(i1, i2, i, j), x(i, j), 0, l(i, j)));
            end
        end
    end
end

%% Assemble Mass Matrices

```

```

for i=1:4
    for j=1:3
        M(:, :)=M(:, :)+m(:, :, i, j);
    end
end
%% Stiffness Matrix and its assemble
d=5;
for i=1:4
    for j=1:3
        ks(:, :, i, j)=E*I*[12/l(i, j)^3,    6/l(i, j)^2, -12/l(i, j)^3,
6/l(i, j)^2; ...
        6/l(i, j)^2,    4/l(i, j),    -6/l(i, j)^2,    2/l(i, j); ...
        -12/l(i, j)^3,    -6/l(i, j)^2,    12/l(i, j)^3,    -6/l(i, j)^2; ...
        6/l(i, j)^2,    2/l(i, j),    -6/l(i, j)^2,    4/l(i, j)];

        K(d:d+3, d:d+3)=K(d:d+3, d:d+3)+ks(:, :, i, j);
        d=d+2;
    end
    d=d+2;
end

%% Eliminating rows and collumns for u,v=0
q([5, 6, 11, 12, 13, 14, 19, 20, 21, 22, 27, 28, 29, 30], :)=[];
B([5, 6, 11, 12, 13, 14, 19, 20, 21, 22, 27, 28, 29, 30], :)=[];
Bd([5, 6, 11, 12, 13, 14, 19, 20, 21, 22, 27, 28, 29, 30], :)=[];

qd(:, :)=diff(q(:, :), t);
qdd(:, :)=diff(qd(:, :), t);
M([5, 6, 11, 12, 13, 14, 19, 20, 21, 22, 27, 28, 29, 30], :)=[];
M(:, [5, 6, 11, 12, 13, 14, 19, 20, 21, 22, 27, 28, 29, 30])=[];
K([5, 6, 11, 12, 13, 14, 19, 20, 21, 22, 27, 28, 29, 30], :)=[];
K(:, [5, 6, 11, 12, 13, 14, 19, 20, 21, 22, 27, 28, 29, 30])=[];

```

I. APDL code for eigenvector extraction from modal FEA-A, section 3.6

The following code corresponds to the cantilever beam specified in appendix C.

! Commands inserted into this file will be executed immediately after the ANSYS /POST1 command.

! Active UNIT system in Workbench when this object was created: Metric (m, kg, N, s, V, A)

! NOTE: Any data that requires units (such as mass) is assumed to be in the consistent solver unit system.

! See Solving Units in the help system for more information.

```
/output,cant4thesis_torque,frq      ! write out frequency list
set,list

/output,term                        ! returns output to terminal
! ***** output eigenvectors
! define nodes for output: forces applied or output displacements
nset,s,node,,1                      ! 1/3
nset,a,node,,2                      ! tip
/output,cant4thesis_torque,eig      ! write out eigenvectors list
*do,i,1,20
    set,,i
    prnsol,dof
*enddo
/output,term
```

The following code corresponds to the 2L2JM specified in appendix D.

! Commands inserted into this file will be executed immediately after the ANSYS /POST1 command.

! Active UNIT system in Workbench when this object was created: Metric (m, kg, N, s, V, A)

! NOTE: Any data that requires units (such as mass) is assumed to be in the consistent solver unit system.

! See Solving Units in the help system for more information.

```
/output,2link_june,frq      ! write out frequency list
set,list
/output,2link_june,eig
*do,I,1,20
SET,,I
esel,s,ename,,184          !152 (joint2)
nsle
nsel,a,node,,2             ! tip
nsel,a,node,,89           ! 1/6
nsel,a,node,,76           ! joint1
prnsol,dof,comp
allsel,all
*enddo
/output,term
```

The following code corresponds to the 5-DOF manipulator specified in appendix B.

! Commands inserted into this file will be executed immediately after the ANSYS /POST1 command.

! Active UNIT system in Workbench when this object was created: Metric (m, kg, N, s, V, A)

! NOTE: Any data that requires units (such as mass) is assumed to be in the consistent solver unit system.

! See Solving Units in the help system for more information.

```
/output,5dof_May,frq      ! write out frequency list to ascii file .frq
```

```
set,list
```

```
/output,5dof_May,eig
```

```
*do,I,1,30
```

```
SET,,I
```

```
esel,s,ename,,184
```

```
NSLE
```

```
nsel,a,node,,25034 !base
```

```
nsel,a,node,,53705 !mid
```

```
nsel,a,node,,171337 !tip
```

```
prnsol,dof,comp
```

```
allsel,all
```

```
*enddo
```

```
/output,term
```

J. Transposed Modal Matrices for the manipulators, section 3.6

Table J.1 is the result of the APDL code for eigenvector extraction that is represented in Appendix I. This table corresponds to modal matrix of the Cantilever beam.

Table J.1. Cantilever beam transposed modal matrix

	Tip (vertical displacement)	L/3 (rotational displacement)
Mode 1	2.26	1.19
Mode 2	2.26	-5.04
Mode 3	2.26	8.34
Mode 4	2.25	-6.23
Mode 5	2.25	-2.57
Mode 6	2.25	16.14
Mode 7	2.25	-29.71
Mode 8	2.24	37.35
Mode 9	2.24	-34.24
Mode 10	2.23	18.8
Mode 11	2.23	6.22
Mode 12	2.22	-34.07
Mode 13	2.22	55.9
Mode 14	2.21	-63.55
Mode 15	2.21	52.46
Mode 16	2.2	-23.66
Mode 17	2.2	-15.96
Mode 18	2.19	55.26
Mode 19	2.19	-82.01
Mode 20	2.18	86.73

Table J.2 is the result of the APDL code for eigenvector extraction that is represented in Appendix I. This table corresponds to modal matrix of the 2L2JM.

Table J.2. 2L2JM transposed modal matrix

	Tip (vertical displacement)	Hinge (rotational displacement)	L/6 (vertical displacement)	Middle joint (rotational displacement)
Mode 1	1.15	-1.44	-0.47	2.59
Mode 2	1.74	0.33	0.11	1.42
Mode 3	-1.01	-4.77	-1.24	0.84
Mode 4	-2.01	3.19	0.69	8.48
Mode 5	1.04	9.27	1.21	1.76
Mode 6	2.00	-5.57	-0.47	14.69
Mode 7	-1.04	-13.69	0.00	2.59
Mode 8	-2.00	7.85	-0.24	20.73
Mode 9	1.04	18.1	-1.21	3.42
Mode 10	2.00	-10.12	0.72	26.75
Mode 11	-1.03	-22.47	1.26	4.23
Mode 12	-2.00	12.38	-0.51	32.73
Mode 13	1.03	26.81	-0.12	5.04
Mode 14	2.00	-14.62	-0.18	38.68
Mode 15	-1.03	-31.10	-1.14	5.82
Mode 16	-1.99	16.84	0.70	44.58
Mode 17	1.03	35.35	1.31	6.60
Mode 18	1.99	-19.03	-0.55	50.43
Mode 19	-1.03	-39.55	-0.24	7.35
Mode 20	-1.99	21.20	-0.12	56.23

Table J.3 is the result of the APDL code for eigenvector extraction that is represented in Appendix I. This table corresponds to modal matrix of the 5-DOF manipulator.

Table J.3. 5-DOF manipulator transposed modal matrix. Master DOFs are specified in section 3.6

	DOF 1	DOF 2	DOF 3	DOF 4	DOF 5	DOF 6	DOF 7	DOF 8
Mode 1	0.11	0.11	0.11	0	0	0	0	0
Mode 2	-0.06	0.24	0.24	0	0.31	0	0.31	0
Mode 3	0	0	-0.01	-0.01	0.01	0.01	0.01	-0.01
Mode 4	-0.01	-0.2	-0.52	-0.37	0.16	-0.37	0.15	-0.37
Mode 5	0	-0.04	-0.01	-0.09	0	-0.1	0	-0.08
Mode 6	-0.01	-0.28	0.22	-0.87	0.04	-0.88	-0.04	-0.79
Mode 7	-0.01	0.07	0.45	-0.56	0	-0.64	-0.09	-0.46
Mode 8	0	0.04	0.1	-0.26	0.04	-0.09	-0.04	-0.17
Mode 9	-0.01	0.4	-0.45	-0.54	0.09	-0.77	-0.21	-0.37
Mode 10	0	-0.21	0.23	0.13	-0.1	-0.03	-0.03	-0.13
Mode 11	0	-0.03	0.04	-0.05	-0.01	-0.01	-0.02	-0.06
Mode 12	0	0.12	-0.13	-0.21	0.03	-0.02	0.01	-0.09
Mode 13	0	-0.01	0.2	0.07	0.05	0.14	0.07	0.03
Mode 14	0	-0.02	0	0.5	0.97	0.25	-0.01	0.41
Mode 15	0	-0.06	0.15	1.1	1.88	0.39	0.02	0.62
Mode 16	0	-0.01	0.05	0.19	-0.06	-0.1	0.02	-0.07
Mode 17	0	0	0.33	-0.71	-0.59	-0.22	-0.09	0.06
Mode 18	0	0.01	-0.02	0.59	-1.04	-0.58	0.05	-0.32
Mode 19	-0.02	0.03	0.03	3.48	-1.36	-1.89	0.29	-2.34
Mode 20	0	0.03	0.09	0.51	-0.28	-0.37	-0.02	-0.16
Mode 21	0	0.03	-0.09	-0.08	0.09	0.06	-0.01	0.08
Mode 22	-0.01	-0.17	-0.1	0.4	-0.23	-0.35	0.17	-0.59
Mode 23	0	0	-0.16	0.3	-0.14	-0.19	0.06	-0.38
Mode 24	0	0.01	0	0.49	0.24	-0.1	0.11	-0.85
Mode 25	0	-0.2	0.21	0.04	-0.12	-0.05	-0.14	0.29
Mode 26	-0.02	0.18	0.16	0.68	1.05	0.35	0.67	-2.2
Mode 27	0	-0.07	-0.06	0.06	-0.06	-0.06	-0.06	-0.08
Mode 28	-0.01	-0.42	-0.38	2.06	0.93	-0.11	0.15	-0.87
Mode 29	0	0.19	0.21	2.79	0.64	-0.76	-0.05	0.93
Mode 30	0	0.08	0.06	1.8	0.42	-0.48	-0.07	0.58



K. State-space matrices for the Cantilever beam, section 3.6, 3.7, and 4.2

The 5-DOF manipulator modal matrix was an 8 by 30 matrix, which the resulting state-space matrices based on section 3.3 for the full order model is as follows:

$$A_{40 \times 40}^{\text{full_order}}, \quad B_{40 \times 1}^{\text{full_order}}, \quad C_{1 \times 40}^{\text{full_order}}$$

For the Truncated model, only the first 5 modes from the full order model were taken.

$$A_{4 \times 4}^{\text{Truncated}}, \quad B_{4 \times 1}^{\text{Truncated}}, \quad C_{1 \times 4}^{\text{Truncated}}$$

For the BMDC, first the full order was balanced then the first 5 modes from the full order model were taken.

$$A_{4 \times 4}^{\text{BMDC}}, \quad B_{4 \times 1}^{\text{BMDC}}, \quad C_{1 \times 4}^{\text{BMDC}}$$

The state-space matrices were given in the following. Since the state matrix for the full order was large, it was broken to 10 by 10 chunks. Not mentioned elements are zero.

$$A_{[1:10,1:10]}^{full_order} =$$

0	1	0	0	0	0	0	0	0	0
-2624	-0.01	0	0	0	0	0	0	0	0
0	0	0	1	0	0	0	0	0	0
0	0	-102969	-0.03	0	0	0	0	0	0
0	0	0	0	0	1	0	0	0	0
0	0	0	0	-806052	-0.09	0	0	0	0
0	0	0	0	0	0	0	1	0	0
0	0	0	0	0	0	-3088479	-0.18	0	0
0	0	0	0	0	0	0	0	0	1
0	0	0	0	0	0	0	0	-8415856	-0.29

$$A_{[11:20,11:20]}^{full_order} =$$

0	1	0	0	0	0	0	0	0	0
-18715130	-0.43	0	0	0	0	0	0	0	0
0	0	0	1	0	0	0	0	0	0
0	0	-36359815	-0.6	0	0	0	0	0	0
0	0	0	0	0	1	0	0	0	0
0	0	0	0	-64146905	-0.8	0	0	0	0
0	0	0	0	0	0	0	1	0	0
0	0	0	0	0	0	-105289556	-1.03	0	0
0	0	0	0	0	0	0	0	0	1
0	0	0	0	0	0	0	0	-163360493	-1.28

$$A_{[21:30,21:30]}^{full_order} =$$

0	1	0	0	0	0	0	0	0	0
-2.4E+08	-1.56	0	0	0	0	0	0	0	0
0	0	0	1	0	0	0	0	0	0
0	0	-3.5E+08	-1.86	0	0	0	0	0	0
0	0	0	0	0	1	0	0	0	0
0	0	0	0	-4.8E+08	-2.19	0	0	0	0
0	0	0	0	0	0	0	1	0	0
0	0	0	0	0	0	-6.5E+08	-2.55	0	0
0	0	0	0	0	0	0	0	0	1
0	0	0	0	0	0	0	0	-8.6E+08	-2.93

$$A_{[31:40,31:40]}^{full_order} =$$

0	1	0	0	0	0	0	0	0	0
-1.1E+09	-3.33	0	0	0	0	0	0	0	0
0	0	0	1	0	0	0	0	0	0
0	0	-1.4E+09	-3.76	0	0	0	0	0	0
0	0	0	0	0	1	0	0	0	0
0	0	0	0	-1.8E+09	-4.21	0	0	0	0
0	0	0	0	0	0	0	1	0	0
0	0	0	0	0	0	-2.2E+09	-4.69	0	0
0	0	0	0	0	0	0	0	0	1
0	0	0	0	0	0	0	0	-2.7E+09	-5.19

$$B_{[1:40,1]}^{full_order} =$$

0
1.19
0
-5.04
0
8.34
0
-6.23
0
-2.57
0
16.14
0
-29.71
0
37.35
0
-34.24
0
18.8
0
6.22
0
-34.07
0
55.9
0
-63.55
0
52.46
0
-23.66
0
-15.96
0
55.26
0
-82.01
0
86.73

$$C_{[1,1:10]}^{fullorder} =$$

2.26	0	2.26	0	2.26	0	2.25	0	2.25	0
------	---	------	---	------	---	------	---	------	---

$$C_{[1,11:20]}^{fullorder} =$$

2.25	0	2.25	0	2.24	0	2.24	0	2.23	0
------	---	------	---	------	---	------	---	------	---

$$C_{[1,21:30]}^{fullorder} =$$

2.23	0	2.22	0	2.22	0	2.21	0	2.21	0
------	---	------	---	------	---	------	---	------	---

$$C_{[1,31:40]}^{fullorder} =$$

2.2	0	2.2	0	2.19	0	2.19	0	2.18	0
-----	---	-----	---	------	---	------	---	------	---

$$A_{4 \times 4}^{Truncated} =$$

0	1	0	0
-2624	-0.01	0	0
0	0	0	1
0	0	-102969	-0.03

$$B_{4 \times 1}^{Truncated} =$$

0
1.19
0
-5.04

$$C_{1 \times 4}^{Truncated} =$$

2.26	0	2.26	0
------	---	------	---

$$A_{4 \times 4}^{BMDC} =$$

0	51.23	0	0
-51.23	0	0	0
0	0	-0.02	-320.89
0	0	320.89	-0.02

$$B_{4 \times 1}^{BMDC} =$$

-0.16
-0.16
0.13
-0.13

$$C_{1 \times 4}^{BMDC} =$$

-0.16	0.16	-0.13	-0.13
-------	------	-------	-------

L. State-space matrices for the 2L2JM, section 3.6, 3.8, and 4.4

The 5-DOF manipulator modal matrix was an 8 by 30 matrix, which the resulting state-space matrices based on section 3.3 for the full order model is as follows:

$$A_{40 \times 40}^{\text{full_order}}, \quad B_{40 \times 3}^{\text{full_order}}, \quad C_{1 \times 40}^{\text{full_order}}$$

For the Truncated model, only the first 5 modes from the full order model were taken.

$$A_{8 \times 8}^{\text{Truncated}}, \quad B_{8 \times 3}^{\text{Truncated}}, \quad C_{1 \times 8}^{\text{Truncated}}$$

For the BMDC, first the full order was balanced then the first 5 modes from the full order model were taken.

$$A_{8 \times 8}^{\text{BMDC}}, \quad B_{8 \times 3}^{\text{BMDC}}, \quad C_{1 \times 8}^{\text{BMDC}}$$

The state-space matrices were given in the following. Since the state matrix for the full order was large, it was broken to 10 by 10 chunks. Not mentioned elements are zero.

$$A_{[1:10,1:10]}^{full_order} =$$

0	1	0	0	0	0	0	0	0	0
0	0	0	0	0	0	0	0	0	0
0	0	0	1	0	0	0	0	0	0
0	0	-1	0	0	0	0	0	0	0
0	0	0	0	0	1	0	0	0	0
0	0	0	0	-28137	-0.02	0	0	0	0
0	0	0	0	0	0	0	1	0	0
0	0	0	0	0	0	-84213	-0.03	0	0
0	0	0	0	0	0	0	0	0	1
0	0	0	0	0	0	0	0	-389135	-0.06

$$A_{[11:20,11:20]}^{full_order} =$$

0	1	0	0	0	0	0	0	0	0
-703910	-0.08	0	0	0	0	0	0	0	0
0	0	0	1	0	0	0	0	0	0
0	0	-1863285	-0.14	0	0	0	0	0	0
0	0	0	0	0	1	0	0	0	0
0	0	0	0	-2807424	-0.17	0	0	0	0
0	0	0	0	0	0	0	1	0	0
0	0	0	0	0	0	-5718098	-0.24	0	0
0	0	0	0	0	0	0	0	0	1
0	0	0	0	0	0	0	0	-7819470	-0.28

$$A_{[21:30,21:30]}^{full_order} =$$

0	1	0	0	0	0	0	0	0	0
-1.4E+07	-0.37	0	0	0	0	0	0	0	0
0	0	0	1	0	0	0	0	0	0
0	0	-1.8E+07	-0.42	0	0	0	0	0	0
0	0	0	0	0	1	0	0	0	0
0	0	0	0	-2.8E+07	-0.53	0	0	0	0
0	0	0	0	0	0	0	1	0	0
0	0	0	0	0	0	-3.5E+07	-0.59	0	0
0	0	0	0	0	0	0	0	0	1
0	0	0	0	0	0	0	0	-5.1E+07	-0.72

$$A_{[31:40,31:40]}^{full_order} =$$

0	1	0	0	0	0	0	0	0	0
-6.1E+07	-0.78	0	0	0	0	0	0	0	0
0	0	0	1	0	0	0	0	0	0
0	0	-8.6E+07	-0.93	0	0	0	0	0	0
0	0	0	0	0	1	0	0	0	0
0	0	0	0	-1E+08	-1.01	0	0	0	0
0	0	0	0	0	0	0	1	0	0
0	0	0	0	0	0	-1.4E+08	-1.17	0	0
0	0	0	0	0	0	0	0	0	1
0	0	0	0	0	0	0	0	-1.6E+08	-1.26

$$B_{[140,1:3]}^{full_order} =$$

0	0	0
0.69	0.22	0.69
0	0	0
-1.31	-0.42	2.87
0	0	0
-4.77	-1.24	0.84
0	0	0
3.19	0.69	8.48
0	0	0
9.27	1.21	1.76
0	0	0
-5.57	-0.47	14.69
0	0	0
-13.69	0	2.59
0	0	0
7.85	-0.24	20.73
0	0	0
18.1	-1.21	3.42
0	0	0
-10.13	0.72	26.75
0	0	0
-22.47	1.26	4.23
0	0	0
12.38	-0.51	32.73
0	0	0
26.81	-0.12	5.04
0	0	0
-14.62	-0.18	38.68
0	0	0
-31.1	-1.14	5.83
0	0	0
16.84	0.7	44.58
0	0	0
35.35	1.31	6.6
0	0	0
-19.03	-0.55	50.43
0	0	0
-39.55	-0.24	7.35
0	0	0
21.2	-0.12	56.23

$$C_{[1,1:10]}^{fullorder} =$$

1.38	0	1.57	0	-1.01	0	-2.01	0	1.04	0
------	---	------	---	-------	---	-------	---	------	---

$$C_{[1,11:20]}^{fullorder} =$$

2	0	-1.04	0	-2	0	1.04	0	2	0
---	---	-------	---	----	---	------	---	---	---

$$C_{[1,21:30]}^{fullorder} =$$

-1.03	0	-2	0	1.03	0	2	0	-1.03	0
-------	---	----	---	------	---	---	---	-------	---

$$C_{[1,31:40]}^{fullorder} =$$

-1.99	0	1.03	0	1.99	0	-1.03	0	-1.99	0
-------	---	------	---	------	---	-------	---	-------	---

$$A_{8 \times 8}^{Truncated} =$$

0	1	0	0	0	0	0	0
0	0	0	0	0	0	0	0
0	0	0	1	0	0	0	0
0	0	-1	0	0	0	0	0
0	0	0	0	0	1	0	0
0	0	0	0	-28137	-0.02	0	0
0	0	0	0	0	0	0	1
0	0	0	0	0	0	-84213	-0.03

$$B_{8 \times 3}^{Truncated} =$$

0	0	0
0.69	0.22	0.69
0	0	0
-1.31	-0.42	2.87
0	0	0
-4.77	-1.24	0.84
0	0	0
3.19	0.69	8.48

$$C_{1 \times 8}^{Truncated} =$$

1.38	0	1.57	0	-1.01	0	-2.01	0	1.38	0
------	---	------	---	-------	---	-------	---	------	---

$$A_{8 \times 8}^{BMD C} =$$

0	1	0	0	0	0	0	0
0	0	0	0	0	0	0	0
0	0	0	1	0	0	0	0
0	0	-1	0	0	0	0	0
0	0	0	0	-0.01	-290.2	-0.07	-0.05
0	0	0	0	290.2	-0.01	-0.05	-0.07
0	0	0	0	0.06	0.04	-0.01	-167.74
0	0	0	0	0.04	0.06	167.74	-0.01

$$B_{8 \times 3}^{BMD C} =$$

0	0	0
0.69	0.22	0.69
0	0	0
-1.31	-0.42	2.87
-0.06	-0.01	-0.17
0.06	0.01	0.17
0.12	0.03	-0.02
-0.12	-0.03	0.02

$$C_{1 \times 8}^{BMD C} =$$

1.38	0	1.57	0	0.18	0.18	0.12	0.12	1.38	0
------	---	------	---	------	------	------	------	------	---

M. State-space matrices for the 5-DOF manipulator, section 3.6, 3.9, and 4.5

The 5-DOF manipulator modal matrix was an 8 by 30 matrix, which the resulting state-space matrices based on section 3.3 for the full order model is as follows:

$$A_{60 \times 60}^{\text{full_order}}, \quad B_{60 \times 3}^{\text{full_order}}, \quad C_{1 \times 60}^{\text{full_order}}$$

For the Truncated model, only the first 5 modes from the full order model were taken.

$$A_{10 \times 10}^{\text{Truncated}}, \quad B_{10 \times 3}^{\text{Truncated}}, \quad C_{1 \times 10}^{\text{Truncated}}$$

For the BMDC, first the full order was balanced then the first 5 modes from the full order model were taken.

$$A_{10 \times 10}^{\text{BMDC}}, \quad B_{10 \times 3}^{\text{BMDC}}, \quad C_{1 \times 10}^{\text{BMDC}}$$

The state-space matrices were given in the following. Since the state matrix for the full order was large, it was broken to 10 by 10 chunks. Not mentioned elements are zero.

$$A_{[1:10,1:10]}^{full_order} =$$

0	1	0	0	0	0	0	0	0	0
0	0	0	0	0	0	0	0	0	0
0	0	0	1	0	0	0	0	0	0
0	0	-0.63	0	0	0	0	0	0	0
0	0	0	0	0	1	0	0	0	0
0	0	0	0	-2722.88	-0.01	0	0	0	0
0	0	0	0	0	0	0	1	0	0
0	0	0	0	0	0	-3521.79	-0.01	0	0
0	0	0	0	0	0	0	0	0	1
0	0	0	0	0	0	0	0	-19119.7	-0.01

$$A_{[11:20,11:20]}^{full_order} =$$

0	1	0	0	0	0	0	0	0	0
-24015.2	-0.02	0	0	0	0	0	0	0	0
0	0	0	1	0	0	0	0	0	0
0	0	-50792.4	-0.02	0	0	0	0	0	0
0	0	0	0	0	1	0	0	0	0
0	0	0	0	-89426.1	-0.03	0	0	0	0
0	0	0	0	0	0	0	1	0	0
0	0	0	0	0	0	-113272	-0.03	0	0
0	0	0	0	0	0	0	0	0	1
0	0	0	0	0	0	0	0	-141706	-0.04

$$A_{[21:30,21:30]}^{full_order} =$$

0	1	0	0	0	0	0	0	0	0
-153399	-0.04	0	0	0	0	0	0	0	0
0	0	0	1	0	0	0	0	0	0
0	0	-166248	-0.04	0	0	0	0	0	0
0	0	0	0	0	1	0	0	0	0
0	0	0	0	-244890	-0.05	0	0	0	0
0	0	0	0	0	0	0	1	0	0
0	0	0	0	0	0	-424375	-0.07	0	0
0	0	0	0	0	0	0	0	0	1
0	0	0	0	0	0	0	0	-447438	-0.07

$$A_{[31:40,31:40]}^{full_order} =$$

0	1	0	0	0	0	0	0	0	0
-525103	-0.07	0	0	0	0	0	0	0	0
0	0	0	1	0	0	0	0	0	0
0	0	-557739	-0.07	0	0	0	0	0	0
0	0	0	0	0	1	0	0	0	0
0	0	0	0	-643786	-0.08	0	0	0	0
0	0	0	0	0	0	0	1	0	0
0	0	0	0	0	0	-845446	-0.09	0	0
0	0	0	0	0	0	0	0	0	1
0	0	0	0	0	0	0	0	-907076	-0.1

$$A_{[41:50,41:50]}^{full_order} =$$

0	1	0	0	0	0	0	0	0	0
-998431	-0.1	0	0	0	0	0	0	0	0
0	0	0	1	0	0	0	0	0	0
0	0	-1102860	-0.11	0	0	0	0	0	0
0	0	0	0	0	1	0	0	0	0
0	0	0	0	-1205851	-0.11	0	0	0	0
0	0	0	0	0	0	0	1	0	0
0	0	0	0	0	0	-1447158	-0.12	0	0
0	0	0	0	0	0	0	0	0	1
0	0	0	0	0	0	0	0	-1665886	-0.13

$$A_{[51:60,51:60]}^{full_order} =$$

0	1	0	0	0	0	0	0	0	0
-1861913	-0.14	0	0	0	0	0	0	0	0
0	0	0	1	0	0	0	0	0	0
0	0	-2050626	-0.14	0	0	0	0	0	0
0	0	0	0	0	1	0	0	0	0
0	0	0	0	-2169447	-0.15	0	0	0	0
0	0	0	0	0	0	0	1	0	0
0	0	0	0	0	0	-2464836	-0.16	0	0
0	0	0	0	0	0	0	0	0	1
0	0	0	0	0	0	0	0	-2478665	-0.16

$$B_{[1:30,1:3]}^{full_order} =$$

0	0	0
0.11	0	0
0	0	0
-0.06	0	0.31
0	0	0
0	0.01	0.01
0	0	0
-0.01	-0.37	0.15
0	0	0
0	-0.1	0
0	0	0
-0.01	-0.88	-0.04
0	0	0
-0.01	-0.64	-0.09
0	0	0
0	-0.09	-0.04
0	0	0
-0.01	-0.77	-0.21
0	0	0
0	-0.03	-0.03
0	0	0
0	-0.01	-0.02
0	0	0
0	-0.02	0.01
0	0	0
0	0.14	0.07
0	0	0
0	0.25	-0.01
0	0	0
0	0.39	0.02

$$B_{[31:60,1:3]}^{full_order} =$$

0	0	0
0	-0.1	0.02
0	0	0
0	-0.22	-0.09
0	0	0
0	-0.58	0.05
0	0	0
-0.02	-1.89	0.29
0	0	0
0	-0.37	-0.02
0	0	0
0	0.06	-0.01
0	0	0
-0.01	-0.35	0.17
0	0	0
0	-0.19	0.06
0	0	0
0	-0.1	0.11
0	0	0
0	-0.05	-0.14
0	0	0
-0.02	0.35	0.67
0	0	0
0	-0.06	-0.06
0	0	0
-0.01	-0.11	0.15
0	0	0
0	-0.76	-0.05
0	0	0
0	-0.48	-0.07

$$C_{[1,1:10]}^{fullorder} =$$

0.11	0	0.24	0	-0.01	0	-0.52	0	-0.01	0
------	---	------	---	-------	---	-------	---	-------	---

$$C_{[1,11:20]}^{fullorder} =$$

0.22	0	0.45	0	0.1	0	-0.45	0	0.23	0
------	---	------	---	-----	---	-------	---	------	---

$$C_{[1,21:30]}^{fullorder} =$$

0.04	0	-0.13	0	0.2	0	0	0	0.15	0
------	---	-------	---	-----	---	---	---	------	---

$$C_{[1,31:40]}^{fullorder} =$$

0.05	0	0.33	0	-0.02	0	0.03	0	0.09	0
------	---	------	---	-------	---	------	---	------	---

$$C_{[1,41:50]}^{fullorder} =$$

-0.09	0	-0.1	0	-0.16	0	0	0	0.21	0
-------	---	------	---	-------	---	---	---	------	---

$$C_{[1,51:60]}^{fullorder} =$$

0.16	0	-0.06	0	-0.38	0	0.21	0	0.06	0
------	---	-------	---	-------	---	------	---	------	---

$$A_{10 \times 10}^{Truncated} =$$

0	1	0	0	0	0	0	0	0	0
0	0	0	0	0	0	0	0	0	0
0	0	0	1	0	0	0	0	0	0
0	0	-0.63	0	0	0	0	0	0	0
0	0	0	0	0	1	0	0	0	0
0	0	0	0	-2722	-0.21	0	0	0	0
0	0	0	0	0	0	0	1	0	0
0	0	0	0	0	0	-3521	-0.24	0	0
0	0	0	0	0	0	0	0	0	1
0	0	0	0	0	0	0	0	-19119	-0.55

$$B_{10 \times 3}^{Truncated} =$$

0	0	0
0.11	0	0
0	0	0
-0.06	0	0.31
0	0	0
0	0.01	0.01
0	0	0
-0.01	-0.37	0.15
0	0	0
0	-0.1	0

$$C_{1 \times 10}^{Truncated} =$$

0.11	0	0.24	0	-0.01	0	-0.52	0	-0.01	0
------	---	------	---	-------	---	-------	---	-------	---

$$A_{10 \times 10}^{BMDC} =$$

0	1	0	0	0	0	0	0	0	0
0	0	0	0	0	0	0	0	0	0
0	0	0	1	0	0	0	0	0	0
0	0	-0.63	0	0	0	0	0	0	0
0	0	0	0	0	1	0	0	0	0
0	0	0	0	-3521	-0.01	0	0	0	0
0	0	0	0	0	0	-0.01	155	0.01	0.05
0	0	0	0	0	0	-155	-0.01	-0.05	-0.01
0	0	0	0	0	0	0.01	0.05	-0.01	-225
0	0	0	0	0	0	-0.05	-0.01	225	-0.01

$$B_{10 \times 3}^{BMDC} =$$

0	0	0
0.11	0	0
0	0	0
-0.06	0	0.31
0	0	0
-0.01	-0.37	0.15
0	0.03	0
0	0.03	0
0	-0.03	0
0	0.03	0

$$C_{1 \times 10}^{BMDC} =$$

0.11	0	0.24	0	-0.52	0	-0.03	0.03	0.03	0.03
------	---	------	---	-------	---	-------	------	------	------

N. LQR formulation, section 4.1

Let's assume the dynamics of the system has a linear time variant model as follows:

$$\dot{X} = A(t)X + B(t)U, \quad X \in \mathbf{R}^n, \quad U \in \mathbf{R}^m, \quad t \in [t_0, t_1] \quad \text{N} - 1$$

that we want to minimize a quadratic cost function:

$$J(U) = X^T(t_1)Q(t_1)X(t_1) + \int_{t_0}^{t_1} (X^T Q(t)X + U^T R(t)U) dt, \quad Q(t) \geq 0, \quad R(t) > 0 \quad \text{N} - 2$$

where the first part is called terminal cost and is denoted as Φ :

$$\Phi = X^T(t_1)Q(t_1)X(t_1) \quad \text{N} - 3$$

and the second part is called the running cost and is denoted as \mathcal{L} :

$$\mathcal{L} = X^T Q(t)X + U^T R(t)U \quad \text{N} - 4$$

To solve the optimization problem, Hamiltonian is defined which could be considered as the energy of the system.

$$H := \mathcal{L} + \lambda^T \mathcal{F} = X^T Q X + U^T R U + \lambda^T (A X + B U), \quad \lambda \in \mathbf{R}^n \quad \text{N} - 5$$

where \mathcal{L} is called Lagrangian which is the running cost function. Besides, \mathcal{F} is the dynamics of the system and λ is the Lagrange multiplier.

From calculus of variations, one could end up with the necessary conditions for the optimization problem as follows:

$$\left\{ \begin{array}{l} \frac{\partial H}{\partial \lambda} = \dot{X} \\ \frac{\partial H}{\partial X} = -\dot{\lambda} \\ \frac{\partial H}{\partial U} = 0 \\ \frac{\partial \Phi(t_1)}{\partial X(t_1)} = \lambda(t_1) \end{array} \right. \quad \text{N - 6}$$

These conditions are simplified as follows:

$$\left\{ \begin{array}{l} A X + B U = \dot{X} \\ Q X + \lambda^T A = -\dot{\lambda} \\ R U + B \lambda^T = 0 \\ Q(t_1)X(t_1) = \lambda(t_1) \end{array} \right. \quad \text{N - 7}$$

The first condition is the state equation which is trivial. The second condition is called costate condition. The fourth condition is called transversality condition. The third condition is called stationarity that leads to the optimal control law as follows:

$$U = -R^{-1}B^T \lambda \quad \text{N - 8}$$

To solve equation N-8, λ needs to be found. Based on the following assumption:

$$\lambda(t) = P(t)X(t), \quad t \in [t_0, t_1] \quad \text{N - 9}$$

if we take the derivative of λ with respect to time:

$$\dot{\lambda} = \dot{P}X + \dot{X}P \quad \text{N - 10}$$

By substituting equations N-1 and N-8 into equation N-10:

$$\dot{\lambda} = [\dot{P} + PA - PBR^{-1}B^T P]X, \quad \forall X \in \mathbf{R}^n \quad \text{N - 11}$$

Now we could use the second condition in N-7 instead of $\dot{\lambda}$. This would end up as the the following equation which is called the differential Ricatti equation.

$$-\dot{P} = PA + A^T P - PBR^{-1}B^T P + Q \quad \text{N - 12}$$

where the boundary condition is from the fourth condition in L-7:

$$P(t_1) = Q(t_1) \quad \text{N - 13}$$

By solving P from equation N-12, and substituting equation N-9 in N-8, the following control law could be found:

$$U = -R^{-1}B^T P X \quad \text{N - 14}$$

O. H_∞ controller for vibration damping of manipulators, section 4.3, 4.4, and 4.5

This section is devoted to explanation of H_∞ controller concept. According to [41], a closed loop feedback system as shown in Figure O.1 is internally stable if and only if all the transfer functions in equation (O.1 to O.4) are BIBO stable (bounded input bounded output), *i.e.*, the bounded inputs must have bounded outputs. This happens when the transfer functions have two conditions. First, the denominator has higher order than the numerator. Second, the poles are on the left-hand plane of the s -space.

$$T_{yr}(s) =: \frac{Y(s)}{R(s)} = K_c(s)G(s)(I + G(s)K_c(s))^{-1} \quad \text{O-1}$$

$$T_{yd}(s) =: \frac{Y(s)}{D(s)} = G(s)(I + K_c(s)G(s))^{-1} \quad \text{O-2}$$

$$T_{ur}(s) =: \frac{U(s)}{R(s)} = K_c(s)(I + G(s)K_c(s))^{-1} \quad \text{O-3}$$

$$T_{ud}(s) =: \frac{U(s)}{D(s)} = -K_c(s)G(s)(I + K_c(s)G(s))^{-1} \quad \text{O-4}$$

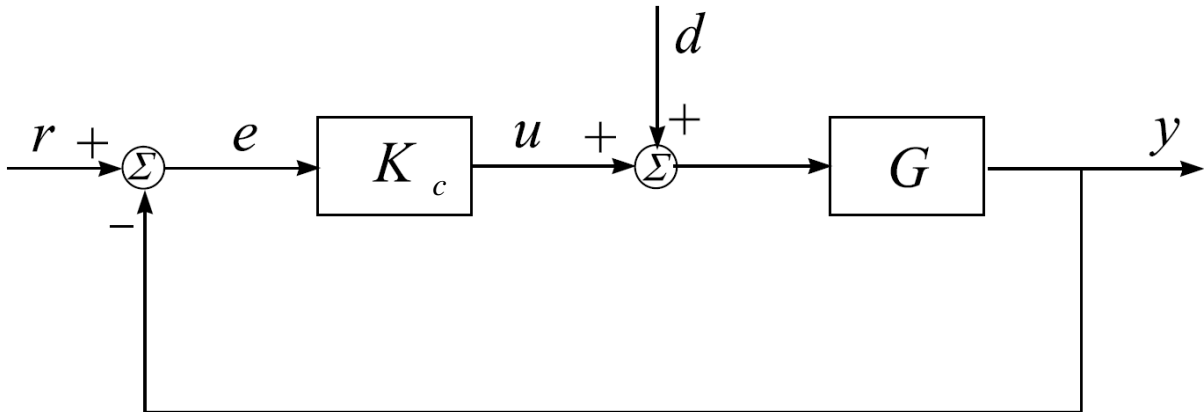


Figure O.1. A closed loop system with feedback [34]. { r : reference, e : error, u : control input, d : disturbance, y : output, K_c : controller transfer function, G : plant transfer function}

If the nominal system is internally stable, it can meet the required performance (nominal performance). The ability for tracking is defined by the transfer function from r to e .

$$T_{er}(s) =: \frac{E(s)}{R(s)} = (I + G(s)K(s))^{-1} \quad 0 - 5$$

This transfer function is called sensitivity and it is represented by S . To have good tracking performance in a certain frequency ω , the sensitivity magnitude should be less than a small positive value:

$$|S(j\omega)| < \epsilon(\omega) \quad 0 - 6$$

The inequality can be normalized with a weighting function $W_s(\omega) = 1/\epsilon(\omega)$:

$$|S(j\omega)W_s(j\omega)| < 1 \quad 0 - 7$$

This inequality over the entire frequency domain could be shown as below:

$$\|S W_s\|_\infty < 1 \quad 0 - 8$$

In inequality (O-8), $\|\cdot\|_\infty$ stands for infinity norm, which is defined as follows:

$$\|G\|_\infty = \sup_{\omega \in R} \|G(j\omega)\|_2 \quad 0 - 9$$

Infinity norm of a system is also called H_∞ norm of the system. It describes the maximum energy gain of the system and is decided by the peak value of the largest singular value of the

frequency response matrix over the whole frequency axis [41]. This ensures that the system at any frequency would track the reference.

In the definition of H^∞ norm of the system in (O-9), $\| \cdot \|_2$ stands for the second norm, which is defined as follows:

$$\|G\|_2 = \left[\frac{1}{2\pi} \int_{-\infty}^{+\infty} |G(j\omega)|^2 d\omega \right]^{\frac{1}{2}} \quad O - 10$$

Similarly, for efficient actuator performance, the transfer function in equation (O-4) should be as follows:

$$\|KS W_u\|_\infty < 1 \quad O - 11$$

The H^∞ controller is a multi-objective controller that solves an optimization problem between different control criteria. Therefore, the inequalities (O-8 and O-11) could be written as follows:

$$\min_K \left\| \begin{matrix} S W_s \\ KS W_u \end{matrix} \right\|_\infty \quad O - 12$$

For better demonstration, Figure O.1 could be recast into standard configuration.

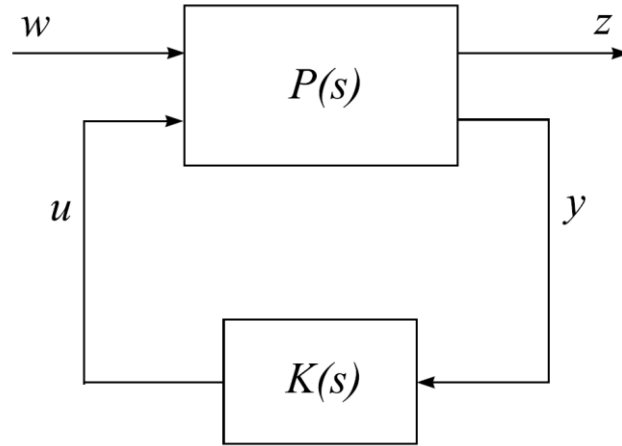


Figure O.2. The standard H_∞ configuration [34]. { w : external input, z : outputs to be minimized, u : control input, y : measured output, $P(s)$: generalized system transfer function, $K(s)$: controller transfer function}

According to Figure O.2, w denotes the external inputs such as the reference, noise, and disturbance. On the other hand, z denotes the output signals to be minimized. The objective is to find a stabilizing controller to minimize the output z . The generalized system P is defined as:

$$\begin{bmatrix} z \\ y \end{bmatrix} = \begin{bmatrix} P_{11} & P_{12} \\ P_{21} & P_{22} \end{bmatrix} \begin{bmatrix} w \\ u \end{bmatrix} \quad \text{O-13}$$

By substituting $u = Ky$ in the system of equations (O-13) and removing y , one could end up having z as:

$$\begin{aligned} z &= [P_{11} + P_{12}K(I - P_{22}K)^{-1}P_{21}]w \\ &:= \mathcal{F}_l(P, K)w \end{aligned} \quad \text{O-14}$$

where $\mathcal{F}_l(P, K)$ is called lower linear fractional transformation of P and K . The design objective becomes:

$$\min_K \|\mathcal{F}_l(P, K)\|_\infty \quad 0 - 15$$

which is called H_∞ optimization problem. The H_∞ norm is usually computed numerically from a state-space realization. The smallest value of γ is found so that the Hamiltonian matrix equation (O-16) has no eigenvalues on the imaginary axis [46].

$$H = \begin{bmatrix} A + BR^{-1}D^TC & BR^{-1}B^T \\ -C^T(I + DR^{-1}D^T)C & -(A + BR^{-1}D^TC)^T \end{bmatrix} \quad 0 - 16$$

where A, B, C, and D are the state-space matrices and $R = \gamma^2 I - D^T D$. Thus, the main problem becomes:

$$\|\mathcal{F}_l(P, K)\|_\infty < \gamma \quad 0 - 17$$